UNIVERSITÀ DEGLI STUDI DI PAVIA
DOTTORATO DI RICERCA IN FISICA – XXXI CICLO

Theoretical study of integrated grating structures for Silicon Photonics

Marco Passoni

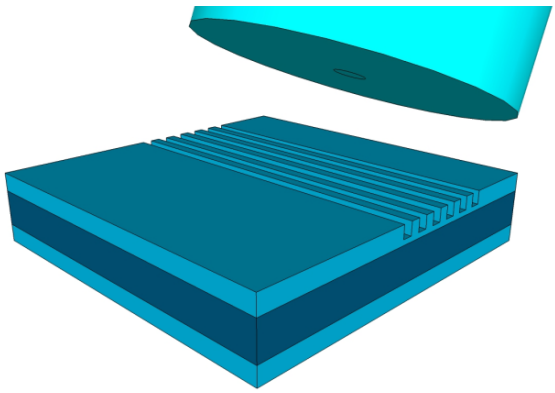

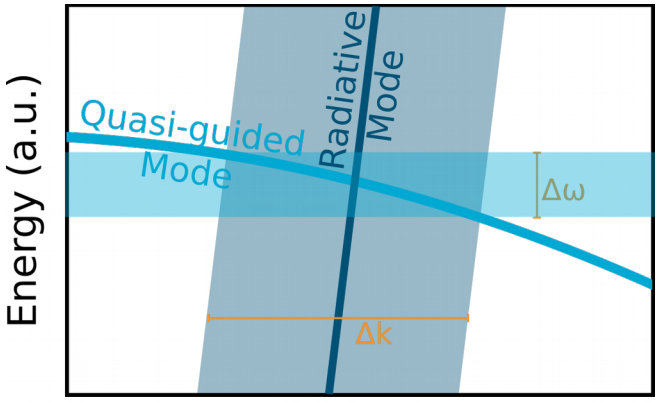

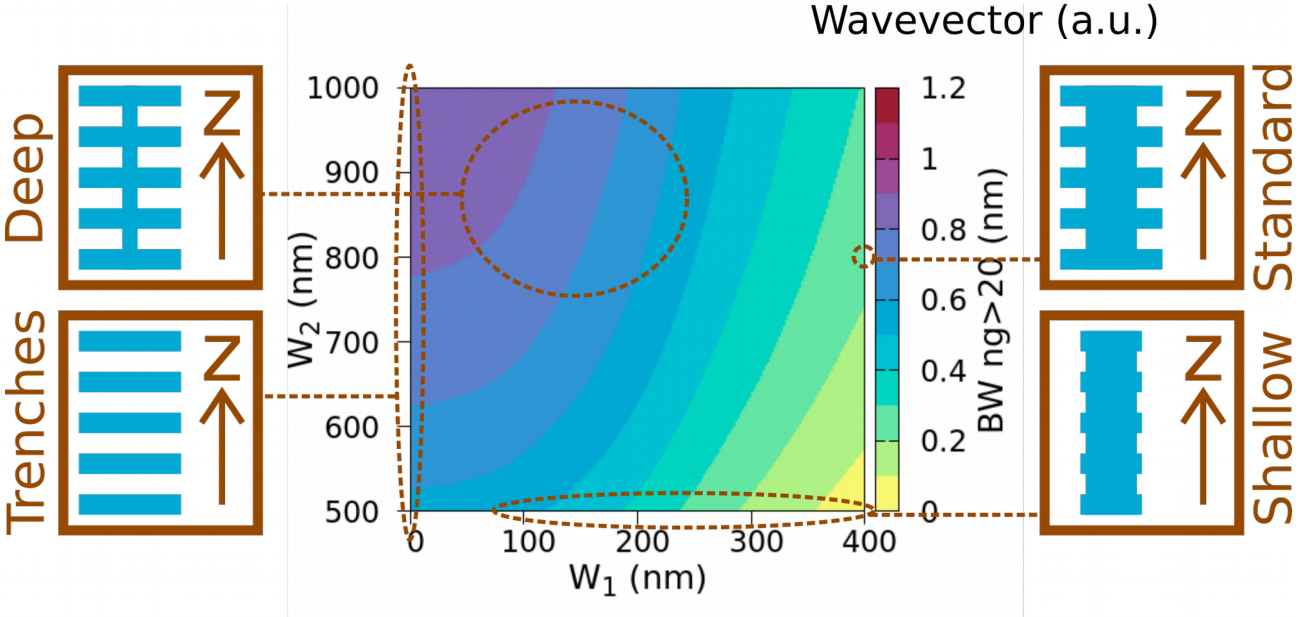

Tesi per il conseguimento del titolo

Full title:
Theoretical study of integrated grating structures for Silicon Photonics

Short title for the side if necessary:
Theoretical study of gratings for Silicon Photonics

Marco Passoni

2018

Università degli Studi di Pavia
Dipartimento di Fisica

DOTTORATO DI RICERCA IN FISICA – XXXI CICLO

Theoretical study of integrated grating structures for Silicon Photonics

Marco Passoni

Submitted to the Graduate School of Physics in partial fulfillment of the requirements for the degree of

DOTTORE DI RICERCA IN FISICA

DOCTOR OF PHILOSOPHY IN PHYSICS

at the

University of Pavia

Supervisors: Prof. Lucio Claudio Andreani, Prof. Dario Gerace

Cover:
Upper left: Graphical representation of a fiber-to-chip grating-coupler.
Upper right: Particular of the band diagram of a 1D PhC Slab, near the coupling point between quasi-guided and radiative modes.
Lower: Slow-light bandwidth (group index greater than 20) of a grating waveguide as a function of W_1 and W_2.

Theoretical study of integrated grating structures for Silicon Photonics

Marco Passoni

PhD thesis - University of Pavia
Pavia, Italy, September 2018

Contents

Introduction

Manipulation of light has been a dream of scientists almost since the first discoveries related to light. However, it is only in the last 50 years that this dream has started to become a reality. In particular, the development of techniques capable of shaping matter at the nano-scale has offered possibilities to control light-matter interaction like never before.

Thus, the branch of Photonics, defined as "the physical science of light generation, detection, and manipulation through emission, transmission, modulation, signal processing, switching, amplification, and sensing" has been born. The potential of Photonics is almost endless, and spans from the simplest applications, such as telecommunication or sensing, to more complex or exotic ones, such as Quantum Optics or Secure Quantum Communication.

Many materials have been proposed as a valid Photonic platform, but none has the appeal of Silicon, leading element of the electronic industry. Indeed, using a common platform for both Photonics and Electronics has obvious advantages, such as a ready and mature technology for realization of Photonic components, along with the possibility of an easy opto-electronic integration. The aim of this particular branch of Photonics, called Silicon Photonics, is the realization of Photonic Integrated Circuits (PICs), following the same route traced by electronic industry years ago. The main field in which Silicon Photonics is expected to have an impact is telecommunication, in particular for mid-and short-range. Optical interconnects have indeed the potential to take over electronic connections for intra- and inter-chip data communications.

To hit this target, however, a careful design of photonic components is needed. Since prototyping costs in Photonics are typically quite high (current foundries can deliver low-cost production only for very high volumes), physical simulation of Photonics devices has taken over a key role in the design flow. In fact, many techniques have been developed over the years for

both optical and electrical simulation, thus providing a rapid and efficient way of improving the designs before fabrication of the actual devices.

In this thesis, some of those techniques are used to simulate the optical properties of photonic devices, with the double aim of better understanding the physical mechanisms involved and of improving the performances. In particular, this thesis focuses on some possible photonic applications of grating structures, trying to use the well understood physics of periodic patterned media and Photonic Crystals to solve real-word problems, especially ones related to optical communication.

The main targeted applications are grating-couplers and slow-light in grating waveguides. In fact, grating-couplers provide efficient light-coupling in and out of a PIC and better understanding of their working principle or improved design strategies could lead to a reduction of the connection losses in optical communication. Slow light, instead, seems to be a viable route to enhance light-matter interaction in electro-optical modulators, allowing for a reduction of energy consumption of transmitting devices.

This thesis is composed by four chapters and four appendices:

Chapter One: An overview (without claim of completeness) on the current status of Silicon Photonics. Some of the basic structures, along with the most common applications, are presented. Additional space is reserved for discussion on the physics of light propagation in periodic media and on the numerical methods employed in this thesis.

Chapter Two: A numerical study on the properties of Silicon-On-Insulator grating-couplers, with particular attention on the physical mechanisms underlying their bandwidth.

Chapter Three: A feasibility study on a grating-to-grating approach for light coupling between two chips belonging to two different platforms, namely conventional Silicon-On-Insulator and an Indium Phosphide based one.

Chapter Four: A study of slow-light performance of silicon grating waveguides: slow-light bandwidth and insertion losses.

Appendices: Theory and details on the numerical methods employed, in particular Aperiodic-Fourier Modal Method (A-FMM) and Particle Swarm Optimization (PSO). Details on the grating-couplers coupling efficiency and bandwidth optimization procedure are also given.

Chapter 1

Integrated Photonics

Photonics is the science of light creation, manipulation, and detection at the nano-scale. The shaping of matter at the nano-scale offered by modern technology has generated interesting questions on what happens to light-matter interaction when the latter can be modeled on a scale comparable with the wavelength of the light. Thus, the way has been opened to a whole new range of phenomena and possible applications regarding light. In particular the possibility of using silicon as base material, leveraging on the solid technological background developed for electronic industry, has gained special attention in the past years, leading to the creation of an entire new field: Silicon Photonics.

This chapter is structured as follows. The first section will give an overview of current state of Silicon Photonics. The second section will provide insight on the physics of light propagation in periodic structures, a key topic of photonics. The third section will present some of the numerical methods used to solve Maxwell equations within arbitrary geometry, a fundamental step in the design of photonic devices.

1.1 Overview on Silicon Photonics

In the past years silicon has often appeared as the ideal candidate for Photonic applications in general, and for the realization of Photonic Integrated Circuit (PICs) in particular. Silicon Photonics could indeed take advantage of all the techniques developed for the electronic industry, and consequently benefit from an easier opto-electronic integration with respect to other materials.

The most important platform in electronics, and thus the starting point of

Silicon Photonics, is the Complementary Metal-Oxide-Semiconductor (CMOS). In this platform a thin layer of silicon (few hundreds of nanometers) is embedded between two sheets of oxide. The thin silicon layer can then be doped and patterned to create electronic circuits, and the top oxide can be opened, allowing metal contacts to reach the silicon. Usually the full CMOS structure is built on a silicon substrate, for both mechanical support and thermal dissipation. This kind of vertical structure is ideal for the building of Metal-Oxide-Semiconductor Field-Effect Transistors (MOSFETs), on which all current electronics is based.

Nevertheless, the features of the CMOS scheme are well suited also for some applications in Photonics. Since both silicon (Si) and silicon oxide (SiO_2) are transparent at typical telecom wavelengths (1.31 µm or 1.55 µm) and their refractive indexes are quite different (typically around 3.44 and 1.44 for Si and SiO_2, respectively), efficient waveguiding of light inside the very same silicon layer used for electronics is easily obtained. Moreover, due to its centro-symmetric crystalline structure, χ^2 non-linearities are very weak in silicon (only the surface contribution remains), so quite high power inside the waveguides can be reached before unwanted nonlinear phenomena, such as Two Photon Absorption (TPA) or Second Harmonic Generation (SHG), take place.

However, using silicon as optical material is not without drawbacks. The main one is that, due to its indirect bad-gap, silicon is a poor light emitter. Thus, silicon based PICs need some sort of external light source or the integration with other materials able to provide the necessary gain for an integrated light source — See Lasers in Par. 1.1.4.

Another big problem of silicon is that, always due to its centro-symmetric nature, the linear electro-optical (Pockels) effect is absent, and can only be obtained by inserting strain. Thus, it is impossible to realize efficient electro-optical modulators so common in other platforms. However, a promising solution has been found in the Plasma Dispersion Effect — See Modulators in Par. 1.1.4.

Thus, Silicon Photonics has been proposed as a valid alternative for many applications in recent years, both in scientific research and commercial applications. This chapter will provide first a very brief summary of past history of Silicon Photonics, then the actual state and future challenges will be discussed, together with an overview of passive and active components nowadays available.

1.1.1 Brief history

Envisions of an optical "super-chip" able to reproduce any components available in an optical laboratory have been around since early seventies [1]. Those dreams have somewhat collapsed under the blows of reality, since still nowadays no "super-chip" containing all the ingredients for a complete integrated Photonics platform — light production, manipulation and detection — has been demonstrated.

Nevertheless, much has been achieved over the years. Research during the eighties and the nineties established the basic building blocks of modern Silicon Photonics. It is during this period that the basic concepts of waveguides, modulators and detectors were established.

Regarding the waveguides, after first explorative studies on the possibility of obtaining waveguides both in doped silicon [2, 3] and Silicon-On-Insulator [4], research focused mainly on reducing propagation losses [5, 6, 7], which were mainly determined by the material type and quality, and by surface roughness. Only later, in the nineties, the focus shifted on the shrinking of waveguides towards the modern single mode operation [8, 9, 10].

In the same period the basics of optical signal modulation in silicon were developed. The seminal work by Richard Soref [11] demonstrated that index modulation in silicon can be achieved by Plasma Dispersion effect, namely the change of index of refraction by effect of free carrier density. A first demonstration of a phase modulator based on this effect quickly appeared [12]. With the inclusion of such device inside a Mach-Zehnder interferomenter, the modern silicon optical modulators have been born [13]. Mach-Zehnder modulators based on the thermo-optic effect have also been proposed [14], but soon abandoned due to their low speed. Later research on modulators focused on increasing modulation speed and decreasing the energy consumption per bit, culminating in 2004 with the first realization of a 10 GHz modulator [15].

Regarding photo-detectors, first devices begun to appear in the mid-eighties at AT&T Bell Laboratories. They were based on the implantation of germanium in silicon, which at sufficient concentration can lower the band edge up to telecom wavelength [16, 17, 18]. Such structures were realized using a Si-Si_xGe_{1-x} super-lattice [19], and a Quantum Efficiency of 40% was measured. The first CMOS compatible device was proposed in the early nineties [20], albeit with a very low QE at telecom wavelength. Successful research managed to improve both quantum efficiency and response time [21, 22, 23].

Although the long dreamed photonic "super-chip" is still far away, considerable progress has been made over 40 years of research. For additional

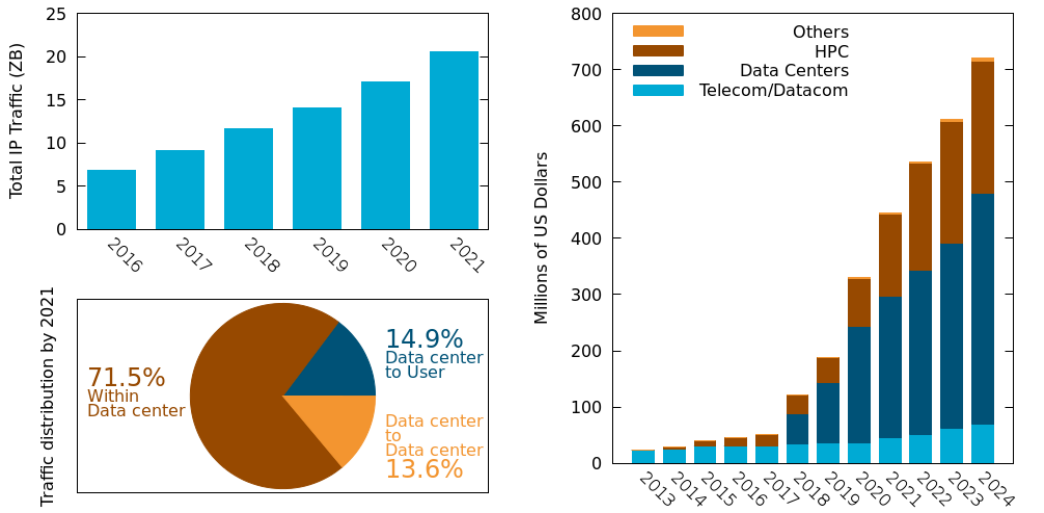

(a) Traffic through data centers. (b) Market value of optical interconnects.

Figure 1.1: Some estimation on the future of Silicon Photonics for optical interconnects. Data taken from [28] and [29].

information on early research in Silicon Photonics see the works from G.T. Reed [24] and R. Soref [25].

1.1.2 Actual state and future challenges

Silicon Photonics nowadays is somewhat in the middle of the transition from research to mature technology. Although not all the desired features can be obtained on a single photonic chip, realities that leverage on existing technology to offer small industries and start-ups easy access to photonic foundries, allowing for rapid R&D, began to appear [26, 27]. The aims of these partnerships is to bridge the so called "Valley of Death", namely to help industries to make the jump from prototyping to a small volume fabrication.

The main targeted applications for Photonics right now are telecommunication, sensing, and especially optical interconnection, which is the main driver behind current Photonics R&D. The term optical interconnects usually refers to the substitution of electrical connections on any scale, from long distance communication (where optical fibers have been the dominant technology since the 90s), through mid-range applications, such as inside data-center and super-computers (where optical interconnects have begun to affirm in the late 2000), down to intra-chip communication (still domain of electrical interconnects).

Indeed, optical interconnects do not possess any physical constraint on

the bit-rate, as electrical ones do [30]. Thus, optical interconnects, especially Silicon Photonics based ones, are seen as the only technology able to meet the growing demand of bandwidth. Silicon Photonics will be particularly beneficial to data centers, which will see a dramatic increase in traffic [29], especially within the single data center, and will probably be the major drivers of the optical interconnects market in the near future [28, 31]. Research on optical interconnects in the next years will probably focus on reducing the energy consumption, which, although greater speed can be delivered, is now higher than the typical 1 pJ per bit needed by electrical interconnection.

As an additional possible application of Photonics in the future, it would be impossible not to mention Quantum Technologies. Although still a technology confined in research laboratories, with few exceptions such as true random number generator [32], Photonics has shown great potential as a platform for Quantum Technologies [33], especially in the areas of Quantum communication, metrology, and sensing.

1.1.3 Passive components

Waveguides

In optics, waveguides are defined as structures that guide electromagnetic radiation, allowing the propagation of light in selected directions with minimal energy loss and forbidding the propagation along other directions. At near infrared frequencies, which are the region of interest for Silicon Photonics, two ways of providing light confinement exist: Total Internal Reflection (TIR) and Photonic Band Gap (PBG).

Total Internal Reflection (TIR) takes place when a light ray is propagating beyond the limiting angle in a high index dielectric and cannot escape it. This is the simplest and most efficient way of confining light in actual fabricated structures. Thus, Total Internal Reflection is employed in the totality of commercially available Silicon Photonics devices. The most common type of 1D-waveguide in SOI platform is the so called rib (sometimes ridge) waveguide — see Fig 1.2.

The main source of loss in this type of waveguide is Rayleigh scattering from surface roughness. With current fabrication techniques propagation loss varies greatly. It can range from the order of 2.5 dB/cm available at commercially available foundries as EuroPractice [34] to the more or less 1 dB/cm accepted as industry standard [35], while record losses as low as 0.026 dB/cm have been reported in the research literature for multi-mode waveguides [36].

Instead, the Photonic Band Gap (PBG) approach is based on the fact

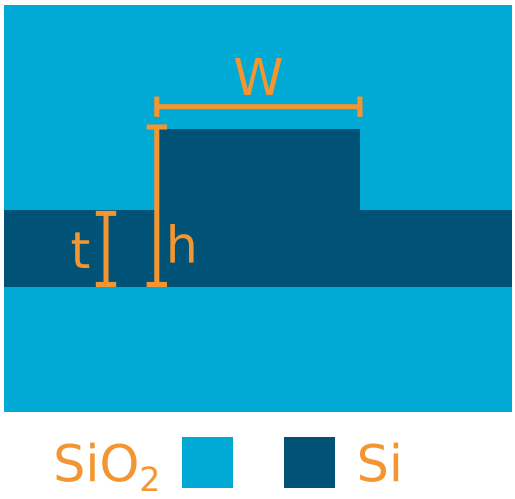

(a) Cross section.

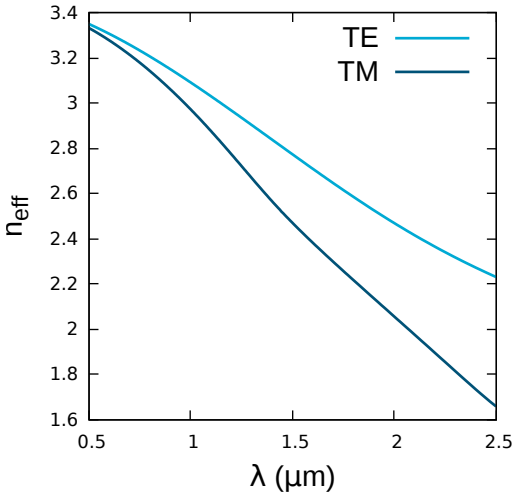

(b) Effective index.

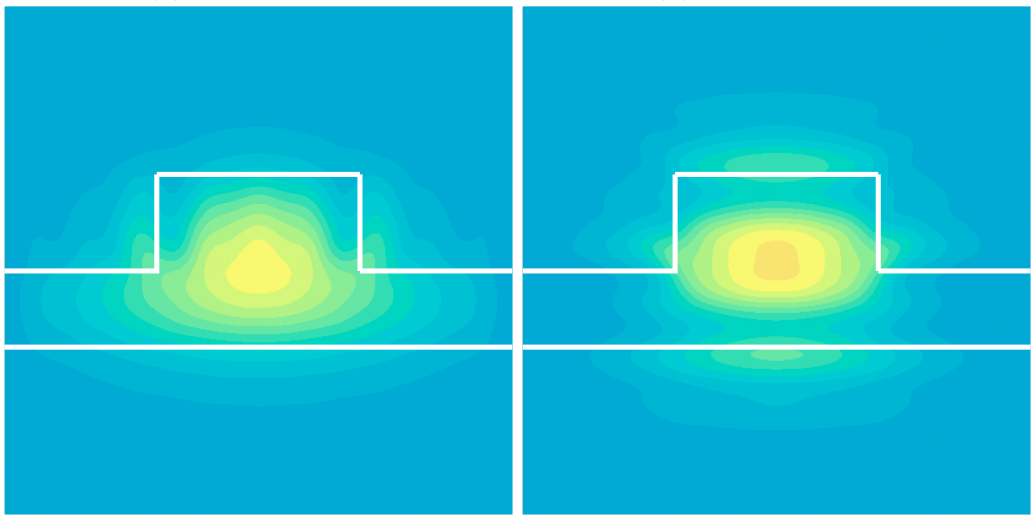

(c) Field distribution of fundamental TE mode at λ= 1.31 µm

(d) Field distribution of fundamental TM mode at λ= 1.31 µm

Figure 1.2: Sketch and features of a typical rib waveguide — h=310 nm, t=150 nm, W=400 nm. Normally the terms "ridge" refers to fully etched (t=0) waveguides.

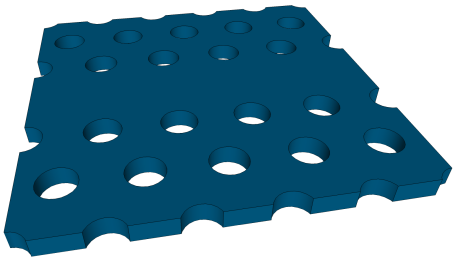

(a) Sketch of typical structure of a W1 waveguide.

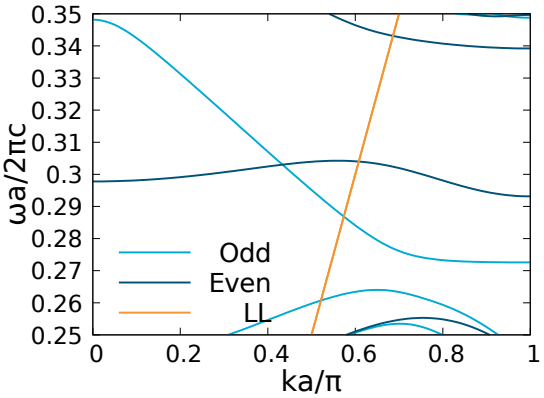

(b) Example of bandstructure of a W1 waveguide built out of a $\varepsilon = 12$ dielectric slab suspended in air.

Figure 1.3: Sketch and features of a typical W1 PhC-Slab waveguide.

that regions of energy in which light propagation is forbidden (indeed, a Photonic Band Gap) can appear in periodically patterned structures. Such phenomenon can be used for the realization of very efficient mirrors, and thus waveguides. Numerous ways of creating waveguides by this approach have been proposed over the years. The most prominent one is without doubt the W1 waveguide in Photonic Crystals Slabs, in which a PBG in the horizontal direction is joined to TIR in the vertical direction to realize 1D waveguides. Although it is a very interesting solution, allowing for the integration of typical features of Photonics Chrystals, such as slow-light [37], this technology is not mature enough for mainstream commercial applications. The main reason, besides the more complex fabrication, is disordered induced loss [38, 39] which, even with the best performing fabrication techniques, gives a total loss at least an order of magnitude greater than in TIR based waveguides [40].

Bragg gratings

Bragg gratings are probably the easiest way to bring all the features of periodic structures and Photonic Crystals to integrated Silicon Photonics. Typical realizations of Bragg gratings are based on periodic etching in a 2D silicon slabs or width modulation in silicon nanowires — see Fig. 1.4.

Typically in a Bragg grating three different regimes, corresponding to different scales of wavelength compared to the period Λ of the grating, can be identified — see Fig. 1.5. At lower energies ($\lambda >\approx 2\Lambda$) there is the so

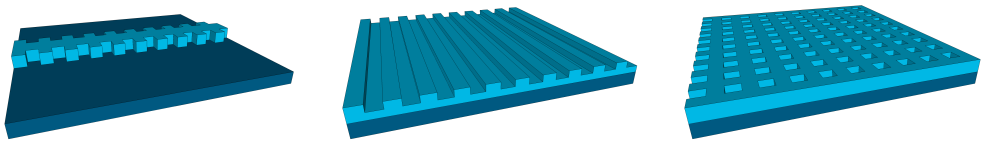

(a) 1D waveguide — 1D grating (b) 2D waveguide — 1D grating (c) 2D waveguide — 2D grating

Figure 1.4: Three possible configurations of Bragg gratings in Silicon Photonics.

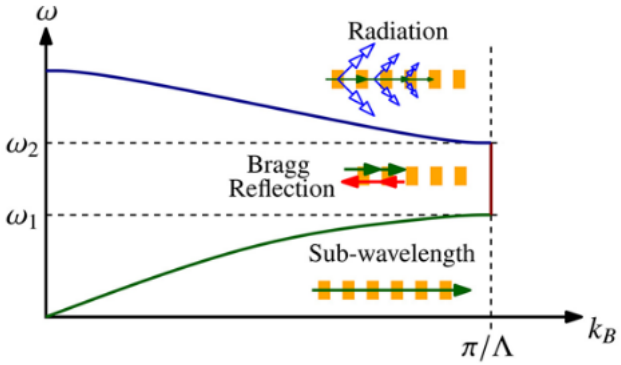

Figure 1.5: Typical band dispersion of a 1D Bragg grating. The three relevant regimes — sub-wavelength, Bragg reflection and radiation — and relevant energy regions are enlightened. Image reported from [41].

called sub-wavelength regime. In this region light can freely propagate in the grating as in a bulk material (or a waveguide composed of bulk material, in this case), but the dispersion is modified. At intermediate energy ($\lambda \approx 2\Lambda$) usually sits the band gap, a region in which propagation of light inside the grating is forbidden and any light externally incident on the grating is scattered back. At higher energies ($\lambda <\approx 2\Lambda$), and above the light line of the low index material, there is the radiation regime. In this regime guided light propagation is allowed in the grating, but the guided mode is coupled to the continuous of radiative modes by first (or more) order diffraction. Thus, the guided mode inside the grating has a finite lifetime after which almost all the light is scattered away. For details on the reason of such rich behavior see Sec. 1.2: Physics of Periodic Structures; here the focus will be on some of the possible applications of these three different regimes.

The sub-wavelength regime is very powerful in all the platforms in which only few materials (and thus, only few values of the refractive index) are

available, such as Silicon Photonics. This because a sub-wavelength periodically patterned medium can be treated as an effective uniform material with an effective index dependent on the patterning. Thus, sub-wavelength pattering can, in particular conditions, be equivalent to changing the material properties. Moreover, this effective medium is generally anisotropic [42, 43] and can be tailored to tweak TE and TM properties differently and independently. Sub-wavelength structures were first proposed to address the problem of fiber-to-chip light coupling, where were used, in an edge-coupling scheme, to adapt the effective index between an optical fiber and a standard integrated silicon waveguide [44]. Since then, their application field has expanded dramatically, contributing to almost every topic in Silicon Photonics: waveguides [45] and waveguide-crossing [46], grating-couplers [47, 48, 49], waveguide lenses [50, 51], in-plane light routing [52], (de)multiplexers [53], mode converters [54], optical [55] and electrical [56] modulators, multi-mode interferometers [57, 58] and polarization splitters [59]. For a complete overview on the use of sub-wavelength structures see: Robert Halir *et al.* "Waveguide sub-wavelength structures: a review of principles and applications" [41] and Robert Halir *et al.* "Subwavelength-grating metamaterial structures for silicon photonic devices" [60].

Devices based on the concept of Photonic Band Gap are essential to Silicon Photonics, and gratings are indeed the easiest way to insert totally or partially reflective mirrors inside integrated circuits, thus providing a basic building block for cavities and Photonic Crystals based structures. For example, the PBG available in a triangular lattice of holes [61] has enabled the development of W1 waveguides and all the related physics and applications. More important, 1D grating mirrors are the basis for many laser cavities [62, 63]. In addition, fancier applications are possible, such as temperature [64] or biological [65] sensors.

Regarding operation in the radiation regime, although it seems it would only insert losses and should be avoided, it can indeed be a desirable feature when the aim is to couple light in and out of the planar chip through the vertical direction. Such devices, called grating-couplers, have stimulated a great deal of research in the past twenty years, focusing in particular in decreasing insertion loss and increasing operational bandwidth. Grating-couplers exist in both 1D [66] and 2D [67, 68] versions, the former being able to couple only one polarization and the latter being suitable for both. While the simplest configuration is the uniform one [69], variants have been developed to address particular problems. Chirped or apodized gratings [70, 71, 72] can be realized to improve the insertion loss over the uniform ones, while focusing gratings [73, 74] can be employed to reduce the total footprint of the component, or both strategies can be used together [75].

Moreover, it is important to notice that each working regime of a Bragg grating does not exclude the others. On the contrary, they can be joined together to obtain additional freedom and functionalities, such as sub-wavelength grating-couplers, where sub-wavelength patterning is used in a 1D grating to finely tune the index of the material [47, 76].

Chapter 2 and 3 of this thesis will be devoted to 1D grating-couplers. The former will focus on Fiber-to-Chip coupling, analyzing the mechanisms behind the bandwidth composition and the trade-off between bandwidth and insertion loss. The later will focus on the co-design of silicon and indium phosphide grating-couplers for chip-to-chip coupling in a hybrid integration scheme.

Cavities

Optical cavities or resonators are structures that are able to trap light for a certain amount of time. Two main figures of merit for an optical resonator exist: the quality factor Q and the mode volume V. The Q-factor is related to the time it takes for the field inside the resonator to decay. It can be calculated as 2π times the ratio between the energy stored in the cavity and the energy loss per cycle (in the absence of a forcing field), or equivalently, as the ratio between the frequency of the resonance and its spectral width (intended as Full-Width-Half-Maximum). The mode volume V gives an indication on how much the cavity mode is extended in real space. It is usually defined as the inverse of the maximum of the field (once the mode is correctly normalized) and it is related to the Purcell factor [77].

Many ways have been proposed to realize cavities in SOI platform, based on either TIR, PBG or both. Typical TIR-based cavities in Silicon Photonics are based either on ring resonators [78] or Whispering Gallery Modes (WGM) in microdisks [79, 80, 81]. These types of cavities usually exhibit a very high Q-factor, at the price of fairly large mode volumes. Many applications have been demonstrated using these resonators, such as lasers [82], sensors [83, 84], modulators [85], switches [86, 87], routers [88, 89], and nonlinear optical devices [90, 91].

Regarding PBG confinement, two major classes of cavities can be identified [92]: nano-beam cavities and PhC Slab ones. Both these types can reach very high Q-factors together with small (on the order of few cubic wavelengths) mode volumes. The main drawbacks are their complexity, both in fabrication and design, and the quite high sensitivity to fabrication errors and disorder [93].

Nano-beam cavities are usually based on a periodic modulation of a 1D TIR-based waveguide. The simplest approach is to use PBG to create mirrors

to build a Fabry-Perot cavity [94] or using a more gentle confinement by the mode-gap modulation approach [95].

In PhC Slabs, instead, the easiest way to create a cavity is simply to insert a defect in the periodic lattice. The most prominent examples includes H- [96, 97] and L-cavities [98, 99], namely one ore more holes missing or displaced from a triangular lattice of holes etched in a silicon slab. Different types of cavities have however been proposed and tested, such as Fabry-Perot heterostructures [100], mode-gap modulation [101] or effective bi-chromatic potential [102].

Multiplexers and de-multiplexers

The use of Wavelength Division Multiplexing (WDM) as the main road to increase bandwidth in current Silicon Photonics for optical interconnects has generated a high demand for multiplexers and de-multiplexers. Those are components able to combine signals at different wavelengths from different physical input channels in a single physical output channel, and vice versa.

Many solutions to this problem have been explored over the years. Early integrated structures simply translated some common schemes of discrete optics, such as Echelle gratings, i.e. gratings working at a very high (tens of even hundreds) diffraction order [103]. The advantage of using such a high diffraction order lies mainly in the enhancement of the resolving power, thus allowing a finer channel spacing, but at the price of a reduced Free Spectral Range (the difference in wavelength between two consecutive orders diffracted at the same angle), which ultimately limits the wavelength span in which the multiplexer can operate. The first SOI-based device employed a reflection-grating in the Rowland configuration [104]. This solution suffered from several drawbacks, mainly in term of losses (around 10 dB) and of physical footprint (on mm scale).

To solve such problems, a different approach has been proposed: Arrayed Waveguide Grating (AWG) [105] — see Fig. 1.6a. Simply stated, an AWG is composed of two Free Propagation Regions (FPR) connected by an array of waveguides of different length, which are designed to give a $2\pi m$ (m is the order of the grating) phase shift between each other at the central wavelength of the component. The input and output waveguides are connected to the two FPRs. The operating principle is as follow: when a signal at the central wavelength arrives in the first FPR, it diverges and is split between the arrayed waveguides; since each waveguide has a 2π multiple phase shift with respect to each other, the phase distribution at the input of the array is exactly reconstructed at the output; the light is so re-focused in the central position of the second FPR; when the input signal is at a different wavelength,

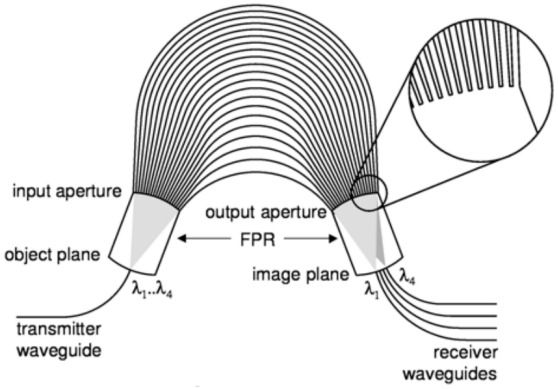

(a) Arrayed-Waveguide Grating (AWG). Figure reproduced from [105].

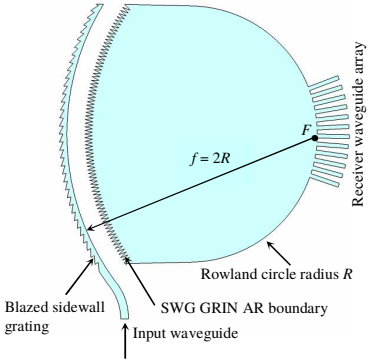

(b) Sidewall grating waveguide. Reproduced from [53].

Figure 1.6: Two possible configuration of a (de)multiplexing device.

a wavelength dependent phase shift is applied between each waveguide at the end of the array, causing the light to be focused in a different position; if output waveguides are properly placed at the end of the second FPR, the demultiplexing action take place. Consequently, the multiplexing is obtained by operating the device in the reverse direction. The chosen order of an AWG grating usually varies between 20 and 50, leading to different trade-offs in the multiplexer behavior [106, 107].

Great performances have been demonstrated by AWG-based devices [108, 109, 110], such that they nowadays constitute the de-facto standard for WDM applications. However, research has never stopped, and recent developments have provided AWG (de)multiplexers with additional features, such as athermal operation [111], compatibility with Mode Division Multiplexing (MDM) [112] and reconfigurable add-drop [113].

More recently, a viable alternative to AWG has been found in sidewall grating waveguides — see Fig. 1.6b. In this approach, a grating is etched in the side of a conventional ridge waveguide, in such a way to radiate power outside the waveguide from the side. The waveguide is curved, thus radiation of different wavelengths is focused in different points of the Rowland circle, where the collecting waveguides are placed [53, 114]. The main advantage of this approach is the compactness, since it can be fitted in a fraction of the space of conventional AWG.

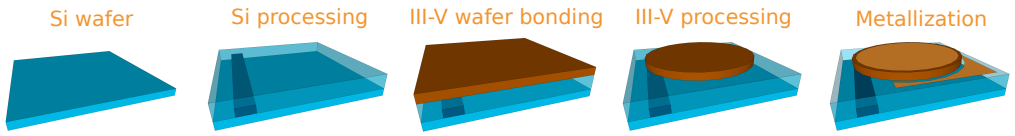

Figure 1.7: Typical workflow of wafer bonding process.

1.1.4 Active components

Lasers

The realization of light sources and amplifiers is probably the most important feature in Silicon Photonics, but at the same time its greater challenge. Due to the indirect nature of the bandgap in silicon [115], obtaining electrically pumped gain is quite a difficult task. Early solutions to this problem were the packaging of external lasers together with the PIC. More recently, great effort was placed in the research for integrated light sources. Three main lines of research can be identified: direct lasing of silicon, epitaxial integration, and hybrid integration.

Regarding silicon, two main ways to reach lasing exist: enhancement of radiative processes due to exciton confinement and stimulated Raman scattering. Exciton confinement can be achieved by nano-structuring the material, for example in porous silicon [116, 117], silicon nano-crystals [118] or periodically patterned structures [119, 120]. The problem with this approach, besides the difficult fabrication, is that it requires low temperatures to work. Stimulated Raman scattering takes advantage of the gain which is created at the Stokes lines when silicon is pumped with a laser [120, 121]. Their performances can be quite high [122], and can access virtually any wavelength, but, requiring an additional pump laser, do not resolve the problem of integrating a light source.

The most promising approach nowadays is to join silicon with other gain materials, such as III-V compounds, relying on either epitaxial or hybrid integration. Epitaxial integration consist in the direct grow of a gain material on silicon substrate, which can be difficult given the great lattice and thermal coefficient mismatch usually involved [123]. Numerous solutions have been proposed, based either on GaAs [124] or on GaSb [125]. However, performance level and reliability are still a problem to be solved, especially taking into account the high costs involved.

To overcome the intrinsic problem of monolithic integration, many schemes of hybrid integration have been studied, the most important being wafer bonding [126] and transfer printing [127]. The wafer bonding technique — see Fig. 1.7 — consists in the bonding of an unprocessed III-V wafer to a

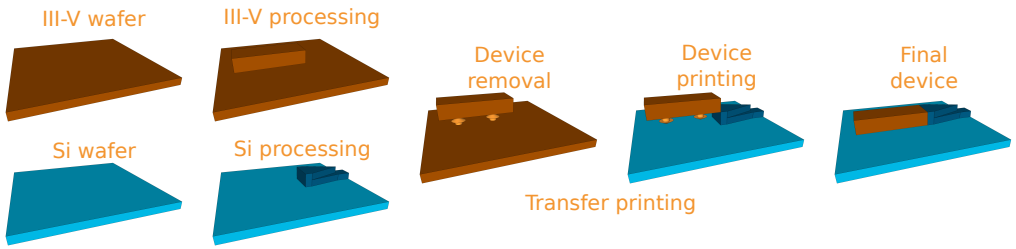

Figure 1.8: Typical work-flow of transfer-printing process.

previously worked SOI wafer, both directly or with the addition of a "glue" material. The additional layer is then processed to create the lasing devices and the control electronics. This kind of approach allows for great versatility, since many structures, such as micro-disks (both single [128] and array [129]), rings [130], Fabry-Perot [131, 132] and Distributed Feedback lasers [62] can be realized. However, it presents also some disadvantages: wafer bonding usually requires very careful polishing of the surfaces, and, since the processing of the III-V wafer takes place after bonding to silicon, it can result in considerable material wastage in case of any error in the fabrication.

On the contrary, transfer printing — see Fig. 1.8 — allows for the transportation of individual devices between two wafers. The material wastage is greatly reduced, since SOI and III-V devices can be built and tested separately, and then only the good performing ones are selected to be joined. While a little less versatile than wafer bonding, transfer printing has proven successful in a wide range of materials and structures. For examples, Fabry-Perot lasers have been demonstrated in GaAs [133, 134] and InP [135, 136]. The main drawback of this approach is the sub-µm alignment needed in the transfer process.

In the prospect of hybrid integration, chapter 3 of this thesis will be devoted to a feasibility study of light coupling between SOI and InP platforms via a grating-to-grating coupling scheme. The aim is to open the way towards hybrid integration with conventional flip-chip technology, at lower cost than both wafer bonding and transfer printing.

For a comprehensive review of current status of lasing in silicon see: D. Liang & J. Bowers "Recent progress in laser on silicon" [137].

Modulators

Another class of key active elements needed in the Silicon Photonics toolkit is the one of electro-optical modulators. These devices are responsible for the modulation of an optical signal using an electrical driver, a key feature

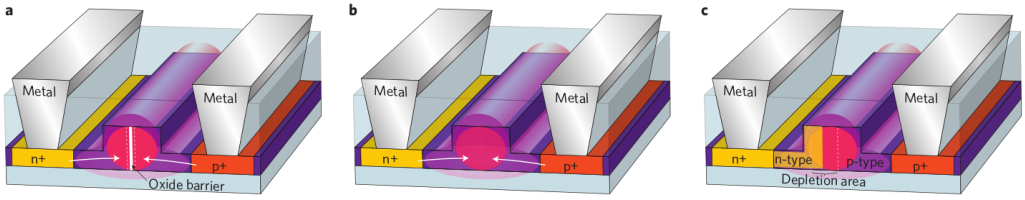

Figure 1.9: Three possible implementations of the Plasma Dispersion Effect in silicon using a p-n junction: (a) carrier-accumulation, (b) carrier-injection and (c) carrier-depletion. Figure reproduced from [143].

for the realization of optical interconnects.

Typical modulators, either integrated or not, rely on some kind of electro-optic effect, which causes an electric field to modify either the real (eletro-refraction) or the imaginary (electro-absorption) part of the refractive index of a material. The most common effects are Pockels, Kerr or Franz–Keldysh. Unfortunately those approaches are unfeasible in silicon, since the relevant effects are quite weak [11] compared to other materials (such as III-V compounds). Nevertheless, attempts to relay on such phenomena have been made. For example, it has been demonstrated that, by introducing strain in the silicon, usually by adding a small layer of silicon nitride on top of a silicon waveguide [138], linear Pockels effect can be induced [139]. This has even led to the realization of working modulators [140], but this approach is not the most suitable for commercial integrated applications, both for the high voltages ($\approx 30\,\mathrm{V}$) required and the poor scaling in frequency [141]. Therefore, the two main options practically available in silicon are thermal modulation and plasma dispersion effect.

The first effect is based on the change of refractive index as a function of temperature. This effect is quite huge in silicon, due to the large thermo-optic coefficient, but suffers from several major drawbacks: (i) the modulation speed is too low to meet the performance expectation of optical interconnects; (ii) the energy consumption can be quite high, and (iii) the operation in environments with huge thermal fluctuations can be quite challenging [142].

The second effect is the modification of the refractive index as a function of carrier density, and it is currently the most employed. It is usually realized with the aid of a p-n junction inside the waveguide, and it is commonly found in one of three possible implementations: carrier-accumulation, carrier-injection and carrier-depletion — see Fig 1.9. The carrier-accumulation approach requires a thin insulating layer inside the p-n junction, to effectively turn the junction into a capacitor. The index modulation takes place by charging or discharging the capacitor. This method was the basis for the

first realized modulator operating at Gigahertz rates [15]. While being quite effective, it suffers from difficult fabrication and high optical loss. In the carrier-injection configuration a region of intrinsic silicon, where the waveguide is built, is placed inside the junction. Forward-biasing the junction injects electrons and holes into the intrinsic region, providing the index modulation. This solution is quite effective and exhibits low optical loss, however the speed is limited by the carrier lifetime in the intrinsic region. The carrier-depletion approach requires the realization of the p-n junction inside the waveguide. Thus, a depletion region is created, whose amplitude can be varied by changing the applied voltage in reverse-bias configuration. This solution ensures high modulation speed and low optical loss, but the magnitude of the modulation is quite low compared to the other two approaches operating at the same voltage.

Beyond the type of index modulation, electro-optic modulators can be further divided into two classes based on their working principle: the ones based on resonating cavities and the ones based on Mach-Zehnder (MZ) interferometers, both with their advantages and disadvantages. Cavity based modulators — see Fig 1.10a — use the cavity resonance to insert a narrow feature in the spectral response of the component. By modulation of the index in the region of the cavity a shift in the resonance is achieved, allowing the device to work as a switch. The main advantage of this solution is compactness, since resonant cavities can be made very small inside PICs. However, they are characterized by a very narrow working bandwidth (fractions of nm), so their versatility is compromised. The majority of resonant modulators proposed over the years are based on ring resonators [85, 144, 145, 146], but also other solutions have been proposed, such as nano-beam [147, 148] or PhC-slabs [149] based cavities.

Instead, in Mach-Zehnder modulators the index modulation is applied to one, or both, the arms composing the interferometer — see Fig. 1.10b — to change the intensity ratio between the two outputs of the Mach-Zehnder. Consequently, this allows for a very fast and broadband modulation [150, 151, 152, 153], although at the price of a bigger footprint than cavity modulators (usually millimeter long arms are needed).

More recently, attempts have been made to join the best of both approaches, by using slow-light features to enhance light matter interaction in Mach-Zehnder modulators. Since the phase shift provided by one arm is, at constant index modulation and length, proportional to the group index of the waveguide, the aim is to leverage on the high group index that can be obtained in periodically patterned structures. The main drawbacks in this case are a more complex fabrication and a reduction of the optical bandwidth with respect to conventional MZ, although not as much as in resonant

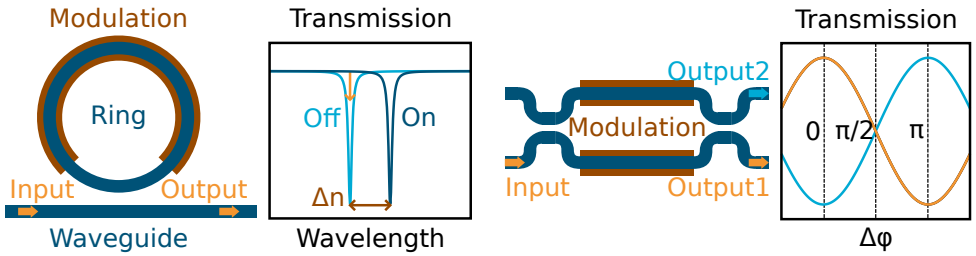

(a) Ring resonator.

(b) Mach-Zehnder interferometer.

Figure 1.10: Sketch and working principle of the two most common configurations of a silicon electro-optical modulator.

devices. In this direction, solutions has been proposed based either on W1 waveguides in PhC Slabs [154, 155, 156] or corrugated waveguides [157, 158] (also called grating waveguides). Chapter 4 of this thesis will be devoted to the optimization of slow-light properties of silicon grating waveguides for this kind of application. For a detailed survey of current status of electro-optical modulators see G.T. Reed *et al.* "Silicon optical modulators" [143].

Photodetectors

The last fundamental building block for Silicon Photonics is an efficient detector. The realization of photo-detectors in silicon has been thwarted by the same problem afflicting the light sources. A few attempts have been made to realize photo-detectors based only on silicon, by using defects to push the absorption edge inside the band gap down to useful frequencies [159]. However, this approach has not generated much interest in recent years.

The most promising approaches for practical realization of detectors in Silicon Photonics are basically two: hybrid integration of III-V compounds and monolithic integration of germanium. The hybrid integration of III-V compounds, usually by direct or adhesive wafer bonding, was probably the first technique to deliver high performances [160]. Many solutions have been proposed over the years, based either on direct [131], evanescent [161] or vertical [162] coupling schemes.

The monolithic integration of germanium is based on direct epitaxial growth of germanium on silicon wafers. Careful optimization of the growth techniques has allowed to solve the 4.2% lattice mismatch problem. Furthermore, current techniques rely on the difference in thermal expansion between silicon and germanium to insert tensile strain in the latter, enhancing its optical properties [163]. Several high-performance and possibly CMOS-compatible solutions have been demonstrated during the years [164, 165, 166],

making the monolithic integration of Ge a viable route for the future of photo-detection in silicon.

In the field of photo-detectors for applications in Silicon Photonics a special mention is reserved for the ContactLess Integrated Photonic Probes (CLIPPs). They rely on a capacitive measurement of the change in conductance of the silicon waveguide, induced by sub-gap absorption mechanisms such as Surface-State Absorption [167]. In this way a fast and non invasive measure of the light intensity inside the waveguide is achieved, opening the way to real time monitoring of PICs and feedback mechanisms [168, 169].

1.2 Physics of periodic structures

In this section a small summary of the electromagnetic properties of periodic structures is reported, following the one given in the book "Photonic Crystals: Molding the Flow of light" [170].

1.2.1 Maxwell Equations as eigenvalue problem

The starting point of every discussion on classical electromagnetism are of course Maxwell equations [171]:

$$\nabla \cdot \mathbf{D} = \rho \tag{1.1a}$$

$$\nabla \cdot \mathbf{B} = 0 \tag{1.1b}$$

$$\nabla \times \mathbf{E} + \frac{\partial \mathbf{B}}{\partial t} = 0 \tag{1.1c}$$

$$\nabla \times \mathbf{H} - \frac{\partial \mathbf{D}}{\partial t} = \mathbf{J}. \tag{1.1d}$$

The material is then specified through its constitutive relations:

$$\mathbf{D} = \mathbf{D}(\mathbf{E}) \tag{1.2a}$$

$$\mathbf{B} = \mathbf{B}(\mathbf{H}) \tag{1.2b}$$

which allow to solve Maxwell Equation to get full electromagnetic behavior.

The constitutive relations 1.2 can in general be very complex. For the sake of simplicity the present treatment will be restricted to nonmagnetic, linear and isotropic material, where the constitutive relations can be simply specified:

$$\mathbf{D} = \varepsilon\varepsilon_0\mathbf{E} \tag{1.3a}$$

$$\mathbf{B} = \mu_0\mathbf{H} \tag{1.3b}$$

where $\varepsilon_0 = 8.854 \cdot 10^{-12}$ F m^{-1} and $\mu_0 = 4\pi \cdot 10^{-7}$ H m^{-1} are the vacuum permittivity and permeability, respectively. The quantity ε is the relative dielectric constant, it is a property of the material and can depend on frequency and position.

In trying to solve the Maxwell equations the easiest route is to apply the separation of variables, namely to write the electric and magnetic fields as a product of two functions, one dependent on space only, the other on time only. Moreover, due to linearity of Maxwell equations, it is possible to look only at solutions harmonic in time:

$$\mathbf{E} = \mathbf{E}(\mathbf{r})e^{-i\omega t} \tag{1.4a}$$

$$\mathbf{H} = \mathbf{H}(\mathbf{r})e^{-i\omega t}, \tag{1.4b}$$

since any general solution can then be built with a proper linear combination of harmonic solutions.

Inserting 1.3 and 1.4 inside 1.1, with the additional condition of no free charges nor currents, gives the Maxwell equations for the harmonic fields:

$$\nabla \cdot \mathbf{E}(\mathbf{r}) = 0 \tag{1.5a}$$

$$\nabla \cdot \mathbf{H}(\mathbf{r}) = 0 \tag{1.5b}$$

$$\nabla \times \mathbf{E}(\mathbf{r}) + i\mu_0\omega\mathbf{H}(\mathbf{r}) = 0 \tag{1.5c}$$

$$\nabla \times \mathbf{H}(\mathbf{r}) - i\varepsilon\varepsilon_0\omega\mathbf{E}(\mathbf{r}) = 0. \tag{1.5d}$$

Furthermore, the two equations containing the curl can be combined in the following way:

$$\nabla \times \left(\frac{1}{\varepsilon(\mathbf{r})}\nabla \times \mathbf{H}(\mathbf{r})\right) = \left(\frac{\omega}{c}\right)^2 \mathbf{H}(\mathbf{r}) \tag{1.6}$$

where the fact that $c = 1/\sqrt{\varepsilon_0\mu_0} = 299792458$ m s^{-1} (the speed of light in vacuum) has been used.

Equation 1.6, which together with the divergence conditions is equivalent to the Maxwell equations, is sometimes called the *master equation*. It can be easily seen that the master equation assumes the form of an eigenvalue problem for the operator:

$$\Theta(\cdot) = \nabla \times \left(\frac{1}{\varepsilon(\mathbf{r})}\nabla \times \cdot\right). \tag{1.7}$$

Moreover, the operator Θ is Hermitian with respect to the inner product:

$$\langle \mathbf{F}|\mathbf{G}\rangle = \int \mathbf{F}^*(\mathbf{r})\mathbf{G}(\mathbf{r})d\mathbf{r}, \tag{1.8}$$

since it can be proven that:

$$\langle \mathbf{F}|\Theta\mathbf{G}\rangle = \langle \Theta\mathbf{F}|\mathbf{G}\rangle \tag{1.9}$$

provided either one of the following conditions are satisfied: (I) the fields vanish at the boundary of the integration region or (II) the fields satisfy periodic boundary conditions in the integration domain. In addition, the definition of the inner product of Eq. 1.8 provides a very convenient way to fix the normalization of the modes. Since every solution of Eq 1.6 multiplied by a constant is still a solution, it is possible to identify each class of equivalent solutions by its normalized element, defined from an arbitrary solution $\mathbf{F}'$ as:

$$\mathbf{F} = \frac{\mathbf{F}'}{\sqrt{\langle \mathbf{F}|\mathbf{F}\rangle}} \tag{1.10}$$

The possibility to recast Maxwell equations as an hermitian eigenvalue problem is indeed remarkable. It promptly draws a parallelism with quantum mechanics, allowing well known techniques, such as the variational principle or perturbation theory, to be easily applied to electromagnetic problems. Moreover, a great variety of numerical methods have been developed to solve the Schrödinger equation whose application to electromagnetic problems is, in this framework, straightforward.

1.2.2 Discrete translational symmetry

Expressing Maxwell equations in the form of an eigenvalue problem has a very notable consequence: it allows for a very convenient treatment of the system's symmetries. Indeed, it is known from quantum mechanics that if two operators commute with each other, they can be simultaneously diagonalized on the same basis. For two operator $\hat{A}$ and $\hat{B}$ to commute it is sufficient that the commutator operator $[\hat{A}, \hat{B}] = \hat{A}\hat{B} - \hat{B}\hat{A}$ is the same as the null operator.

Therefore, if the master equation's operator $\hat{\Theta}$ commutes with some symmetry operator $\hat{O}$, whose spectrum is usually known, it is possible to extract useful information on the spectrum of $\hat{\Theta}$ from the one of $\hat{O}$, or even use the eigenvalues of $\hat{O}$ to label the solutions to the electromagnetic problem.

More notable symmetries that are usually employed for this scope are inversion symmetries, mirror symmetries, and translational symmetries. The most relevant for the scope of this thesis is translational symmetry, and in particular discrete translational symmetry, which is the fundamental symmetry defining a Photonic Crystals.

Discrete translational symmetry takes place when the dielectric constant profile is invariant under translation by an infinite set of specified vectors

$\{\mathbf{R}\}$. This set can be generated by linear combination, using integer coefficients, of a finite set of linearly independent vectors $\{\mathbf{a}_i\}$ (in number equal to the dimension in which the periodicity extends). The entire collection of $\{\mathbf{R}\}$ is called the Bravais lattice and the related $\{\mathbf{a}_i\}$ are called the primitive vectors, and together they define the periodicity of the lattice.

In this framework, it is useful, before solving the electromagnetic problem, to find the spectrum of all the translation operators $\{\hat{T}_{\mathbf{R}}\}$ corresponding to the vectors $\{\mathbf{R}\}$. To do this, let's first apply the translation operator $\hat{T}_{\mathbf{R}}$ to the simple plane wave $e^{i\mathbf{q}\cdot\mathbf{r}}$:

$$\hat{T}_{\mathbb{R}} e^{i\mathbf{q}\cdot\mathbf{r}} = e^{i\mathbf{q}\cdot\mathbf{R}} e^{i\mathbf{q}\cdot\mathbf{r}}. \tag{1.11}$$

So the plane wave $e^{i\mathbf{q}\cdot\mathbf{r}}$ is an eigenfunction of the operator $\hat{T}_{\mathbf{R}}$ with eigenvalue $e^{i\mathbf{q}\cdot\mathbf{R}}$. It is now worth noting that a different plane wave $e^{i\mathbf{q}'\cdot\mathbf{r}}$ is also an eigenfunction of $\hat{T}_{\mathbf{R}}$ with the same eigenvalue provided that $(\mathbf{q}-\mathbf{q}')\cdot\mathbf{R}$ is a multiple of 2π.

It can be demonstrated that an infinite set of vectors $\{\mathbf{k}\}$ for which $\mathbf{k}\cdot\mathbf{R} = 2\pi n$ for every vector in $\{\mathbf{R}\}$ does exist. This set is called reciprocal lattice, and can be generated, as the direct lattice, by linear combinations with integer coefficient of a set of reciprocal primitive vectors $\{\mathbf{b}_i\}$, which can be generated from the direct primitive vectors by enforcing $\mathbf{a}_i \cdot \mathbf{b}_j = 2\pi\delta_{ij}$.

It is now possible to construct the general eigenfunction of the operators $\{\hat{T}_{\mathbf{R}}\}$ by summing all plane waves whose wavevectors differ by a reciprocal lattice element:

$$\phi_{\mathbf{q}}(\mathbf{r}) = \sum_{\mathbf{k}} c_{\mathbf{q}}(\mathbf{k}) e^{i(\mathbf{q}+\mathbf{k})\cdot\mathbf{r}} = e^{i\mathbf{q}\cdot\mathbf{r}} \sum_{\mathbf{k}} c_{\mathbf{q}}(\mathbf{k}) e^{i\mathbf{k}\cdot\mathbf{r}} = e^{i\mathbf{q}\cdot\mathbf{r}} u_{\mathbf{q}}(\mathbf{r}), \tag{1.12}$$

where $u_{\mathbf{q}}(\mathbf{r})$ is a function with the same periodicity of the direct lattice and $\mathbf{q}$ is called the Bloch vector, and it is related to the eigenvalues with respect to the translation operators $\{\hat{T}_{\mathbf{R}}\}$, which is $e^{i\mathbf{q}\cdot\mathbf{R}}$. Since every Bloch vector which differs by an element of the reciprocal lattice represents the same set of eigenvalues, it is always possible to choose the Bloch vector of minimum modulus. The collection of such Bloch vectors is called the *Brillouin zone* and it is sufficient to represent the full spectrum of the solutions.

At this point the exploitation of symmetry is complete, and it is time to solve the electromagnetic problem. To do this it is sufficient to insert the Bloch function 1.12 inside the master equation 1.6:

$$\hat{\boldsymbol{\Theta}}\phi_{\mathbf{q}}(\mathbf{r}) = \frac{\omega(\mathbf{q})}{c}\phi_{\mathbf{q}}(\mathbf{r}) \tag{1.13a}$$

$$\nabla \times \left(\frac{1}{\varepsilon(\mathbf{r})} \nabla \times e^{i\mathbf{q}\cdot\mathbf{r}} u_{\mathbf{q}}(\mathbf{r}) \right) = \frac{\omega(\mathbf{q})}{c} e^{i\mathbf{q}\cdot\mathbf{r}} u_{\mathbf{q}}(\mathbf{r}) \tag{1.13b}$$

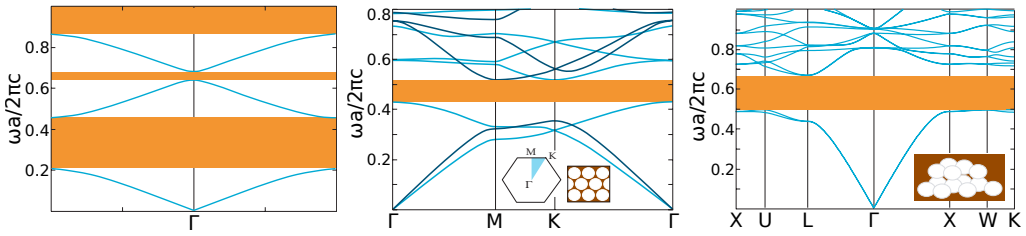

(a) 1D photonic bands: periodic stripes dielectric of thickness $0.2a$ in air.

(b) 2D photonic bands: triangular lattice of air holes in dielectric.

(c) 3D photonic bands: diamond lattice of air spheres in dielectric.

Figure 1.11: Example of photonic bands for different dimension. The dielectric in all three cases is assumed uniform with $\varepsilon = 13$. Photonic Band Gaps are enlightened in orange. Bands reproduced from [170].

$$(i\mathbf{q} + \nabla) \times \left[\frac{1}{\varepsilon(\mathbf{r})} (i\mathbf{q} + \nabla) \times u_{\mathbf{q}}(\mathbf{r}) \right] = \frac{\omega(\mathbf{q})}{c} u_{\mathbf{q}}(\mathbf{r}) \tag{1.13c}$$

$$\hat{\Theta}_{\mathbf{q}} u_{\mathbf{q}}(\mathbf{r}) = \frac{\omega(\mathbf{q})}{c} u_{\mathbf{q}}(\mathbf{r}). \tag{1.13d}$$

In this way, the hard eigenproblem of the master equation is reduced to a collection of independent and simpler eigenproblems, one for every $\mathbf{q}$ in the first Brillouin zone. This conclusion is known as Bloch theorem in solid state physics, while for this application is usually referred as Bloch-Floquet theorem.

In the most common situations the eigenproblem for each $\mathbf{q}$ can be solved to find a (possibly infinite) collection of discrete modes, which are continuous with respect to $\mathbf{q}$ since $\hat{\Theta}_{\mathbf{q}}$ depend continuously on $\mathbf{q}$. This is the origin of the so called Photonic Bands (regions of energy in which propagation of light inside the periodic structure is permitted) and Photonic Band Gap (regions in which is forbidden) — see Fig. 1.11 for some examples of bands.

1.2.3 Photonic Crystal Slabs

A particularly interesting class of periodic structures are the so called Photonic Crystal Slabs [172]. They are composed of a periodically patterned slab of a high index material, acting as the core of a waveguide, embedded in a low index material. It is possible to apply the Bloch theorem to such a structure to obtain the spectrum of modes as a function of the Bloch vector in the plane. Such spectrum is more complex than in standard periodic structures, since it usually features both a discrete and continuous part. Indeed, the spectrum is discrete in the region of the $k\omega$ plane where propagating

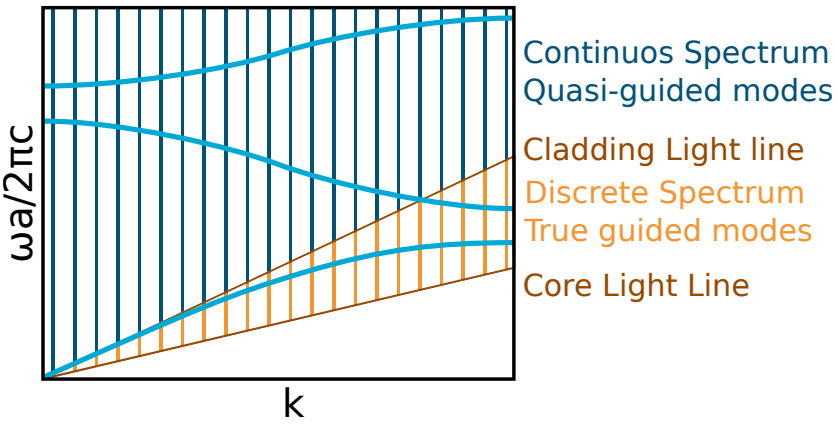

Figure 1.12: Qualitative sketch of typical bandstructure of PhC Slab. True and quasi-guided modes regions are enlightened in orange and blue, respectively.

waves can exist in the core but not in the cladding ($ck/n_{core} < \omega < ck/n_{clad}$) and continuous where propagating waves exist in both core and cladding ($\omega > ck/n_{claddng}$). The separation between these regions is the straight line $\omega = ck/n_{clad}$, called cladding light line.

The discrete modes under the light line are confined to the slab. Furthermore, they ideally propagate without loss, and their possible decay is only due to extrinsic losses, such as disorder or Rayleigh scattering.

The continuous spectrum is mainly composed by radiative modes, namely modes which are not confined to the slab. However, confined modes can extend themselves in the region of continuous spectrum, due to the folding of photonic bands inside the first Brillouin zone. When this happens, the confined modes survive as quasi-guided modes, namely they are broadened by the interaction with radiative modes and acquire a finite lifetime, after which all the energy in the quasi-guided mode is radiated away from the waveguide.

Each region of energy can be used for different applications. True guided modes can be used to tailor light dispersion [173] or create sub-wavelength materials [41].

Quasi-guided modes, although their finite lifetime seems to imply large propagation loss, are quite useful too. They have in fact the unique capacity to couple light between guided and radiative modes. In case of an infinite structure this coupling can be see as a Fano resonance in the transmission and reflection of vertically incident light [174]. If the patterning is truncated some light can survive in the unpatterned waveguide, and a grating coupler in its simplest form is eventually built.

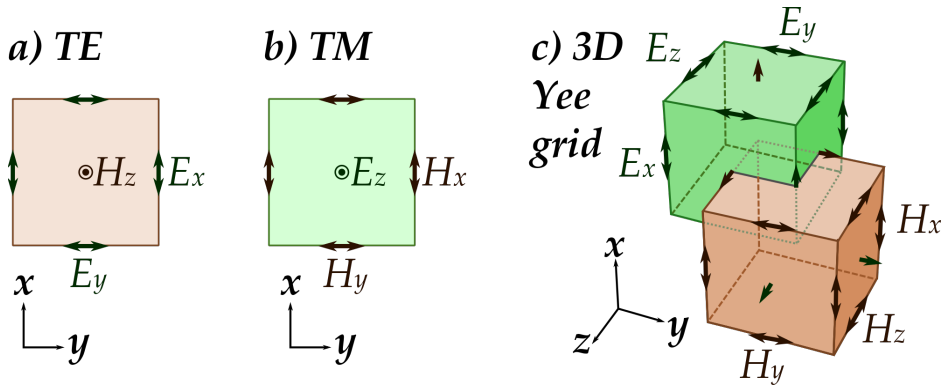

Figure 1.13: Representation of the Yee cell for 2D-FDTD — both polarizations: TM (a) and TE (b) — and 3D-FDTD (c).

Moreover, the ability to create a band gap in a planar structure is very interesting. Creating a complete bandgap is quite trickier than in conventional Photonic Crystals, but by using the right geometry and optimizing it is possible [61, 175]. In particular, once a band gap is in place, inserting a defect is an easy way to create a waveguide [176] or a cavity [98].

1.3 Numerical Methods

The great majority of the simulation during the research work for this thesis was performed with either of two numerical methods: the Finite-Difference-Time-Domain method and two formulations of the Scattering-Matrix method: Rigorous-Coupled-Wave-Analysis (RCWA) and Aperiodic-Fourier Modal Method (AFMM).

For the FDTD method a commercial software, Lumerical FDTD Solutions, was used. On the contrary, regarding the Scattering Matrix, in-house implementations were employed for both formulations: a FORTRAN code for RCWA and a python 2.7 code (which I developed during my PhD) for the A-FMM.

1.3.1 FDTD

The Finite-Difference-Time-Domain (FDTD) method is a numerical procedure to solve Maxwell equations first devised by Kane S. Yee [177] in 1966. The method is based on a discretization of the curl Maxwell equations in the time-space domain, which is used to get the complete time evolution of the electromagnetic field once the initial condition is known [178].

The discretization of the physical fields in time and space takes place over two grids, for electric and magnetic fields, staggered in both space and time — see Fig. 1.13. This structure in the discretization, named Yee's grid, has more than one advantage. Indeed, by using the central difference in the finite-difference expression of the derivatives and a leap-frog algorithm for updating the fields, both precision and stability of the method can be improved. Moreover, once the Maxwell equations containing the divergences are satisfied by the initial condition, this is automatically preserved by the grid's structure during the time evolution.

The main advantage of the FDTD method lies in its versatility. Solving the Maxwell equations in the time-space domain gives complete freedom on the structure, which can be neither periodic nor symmetric, and on the possible sources. Moreover, due to the time domain nature, only one simulation is required to get the broadband response of the structure.

On the drawback side, the FDTD method tends to be computationally expansive and to require post processing of the simulation data to obtain the desired information, such as coupling efficiencies, Q-factors, bandstructures, etc.

During this thesis the FDTD method is used as the main instrument in the research on grating-couplers, mainly due to his versatility and ease of use compared to other methods.

1.3.2 RCWA

Rigorous Coupled Wave Analysis (RCWA) is a frequency domain method based on the Scattering Matrix approach.

The RCWA was developed in his original formulation by D. M. Whittaker and I. S. Culshaw [179] in 1999, to calculate reflection, transmission and even emission from a periodically patterned multilayer. The method was then extended to asymmetric unit cell and birefringent media by M. Liscidini [180], who is also the author of the FORTRAN implementation used for some of the calculations in this thesis.

This method can be used to solve Maxwell equations in any structure, provided it can be represented as a multilayer. Inside each layer, the dielectric constant along the stacking direction (let's call it z) has to be uniform. Variation of the dielectric constant in the plane perpendicular to the stacking direction (the xy) plane is instead permitted, as long as it is periodic on the same Bravais lattice for every layer. Although these constraints could seem a little restrictive, the class of structures that can be analyzed is quite big. Full 3D structures in fact can be analyzed performing a staircase approximation along a specified direction [181], and then checking the convergence with the

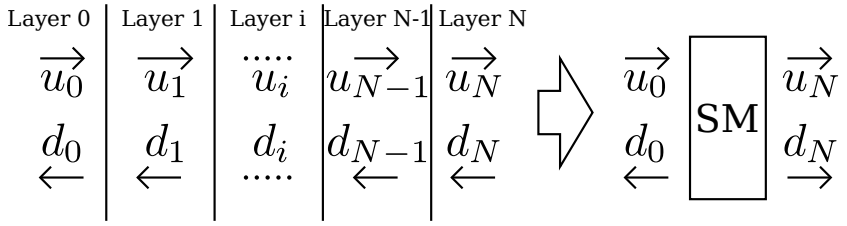

Figure 1.14: scattering matrix

number of slices in the approximation.

The basic working principle is as follows. Firstly, the fields in each layer (for now assumed infinite in the z direction) are expressed as a sum of forward and backward propagating plane waves (expansion on a Fourier basis). Secondly, the boundary conditions are applied to each interface, linking together the fields between adjacent layers. The output of the code is the scattering matrix S, a matrix that connects the Fourier expansion of the fields outgoing from the structure to the one of the incoming fields:

$$\begin{bmatrix} u_N \\ d_0 \end{bmatrix} = S \begin{bmatrix} u_0 \\ d_N \end{bmatrix} = \begin{bmatrix} S_{11} & S_{12} \\ S_{21} & S_{22} \end{bmatrix} \begin{bmatrix} u_0 \\ d_N \end{bmatrix} \tag{1.14}$$

where u_i and d_i are the coefficient of the Fourier expansion in the i^{th} layer for the forward and backward propagating waves.

If a total of M elements of the Fourier expansion are retained, each u_i and d_i is a $2M$ vector (the factor 2 account for the two different polarization states) and the scattering matrix S is a $4M \times 4M$ matrix.

Once the scattering matrix of a system is known, information such as reflection, transmission and diffraction in the open orders can be extracted. Since the scattering matrix gives the coupling coefficient between the input and output Fourier modes, getting such information is just a matter of taking the correct element in the scattering matrix and normalizing it with the ratio between the Poynting vectors of the selected modes.

During this thesis, the RCWA method is mainly employed in the research on grating couplers, in particular regarding the problem of the bandwidth.

1.3.3 A-FMM

The Aperiodic-Fourier Modal (A-FMM) method is conceptually similar to the RCWA but, thanks to the addition of a coordinate transformation in the unit cell, the periodicity condition in the xy plane is no longer required. Thus, the treatment of aperiodic structures, such as rib or grating waveguides, is

possible. A more detailed description of this method will be given, since I spent part of my PhD implementing a Python version of this method.

The A-FMM has its roots in the classical modal method for crossed gratings, firstly devised by L. Li [182] in 1997. The method was then updated by J.P. Hugonin and P. Lalanne [183] with the inclusion of a coordinate transformation. The role of the coordinate transformation is to map the entire $\mathbb{R}$ space ($\mathbb{R}^2$ for 3D calculation) to the finite computational cell. In this way, the computational cell can contain an arbitrary dielectric constant distribution, which can still be treated with Fourier Methods but without crosstalk between adjacent cells. For more details on the theory beyond the coordinate transformation see App. A.

The procedure involved in the A-FMM is basically the same of the RCWA, and can be summarized as:

1. Divide the system in N layers.
2. Solve the Maxwell equations in each layer, assuming homogeneity in the staking (z) direction and expanding the filed on a Fourier basis.
3. Using the solution found in 2, calculate the propagation matrix in each layer and the scattering matrix of each interface.
4. Using the recursion algorithm for the scattering matrix, calculate the scattering matrix of the full structure.
5. Obtain the desired quantities by post-processing of the scattering matrix.

A brief summary of every step will now be reported. Firstly, it is necessary to expand the fields in each layer as a sum over pseudo-Fourier basis :

$$\Phi(x,y,z) = \sum_{n,m} = \Phi_{n,m}(z) \exp\left\{ i(k_x + \frac{2\pi n}{L_x})x + i(k_y + \frac{2\pi m}{L_y})y \right\} \quad (1.15)$$

where Φ is a generic component of the electromagnetic fields, k_x, k_y are the components of the wavector along the x, y direction. The values L_x and L_y are the dimensions of the computational cell. Due to the coordinate transformation they lack a physical meaning, but their values are still important in the definition of the basis for the pseudo-Fourier expansion, and remain as computational parameters.

Once the expansion is established, it can be inserted in the Maxwell equations to get the solutions inside the single layer. After this substitution and a little manipulation it is possible to write:

$$-\frac{i}{k_0}\frac{\partial}{\partial z}\begin{bmatrix} E_x \\ E_y \end{bmatrix} = \begin{bmatrix} \bar{K}_x\varepsilon^{-1}\bar{K}_y & 1-\bar{K}_x\varepsilon^{-1}\bar{K}_x \\ \bar{K}_y\varepsilon^{-1}\bar{K}_y - 1 & -\bar{K}_y\varepsilon^{-1}\bar{K}_x \end{bmatrix}\begin{bmatrix} H_x \\ H_y \end{bmatrix} = F\begin{bmatrix} H_x \\ H_y \end{bmatrix} \tag{1.16a}$$

$$-\frac{i}{k_0}\frac{\partial}{\partial z}\begin{bmatrix} H_x \\ H_y \end{bmatrix} = \begin{bmatrix} -\bar{K}_x\bar{K}_y & \bar{K}_x{}^2 - \varepsilon_{y,x} \\ \varepsilon_{x,y} - \bar{K}_y{}^2 & \bar{K}_x\bar{K}_y \end{bmatrix}\begin{bmatrix} E_x \\ E_y \end{bmatrix} = G\begin{bmatrix} E_x \\ E_y \end{bmatrix} \tag{1.16b}$$

where E_x, E_y, H_x, H_y are the vectors containing the Fourier expansion coefficients of the respective field, and $k_0 = \omega/c$ is the vacuum wavevector of the radiation. The matrices $\varepsilon, \varepsilon_{x,y}$ and $\varepsilon_{y,x}$ are built with the Fourier transform of the dielectric function in the computational cell — see ref. [182] and App. A for further details. The matrix $\bar{K}_x$ is built as:

$$\bar{K}_x = F_x K_x, \tag{1.17}$$

where K_x is simply the matrix containing the wavevectors of the Fourier expansion ($K_x(g, g') = (k_x + g_x)\delta_{gg'}$) and F_x is built from the Fourier coefficient of the derivative of the function used for the coordinate transformation — see App A for details. The matrix F_y is built in an analogous way.

A further summary of Eq. 1.16a and 1.16b is desirable. Focusing on solutions of Φ which have a z dependence in the form $e^{i\gamma z}$ it is possible to write:

$$FG\begin{bmatrix} E_x \\ E_y \end{bmatrix} = \frac{\gamma^2}{k_0^2}\begin{bmatrix} E_x \\ E_y \end{bmatrix}, \tag{1.18}$$

which takes the form of an eigenvalue problem concerning only the electric field components. The eigenvalues γ^2/k_0^2 are related to the propagation constant along z of the eigenmodes of the layer, while the eigenvectors give the electric field profile of the modes. Since for every eigenvalue two solutions for γ are possible — forward and backward propagating — only the solution satisfying $Re(\gamma) + Im(\gamma) > 0$ will be considered and labeled with subscript q.

Defining the vector $E = [E_x E_y]^T$ and the matrix $\tilde{E}$ containing as columns the eigenvectors of Eq. 1.18, the corresponding matrix $\tilde{H}$ for the magnetic field can be expressed as:

$$\tilde{H} = \frac{k_0}{\gamma}\tilde{E} \tag{1.19}$$

which contains the Fourier coefficients relative to the magnetic field of the eigenmodes.

At this point it is possible, after the definition of the vectors u and d, containing, respectively, the amplitude of the forward and backward propagating modes inside the layer, to write the Fourier coefficients of the fields

at an arbitrary value z as a function of u and d:

$$\begin{bmatrix} E \\ H \end{bmatrix}_z = \begin{bmatrix} \tilde{E} & \tilde{E} \\ \tilde{H} & -\tilde{H} \end{bmatrix} \begin{bmatrix} u \\ d \end{bmatrix}_z . \tag{1.20}$$

Currently, a method of connecting the vectors u and d at different z values (both in the same layer or in different ones) is still lacking. In the following, the scattering matrix for both cases will be built.

The easiest case is when the two values of z are in the same layer. In this condition, the values of u and d at z and z' are simply linked with a propagation scattering matrix:

$$\begin{bmatrix} u' \\ d \end{bmatrix} = \begin{bmatrix} \exp[i\Gamma(z-z') & 0 \\ 0 & \exp[i\Gamma(z-z')] \end{bmatrix} \begin{bmatrix} u \\ d' \end{bmatrix} \tag{1.21}$$

where Γ is simply the matrix with the propagation constants of the modes γ on the diagonal.

When the two z values lie in different layers the calculations are a bit more complex. However, is it possible to demonstrate that the scattering matrix of a single interface between two layers can be written as (normal variables refer to the first layer, the primed to the second):

$$\begin{bmatrix} S_{11} & S_{12} \\ S_{21} & S_{22} \end{bmatrix} = \begin{bmatrix} T_+ - T_- T_+^{-1} T_- & T_- T_+^{-1} \\ -T_+^{-1} T_- & T_+^{-1} \end{bmatrix}, \tag{1.22}$$

where $T_\pm$ is defined as:

$$T_\pm = \frac{1}{2}\left({\tilde{E}'}^{-1} \tilde{E} \pm {\tilde{H}'}^{-1} \tilde{H} \right). \tag{1.23}$$

Now that both propagation and interface scattering matrices are defined, in order to connect the u and d vectors at different z values all that is needed is a recursion algorithm to join together two matrices, allowing the scattering matrix of the complete system to be built up piece by piece. In details, the recursion algorithm joining to scattering matrices S and s in the total scattering matrix S^T is:

$$S_{11}^T = s_{11}(1 - S_{12}s_{21})^{-1} S_{11} \tag{1.24a}$$

$$S_{12}^T = s_{12} + s_{11}(1 - S_{12}s_{21})^{-1} S_{12}s_{22} \tag{1.24b}$$

$$S_{21}^T = S_{21} + S_{22}(1 - s_{21}S_{12})^{-1} s_{21}S_{11} \tag{1.24c}$$

$$S_{22}^T = S_{22}(1 - s_{21}S_{12})^{-1} s_{22} \tag{1.24d}$$

It is worth noting that this relation, together with the fact that no diverging exponential appears in the propagation matrix 1.21, ensures the numerical stability of the S-matrix, at variance with other schemes (i.e. T-matrix).

Once the scattering matrix of the entire system is known, information such a coupling strength between one input mode and one output mode are easily calculated. As an example, the fraction of power scattered from a mode m to a mode n can be calculated as:

$$\frac{P_n}{P_m} = |S(n,m)|^2 \frac{\mathcal{P}_n}{\mathcal{P}_m}, \tag{1.25}$$

where $S(n,m)$ is the relevant S-matrix element and the quantity $\mathcal{P}_i$ is the z-component of the Poyting vector referring to the i mode. This component can be calculated as:

$$\mathcal{P} = \frac{1}{2} Re\left[E_x^T H_y^* - E_y^T H_x^*\right], \tag{1.26}$$

where E_x, E_y, H_x and H_y are the vectors of the Fourier components of the mode under consideration.

Speaking of the Poynting vector, it is also possible to calculate the total Poynting vector as a function of z. This is a little more complex than before (where only the Poyting vector relative to a single mode was calculated) since now all modes (forward and backward propagating), together with their interference, have to be considered. In the end, the total Poyting vector $\mathcal{P}_z^{TOT}$ can be expressed as:

$$\mathcal{P}_z^{TOT} = \frac{1}{2} Re\left\{ \begin{bmatrix} u & d \end{bmatrix}_z \begin{bmatrix} \tilde{\mathcal{P}} & -\tilde{\mathcal{P}} \\ \tilde{\mathcal{P}} & -\tilde{\mathcal{P}} \end{bmatrix} \begin{bmatrix} u^* \\ d^* \end{bmatrix}_z \right\} \tag{1.27}$$

where $\tilde{\mathcal{P}}$ is a matrix whose elements are defined as:

$$\tilde{\mathcal{P}}_{nn'} = \sum_k \left[\tilde{E}_x(k,n) \tilde{H}_y^*(k,n') - \tilde{E}_y(k,n) \tilde{H}_x^*(k,n') \right]. \tag{1.28}$$

However, the practical use of Eq. 1.27 to get the total Poyting vector requires the calculation of u_z and d_z, namely the vectors containing the coefficients of the forward and backward propagating modes at z. In order to do that, two S-matrices have to be built. The first S is the matrix linking the beginning of the structure to the desired z coordinate, while the second S' links this z coordinate to the end of the structure. Once those S-matrices are known, the vectors u_z and d_z can be calculated from the input vector u and d' as:

$$u_z = \left(1 - S_{12} S'_{21}\right)^{-1} \left(S_{11} u + S_{12} d'\right) \tag{1.29a}$$

$$d_z = \left(1 - S'_{21}S_{12}\right)^{-1}\left(S'_{21}u + S'_{22}d'\right). \tag{1.29b}$$

One last, but very important, application of the scattering matrix is the calculation of the photonic bands in periodic structures. This can be done by solving a generalized eigenvalue problem derived from the S-matrix of the unit cell. The eigenvalue problem is obtained by imposing Bloch boundary conditions on the fields at the two side of the structure:

$$\begin{bmatrix} u' \\ d' \end{bmatrix} = e^{ik\Lambda} \begin{bmatrix} u \\ d \end{bmatrix} \tag{1.30}$$

where k and Λ are the Bloch vector and the period along the z direction, respectively. Inserting the Bloch boundary condition in the definition of the scattering matrix (Eq. 1.14) easily yields:

$$\begin{bmatrix} S_{11} & 0 \\ S_{21} & -1 \end{bmatrix} \begin{bmatrix} u \\ d \end{bmatrix} = e^{ik\Lambda} \begin{bmatrix} 1 & -S_{12} \\ 0 & -S_{22} \end{bmatrix} \begin{bmatrix} u \\ d \end{bmatrix}, \tag{1.31}$$

which can be solved to obtain the Bloch vector k for given frequency.

The Aperiodic Fourier Modal Method is the main instrument for the research on slow-light in silicon grating waveguides, both for calculation of photonic bands and transmission through finite size structures.

Chapter 2

Grating-Couplers: lineshape and bandwidth

2.1 Introduction

One of the major problems Silicon Photonics has encountered, and still faces today, is the connection of an Integrated Photonic Circuit to the external world. This is a complex task, in general involving both optical and electrical connections, along with thermal management, and goes by the name of Photonic Packaging [184]. On the optical side, the coupling of light between an integrated waveguide and an optical fiber, the preferred medium for mid- and long-distance communication, has posed a substantial challenge.

The reason of such difficulty is mainly due to the large mode mismatch between the two types of waveguides. Silicon integrated waveguides are indeed, thanks to the high index contrast typically available, very efficient in confining light to lateral dimensions comparable to the wavelength (few hundreds of nanometers). On the contrary, the low refractive index contrast available in optical fibers makes the core of even a single-mode fiber quite large, with a diameter of the order of 10 µm.

This mismatch causes high losses every time a direct connection between the two systems is attempted. To solve this problem many solutions have been proposed, but almost all can be classified as either edge-coupling or grating-coupling.

2.1.1 Edge-coupling

Edge-coupling is the natural evolution of direct butt-coupling. The idea behind edge-coupling is to place some sort of interposer between the optical

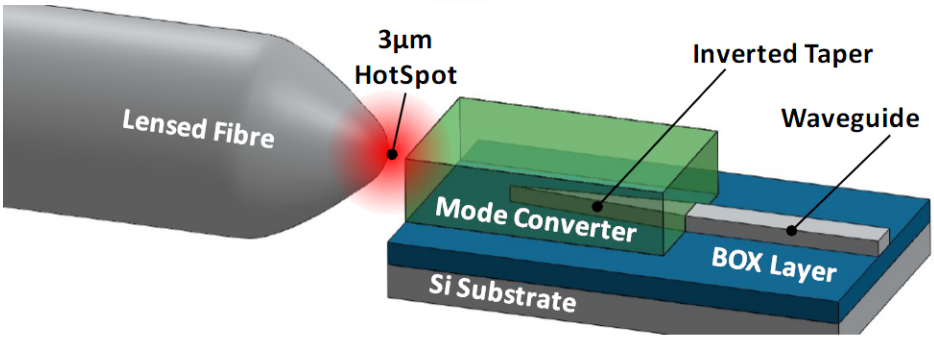

Figure 2.1: Representation of the typical structure of an edge-coupler in SOI platform. Image reproduced from [184].

fiber (or some other source, such as a laser) and the integrated silicon waveguide. The role of this interposer — see Fig. 2.1 — is to gradually adjust the effective index and the size of the mode between the fiber and the waveguide.

Several solutions have been proposed over the years. The most straightforward is the realization of an inverted taper in the silicon waveguide. Indeed, as the width of the integrated waveguide is reduced, so are the effective index of the mode and its localization, yielding a wider mode with a profile which is similar to the one of an optical fiber. Since it is difficult to fully compensate the modal mismatch relying only on the inverse taper, it is often embedded in a spot-size converter [185], made either of SiON or some organic polymer, which makes the transition even more gradual by adding an extra step. Further improvements can be achieved by shrinking the mode at the fiber side, thus reducing the size mismatch, for example by employing lensed or High Numerical-Aperture optical fibers [186]. Overall, this solution can indeed deliver impressing performances, both for fiber-to-chip [187, 188, 189] and laser-to-chip coupling [190].

Another viable way it is to employ sub-wavelength structures. In this framework, the index of the mode is adapted not by shrinking the waveguide, but by modifying the pitch and duty cycle of a sub-wavelength patterned waveguide, which thus acts as a normal waveguide with a tunable index [44, 114]. This solution allows for a finer control of the modal index and mitigate the minimal feature size problem. Done properly, it can achieve very high coupling efficiency (>90%), along with very high bandwidth (>100 nm) and polarization insensitive operation [191].

The main drawbacks of edge-coupling are the complexity of the fabrication, which requires extra thin-features [192] and a possible extra step for the realization of the spot converter, together with the higher post-processing cost, in particular for the dicing and polishing of the chip's edge. Moreover,

alignment tolerance is usually sub-µm [193] and, due to placement of the coupling element one the edge, wafer-scale testing is not possible.

Thus, all these features make edge-coupling a non-ideal solution to the fiber-to-chip problem in Silicon Photonics, although it has demonstrated to be a valid candidate for some commercial applications, such a direct laser-to-fiber coupling [186], and for research purposes.

2.1.2 Grating-coupling

Grating-coupling takes a completely different approach. A grating-coupler consists in a simple diffraction grating etched in a planar waveguide. In this way, light incident on the chip almost vertically can be coherently scattered inside the waveguide. Grating-couplers offer some practical improvement over edge-couplers. They are usually easier to fabricate since, although sometimes additional deposition of poly-silicon is required, they can usually be built with a single etching step [194]. Moreover, since they couple light that arrive vertically on the chip, they can be placed anywhere, adding a great deal of flexibility to the design of the circuit, which now does not require any expansive polishing of the edges. In addition, they usually exhibit more relaxed alignment tolerances, up to 5 µm, and passive alignment can be easily employed.

All these interesting features usually result in lower performances than edge-couplers. The problem is not so much on maximum coupling efficiency, although careful optimization is needed to bring grating-coupler's efficiency to acceptable levels. Instead, the spectral bandwidth can be the real bottleneck. Indeed, since grating-couplers are based on a resonant phenomenon, their bandwidth is intrinsically limited, usually of the order of 30-40 nm when operating at telecom wavelengths. Moreover, simpler 1D grating-couplers are polarization sensitive, and can efficiently couple only one polarization, which is usually designed to be the TE polarization of the waveguide. This is not a problem for out-coupling, when the polarization of light coming from the PIC is fixed, but it is a problem for in-coupling, since polarization of light from the fiber is usually not well defined. Polarization insensitive couplers, which couple the different polarizations either to two different TE waveguides [67] or to TE and TM modes in the same waveguide [68], do exist, but requires 2D patterning and their performance is usually lower than 1D counterparts.

In this chapter a numerical analysis of the grating-couplers' performances will be presented, with particular attention to the problem of the bandwidth and its relation with the intrinsic width of the photonic mode inside the grating. In addition, a simultaneous optimization of coupling efficiency and bandwidth will be performed. All grating-couplers here are considered in the

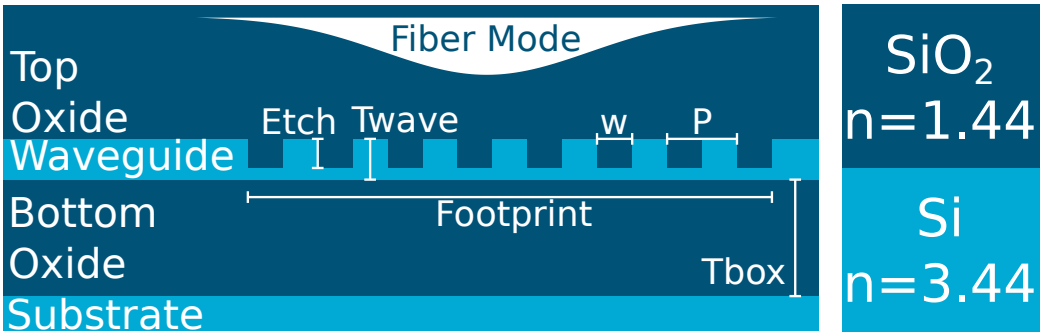

Figure 2.2: Sketch of the structure of an uniform grating coupler. All relevant parameter are defined, except for the duty cycle DC=w/P and the Mode Field Diameter, namely two times the σ of the Gaussian Mode used as fiber excitation.

standard SOI platform with 220 nm waveguide thickness and operating at the standard telecom wavelength of 1.55 µm.

2.2 The physics of grating-couplers

One dimensional grating-couplers are simply composed by a series of grooves etched inside a silicon planar wavequide in the chip. They are usually around 10-15 µm long, to match the 10.4 µm Mode Field Diameter (MFD) of commercial single-mode optical-fibers at the standard telecom wavelength of 1.55 µm. The silicon waveguide is usually embedded in silica (SiO_2) and all is supported by a Si substrate. The simplest grating-coupler — see Fig. 2.2 — is composed by a uniform grating, and it is defined by a limited set of parameters: the waveguide thickness Twave, the period of the grating P, the etching depth Etch, the duty cycle DC (the ratio between the etched part and the period), and the thickness of the bottom oxide Tbox. In principle one must consider also the thickness of the top oxide above the grating. This will be discarded here both for simplicity and because it has usually the same index of refraction of the optical fiber and of the epoxy glue used to make the connection, so in all practical calculations can be assumed semi-infinite. The fiber mode can be assumed to be a Gaussian Beam coming from above the waveguide with an angle θ. The width of such Gaussian is summarized in the Mode Field Diameter (MFD), namely the width at which the field is reduced to $1/e$ of the maximum value.

There are mainly two pictures in which to understand the operation of a grating-coupler: the theory of diffraction gratings and the theory of Photonic

Crystal Slabs.

The theory of diffraction gratings states that, when light is incident on a periodic patterned structure, the coherent scattering of every element gives rise, besides the standard transmitted and reflected wave, to additional scattered waves. The angular distribution of such waves is determined only by the period of the grating, and can be calculated by applying the condition of momentum conservation in the direction parallel to the grating. The parallel wavevector of the m^{th} diffraction order $k_{\parallel}^{m}$ is related to the parallel incident wavevector $k_{\parallel}^{inc}$ by:

$$k_{\parallel}^{m} = k_{\parallel}^{inc} + \frac{2\pi}{\Lambda} m \tag{2.1}$$

where Λ is the period of the grating. The order is open when waves of such wavevector can propagate in the outside medium, namely $k_{\parallel}^{m} < 2\pi/\lambda n$, otherwise it is closed and no light can scatter in that order — see Fig. 2.3. While the position of the orders does not depend on the particular geometry of the grating, how the light divides itself in the different orders does, and a complete calculation of the scattering from a periodic structure usually requires dedicated numerical methods (such a RCWA).

Coupling inside the waveguide is possible when the parallel wavevector of one diffraction order (usually $m = +1$) coincides with the wavevector of the guided mode inside the grating. Since the wavevector of the guided mode can be written as $k_0 n_{eff}$, where n_{eff} is the effective phase index of the guided mode and k_0 is the vacuum wavevector, Eq. 2.1 can be rewritten in the classical Bragg condition for grating-couplers:

$$k_0 n_{eff} = k_0 n_t \sin(\theta) + \frac{2\pi}{\Lambda} \tag{2.2}$$

where n_t and θ are the refractive index of the top oxide and the angle of incidence of the light, respectively. This equation can be used, once the effective index of the waveguide is somehow known, to relate the period and the coupling angle of the grating.

In this framework, coupling of light to an infinite grating is ideally possible only with no bandwidth. This because Eq. 2.2, at fixed angle, can be satisfied only at one single wavelength. The coupling bandwidth here arises as a finite size effect. A finite size excitation, in fact, contains multiple parallel wavevectors even when restricted to a single wavelength. In this way, Eq. 2.2 can be satisfied at different $k_{\parallel}^{inc}$ for different wavelengths, and as long as there is power in the corresponding $k_{\parallel}^{inc}$ mode, some of it can be coupled inside the grating.

To calculate the k-spread, let's start with a Gaussian excitation at a fixed

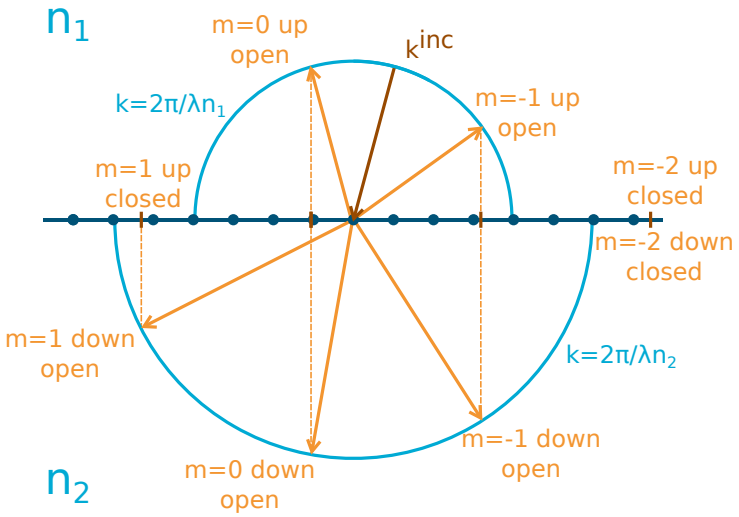

Figure 2.3: Graphical representation of the diffraction orders of a generic grating.

frequency and at normal incidence with the normalized field amplitude:

$$E(x) = \frac{1}{\sqrt{\sqrt{\pi}\sigma}} e^{-\frac{x^2}{2\sigma^2}}, \tag{2.3}$$

where the normalization factor is chosen to normalize the total power, namely:

$$\int_{-\infty}^{\infty} E^2(x)dx = 1. \tag{2.4}$$

From Eq. 2.3 it is possible to extract the k amplitude by simply applying a Fourier transform:

$$\tilde{E}(k) = \frac{1}{\sqrt{2\pi}} \int_{-\infty}^{\infty} E(x)e^{-ikx}dx, \tag{2.5}$$

which, after some manipulation, leads to:

$$\tilde{E}(k) = \sqrt{\frac{\sigma}{\sqrt{\pi}}} e^{-\frac{k^2\sigma^2}{2}}. \tag{2.6}$$

It is worth noting that the total power is preserved when going from the position space to the wavevector space, as it is straightforward to show that:

$$\int_{-\infty}^{\infty} \tilde{E}^2(k)dk = 1 \tag{2.7}$$

Then, generalizing to multiple frequencies and arbitrary incidence (basically selecting a specific $k^{inc} = k^{inc}(\omega)$), the k-spectrum of the exciting field can be written as:

$$\tilde{E}(k,\omega) = \sqrt{\frac{\sigma}{\sqrt{\pi}}} e^{-\frac{(k^{inc}(\omega)-k)^2\sigma^2}{2}}. \tag{2.8}$$

However, a more complete discussion must resort to the full theory of Photonic Crystals Slabs [170]. In this framework, the grating-coupler action can be understood in terms of coupling between a radiative mode (the incident light) and a quasi-guided mode of the grating waveguide [174]. In this picture, the photonic bands inside the waveguide are folded inside the first Brillouin zone by the periodic patterning, so the energy and wavevector conservation can be satisfied without the addition of any wavevector — see Fig. 2.4.

At this point, the Gaussian contribution to the bandwidth can be calculated geometrically in a simple way. Indeed, a k-spread in the excitation can be translated in a ω-spread simply by:

$$\Delta\omega = \frac{\partial\omega}{\partial k}\Delta k = \frac{c}{n_g}\Delta k \tag{2.9}$$

where n_g is the group index of the waveguide. At this point, remembering that with the notation of Eq. 2.3 MFD=$2\sqrt{2}\sigma$, it is possible to derive the Gaussian contribution to the bandwidth in the form:

$$\frac{\sigma_\omega}{\omega} = \frac{\sqrt{2}\lambda}{\pi n_g MFD} \tag{2.10}$$

where both sides have been defined as dimensionless quantities. From this equation it is possible to show that the Gaussian contribution to the bandwidth depends more on the excitation than on the grating, and is inversely proportional to the Mode Field Diameter of the fiber mode.

Moreover, in this framework another contribution to the bandwidth can be seen. The photonic mode inside the waveguide has indeed an intrinsic width given by the fact that, as a quasi-guided mode, it has a finite lifetime. The final bandwidth of a grating coupler is thus composed by the interplay of these two factors. The first part of the chapter will be devoted to the numerical analysis of such interplay.

Some studies can be found in the literature on the bandwidth of grating-couplers [195]. However, a systematic study on how the two different contributions concur in the formation of the bandwidth has not, to my knowledge, been reported.

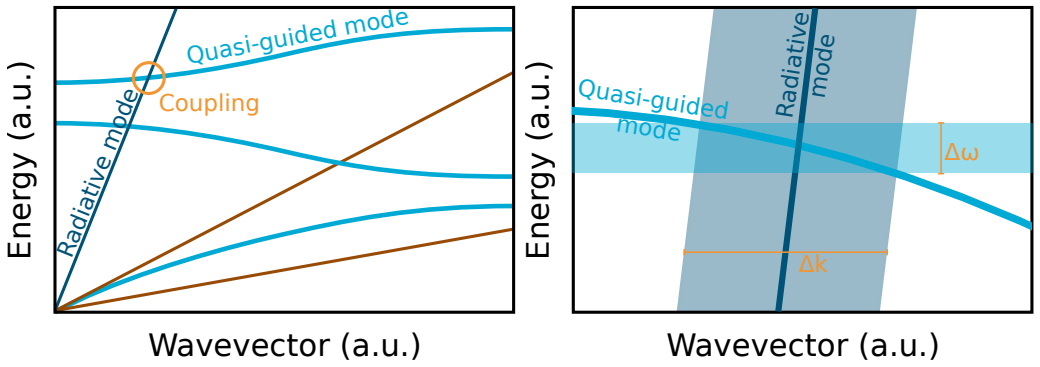

(a) Sketch of the band structure leading to the coupling.

(b) Sketch of the mechanism behind the k-spread contribution to the bandwidth.

Figure 2.4: Sketch of bandstructure of a grating-coupler and k-spreading of the incident beam.

2.2.1 Results from coupling spectra

Here, the FDTD method is used to simulate the coupling spectra of uniform grating-couplers with different sets of parameters. The aim is to shed new light on the mechanism behind the bandwidth formation, by using the MFD as a control parameter in order to change the relative strengths of the two physical contributions to the bandwidth. The hope is thus to isolate each single contribution by analyzing the coupling spectrum. In particular, the DC values of 25%, 50%, and 75% are analyzed, together with various etching depths — from 20 nm to full etch with 20 nm interval — while the Tbox is kept fixed at 2 µm for simplicity. Each parameter configuration is analyzed for a MFD range from 10 to 150 µm, and the ratio between the Fiber Offset FIB and the MFD is kept constant at 0.47. The angle of incidence θ is 10° and the central wavelength is 1.55 µm.

Some of the raw data obtained by this sweep are reported in Fig. 2.5, where coupling efficiency and Full-Width-Half-Maximum (or 3-dB bandwidth) are reported as a function of MFD for some of the analyzed configurations. A few general properties and trends can be noted.

First of all, regarding the behavior of coupling efficiency, it can be seen that the absolute maximum is similar between the configurations, just above 50%. However, this maximum is achieved at different MFD values for different combinations of parameters. In particular, the stronger the scattering-strength — which is increased by increasing etching depth or moving the DC toward 50% — the lower the optimal MFD. This can be intuitively explained by considering that increasing the scattering-strength reduces the

distance light can travel inside the grating before being scattered away, i.e. the mean free path of the radiation. Light which is injected inside the grating at a distance from the edge greater than this mean free path is doomed to be scattered away before reaching the waveguide and to be lost. Thus, extending the MFD beyond a certain limit forcefully decreases the coupling efficiency, as it increases the portion of light which cannot be collected.

Regarding the FWHM, a quite general and simple trend emerges. In particular, the FWHM monotonically decreases on increasing MFD, till it reaches a saturation value, different for each configuration. The decrease of the bandwidth is expected by the finite size effect, but the saturation effect indicates that some other mechanism — the intrinsic width of the guided mode, as shown below — is relevant here.

Another indication that the bandwidth is the product of the interplay of at least two factors comes from the analysis of the coupling spectra. The shape of the coupling does indeed show an evolution as the MFD increase. For small MFD, i.e. till the maximum in CE, the spectrum can be fitted quite well with a Gaussian. For large MFD, i.e. after bandwidth saturation, the spectrum is well fitted by a Lorentzian. In the intermediate region, neither Gaussian neither Lorentzian are able to fit well the spectrum, and a Voigt lineshape, which is a convolution between the two, is needed for a correct reproduction of the obtained results.

The fitting procedure is carried out with a Python script. For the Gaussian and Lorentzian fits the conventional normalized forms are taken:

$$G(x, A, \sigma, x_0) = \frac{A}{\sqrt{2\pi}\sigma} e^{-\frac{(x-x_0)^2}{2\sigma^2}} \tag{2.11a}$$

$$L(x, A, \Gamma, x0) = \frac{A\Gamma}{\pi[(x-x_0)^2 + \Gamma^2]} \tag{2.11b}$$

while the Voigt function is expressed by use of the Feeddeva function $w(x)$ available as `scipy.special.wofz`:

$$V(A, \sigma, \Gamma, x_0) = \frac{A}{\sqrt{2\pi}\sigma} Re\left[w\left(\frac{x - x_0 + i\Gamma}{\sqrt{2}\sigma}\right)\right] \tag{2.12}$$

Some results of this fitting procedure are reported in Fig. 2.6 and 2.7 — fitting parameters are reported in Tab. 2.1 and 2.2 — where the spectral evolution is evident. The interpretation is that at smaller MFD the finite size effect dominates, thus giving a Gaussian spectrum. Moving to larger MFD, the finite size effect gradually vanish, giving a Voigt function when the two contributions are of almost equal magnitude, and then leaving only the intrinsic Lorentzian width of the photonic mode once the MFD is large

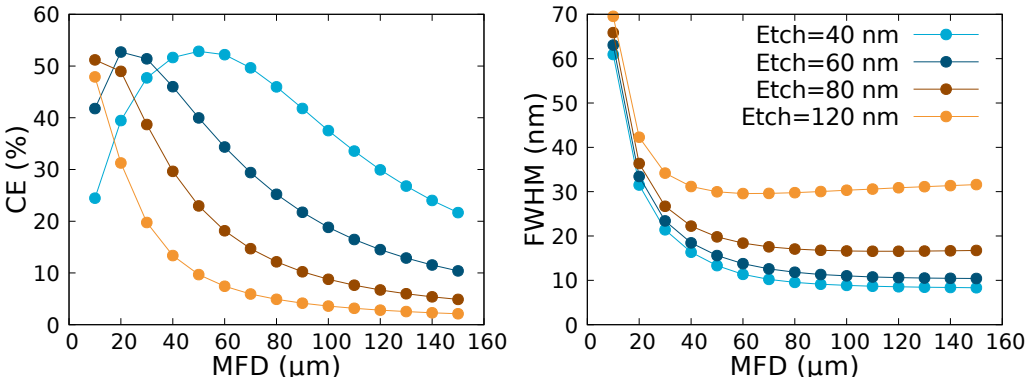

(a) DC=25%.

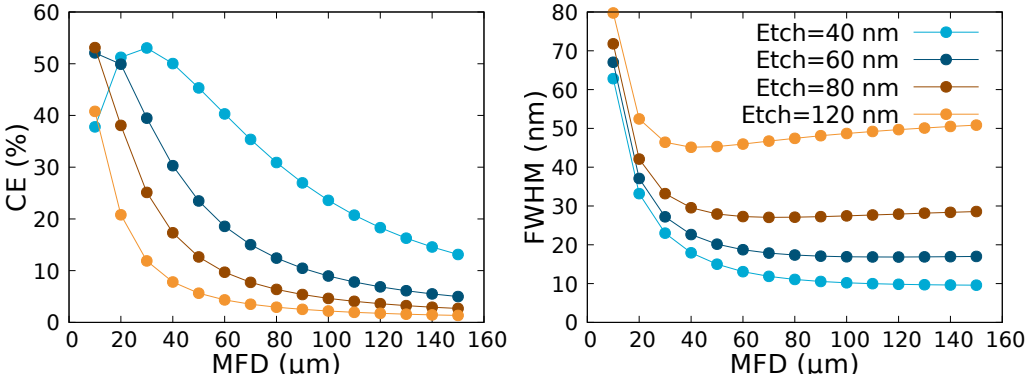

(b) DC=50%.

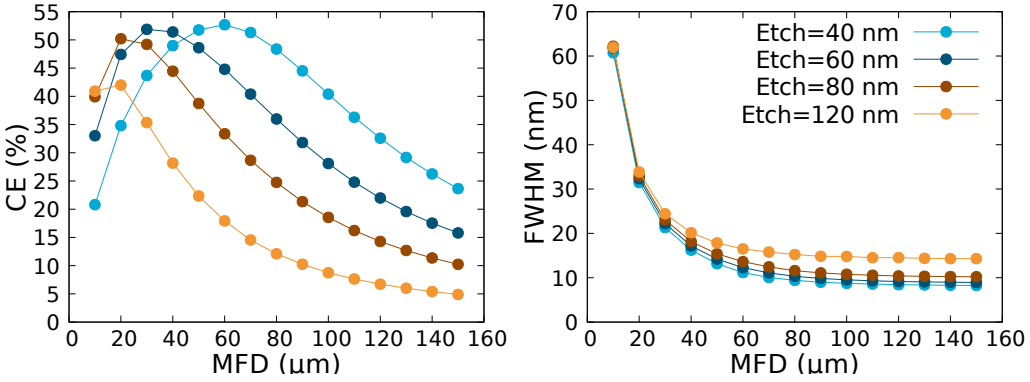

(c) DC=75%.

Figure 2.5: Representation of coupling efficiency (CE — left) and Full-Width-Half-Maximum (FWHM — right) for uniform grating-couplers with different combinations of parameters.

DC	Etch	MFD	Gauss Fit			Lorentz Fit		
DC	Etch	MFD	A	σ	x_0	A	Γ	x_0
25	80	10	1.84e-2	1.42e-2	8.00e-1	2.33e-2	1.33e-2	8.00e-1
25	80	50	2.60e-3	4.69e-3	7.99e-1	3.36e-3	4.39e-3	7.99e-1
25	80	150	5.02e-4	4.49e-3	7.99e-1	6.53e-4	4.18e-3	7.99e-1
50	40	10	1.29e-2	1.35e-2	8.00e-1	1.64e-2	1.26e-2	7.99e-1
50	40	40	4.97e-3	3.98e-3	7.99e-1	6.33e-3	3.72e-3	7.99e-1
50	40	150	7.10e-4	2.19e-3	7.99e-1	9.24e-4	2.09e-3	7.99e-1

Table 2.1: Parameter of the Gaussian and Lorentzian fits for the data shown in Fig. 2.6 and 2.7. The parameters are defined in Eq. 2.11a and 2.11b.

DC	Etch	MFD	Voigt Fit			
DC	Etch	MFD	A	Γ	σ	x_0
25	80	10	1.84e-2	5.54e-6	1.42e-2	8.00e-1
25	80	50	3.00e-3	2.34e-3	3.14e-3	7.99e-1
25	80	150	6.41e-4	3.89e-3	1.10e-3	7.99e-1
50	40	10	1.28e-2	3.42e-4	1.37e-2	8.00e-1
50	40	40	5.21e-3	6.70e-4	3.59e-3	7.99e-1
50	40	150	8.27e-4	1.16e-3	1.44e-3	7.99e-1

Table 2.2: Parameter of the Voigt fits for the data shown in Fig. 2.6 and 2.7. The parameters are defined in Eq. 2.12.

enough. A more quantitative analysis will be given after the calculation of the intrinsic width, in Sec. 2.2.3.

2.2.2 Results for intrinsic width

As already stated, when a guided photonic mode in a periodic structure is folded back in the first Brillouin zone by the action of the periodicity, it can end up in the region of the $k\omega$ plane above the cladding light line, where the radiative modes exist. In such condition, the guided mode is not destroyed, but it is modified by the interaction with the continuum, both being broadened in energy and acquiring a finite lifetime.

The signature of such a mode can be seen in reflection/transmission experiments as the appearance of a Fano resonance, due to the interference between the direct response of the structure and the one mediated by the

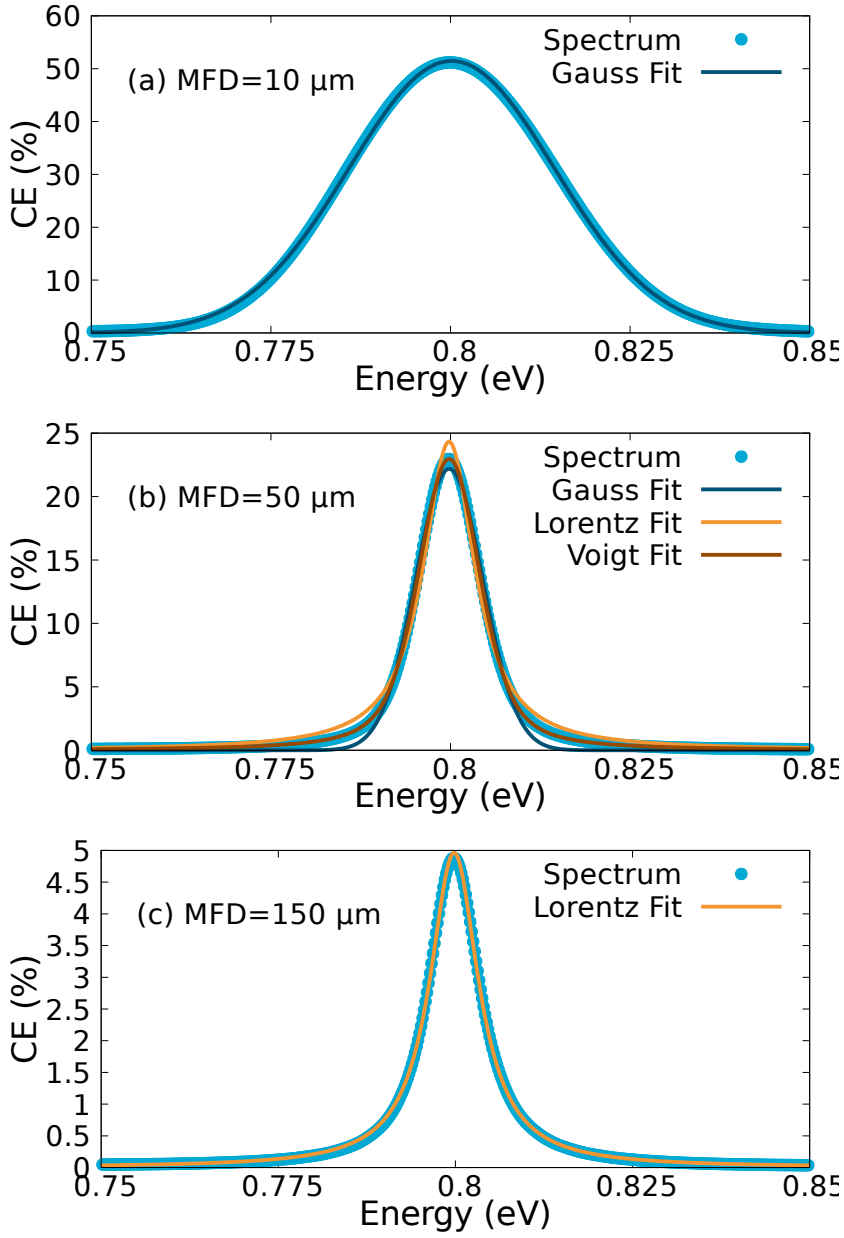

Figure 2.6: Coupling spectra for different MFD relative to the structure with DC=25% and Etch=80 nm.

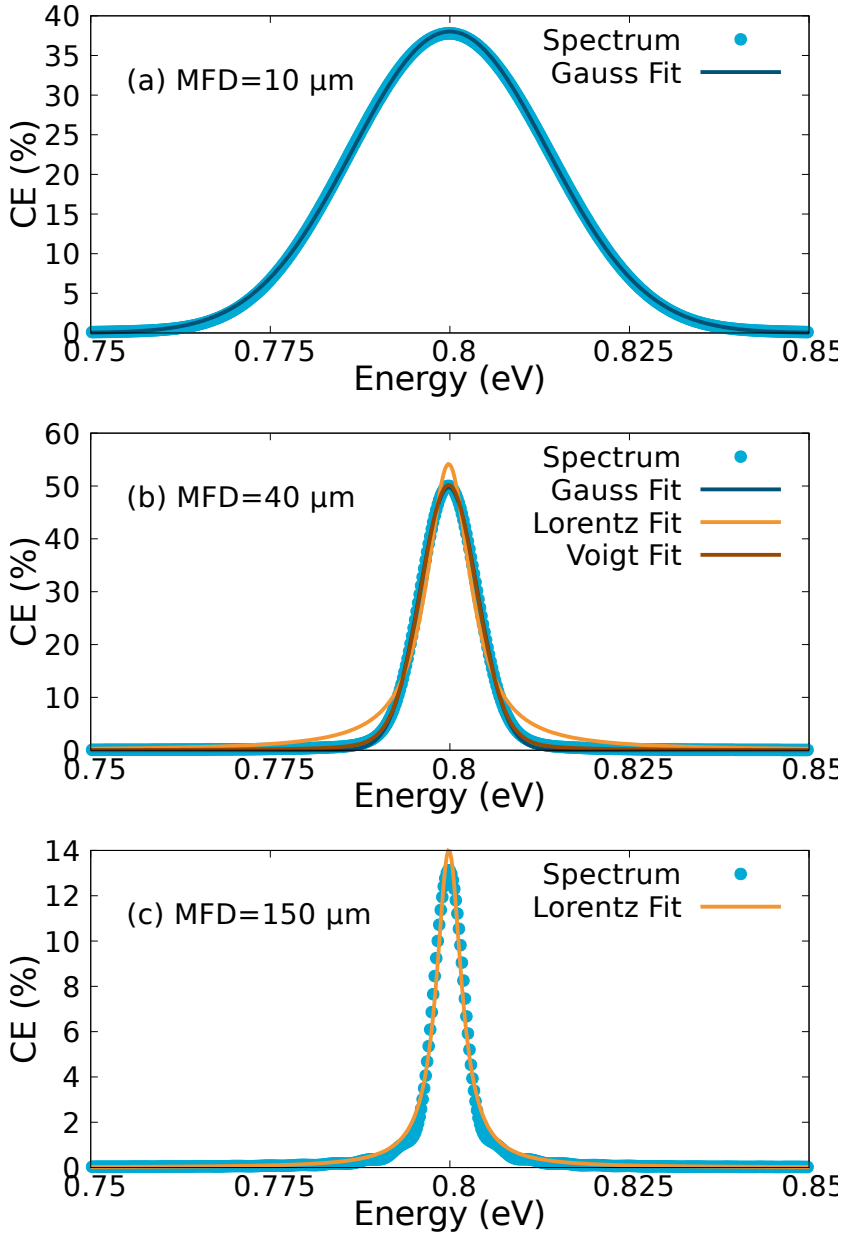

Figure 2.7: Coupling spectra for different MFD relative to the structure with DC=50% and Etch=40 nm.

resonating mode. By looking at the width of such a resonance it is possible to measure the width of the intrinsic photonic mode.

Thus, Rigorous Coupled Wave Analysis is employed for the calculation of such transmission and reflection spectra. The spectra are calculated under the condition of plane wave illumination, TE polarized (s-polarization) and incident at 10° from the upper cladding. The obtained transmission spectra are then fitted with the following Fano lineshape:

$$F(x, B, A, q, \gamma, x_0) = B + A\frac{\left[q + \frac{2(x-x0)}{\Gamma}\right]^2}{1 + \left[\frac{2(x-x_0)}{\Gamma}\right]^2} \tag{2.13}$$

where B represents the background contribution, A is a scale factor, q is a parameter giving the shape of the resonance, and x_0,Γ are the position and Half-Width-Half-Maximum of the resonance, respectively.

The Fano fit of Eq. 2.13 assumes a constant background as a function of energy. This is not the case here, since the Fano resonance adds on a background which has an energy dependence. To remove the effect of dispersion of the background two calculations are performed: one using the full structure and one in which the patterned part is substituted with an uniform medium with average dielectric constant. By subtracting the two spectra it is possible to extract the response assuming a flat background, and then the fit can be carried out.

This procedure is illustrated in Fig. 2.8, where the quality of the fit can be seen. It was carried out for the same structures analyzed in the previous section, and a comparison between the two is proposed in the next section.

2.2.3 Comparison

At this point, a comparison between the two methods is possible. The FDTD simulation is able to give both the Gaussian finite size contribution and the Lorentzian intrinsic one, which will be assumed to be the σ and Γ of the Voigt fit, respectively. The RCWA calculation is able to give the intrinsic contribution directly as the Γ of the Fano fit, and the Gaussian contribution can be obtained through Eq. 2.10 once the n_g is extracted.

The results of this procedure are shown in Fig. 2.9, where both contributions calculated with the two methods are plotted as a function of MFD. The Gaussian contribution is calculated assuming an effective index of 2.77, calculated by the Bragg condition of Eq. 2.2. This is not strictly exact, but since this region of energy is far away from the band edge, where the group

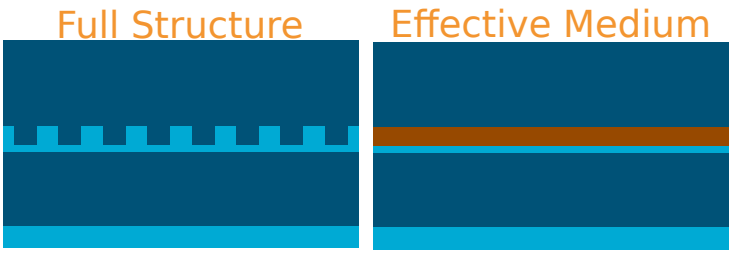

(a) Full structure versus effective medium.

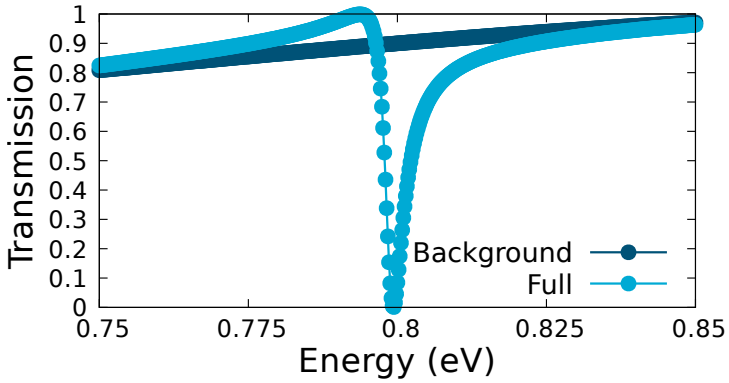

(b) Full spectrum of structure and background.

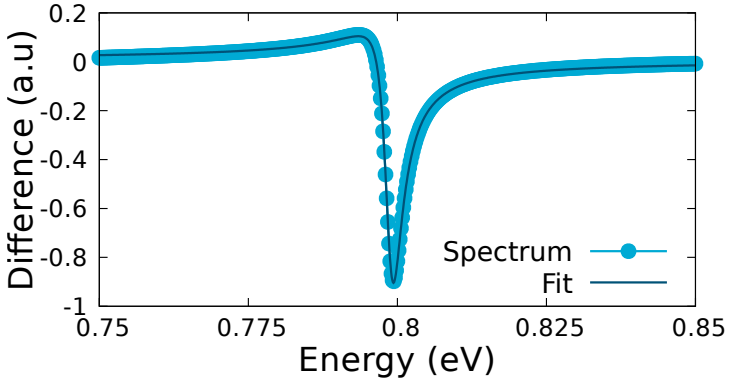

(c) Corrected spectrum and corresponding Fano fit.

Figure 2.8: Procedure for the fitting of Fano lineshape in the transmission spectrum. Parameters of structure are DC=50% and Etch=40 nm.

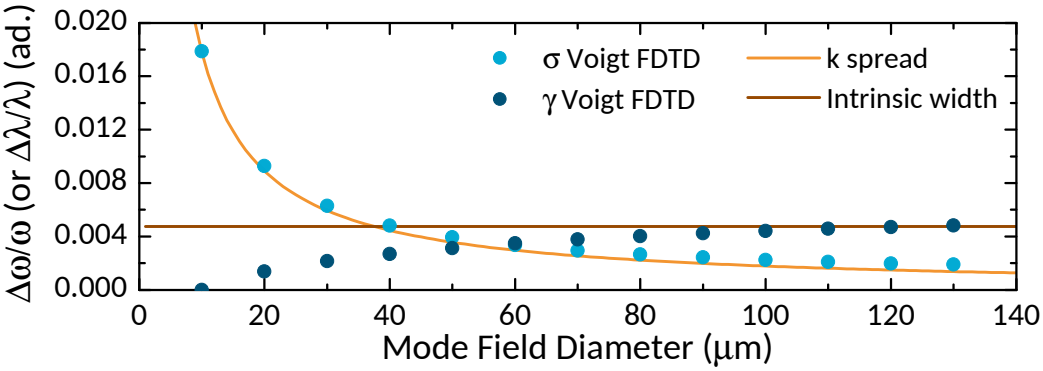

Figure 2.9: Comparison between the FDTD and RCWA calculations of the different contributions to the bandwidth for the structure defined by DC=25% and Etch=80 nm.

index greatly diverges from the phase index, this approach can be assumed to yield a valid approximation.

Regarding the intrinsic contribution, it can be seen that the Lorentzian contribution to the Voigt monotonically increases with the MFD, till saturation to the value of the width of the Fano lineshape provided by RCWA. This behavior can be explained with the fact that at least a few periods must be present in the slab before it is possible to speak of a quasi-guided photonic mode.

Concluding this section, it is possible to say that the interplay of finite size effect and photonic modes in the formation of grating-couplers bandwidth has been analyzed. Both effects have confirmed to be present in the bandwidth formation. Proof have been offered also by the shape of the coupling spectra, which evolve from a Gaussian for smaller MFDs (where the finite effect dominates) to a Lorentzian for bigger MFDs (where the intrinsic width dominated), passing through a Voigt lineshape for MFDs in the middle (where both contribution have similar magnitude). Both finite size effect and intrinsic width have been calculated with two different numerical methods, FDTD and RCWA, showing a good agreement.

Moreover, such analysis has exposed the fact that conventional grating-couplers operate in a regime in which the bandwidth is mainly dominated by the finite size effect, and that a good way of increasing such bandwidth cold be to move to smaller gratings and MFDs, possibly by employing lensed or high numerical-aperture fibers, which are commercially available.

2.3 Simultaneous optimization of couping efficiency and bandwidth

2.3.1 Overview

A great deal of research in the past years has been devoted to improving the performances of grating-couplers. The main concern has been the increase of coupling efficiency, since it is known as the main problem to overcome to successfully bring Silicon Photonics to the market. Losses in a grating-coupler could be seen as arising from mainly two mechanisms: non-optimal directionality and mode mismatch. Here both mechanisms will be discussed from the perspective of the grating-coupler working as out-coupler, and time-reversal symmetry will be invoked to extend the conclusion here drawn to the in-coupling case.

Directionality is the ability of a grating-coupler to scatter light out of the waveguide only in the desired direction, and it is defined as the ratio of the power emitted in the right direction over the total emitted power. A grating-coupler which is symmetric in the vertical direction (fully etched, with no silicon substrate and semi-infinite cladding) would have a directionality of 50%, since light would be equally split. Breaking the vertical symmetry, for example with partial etching or by introducing a silicon substrate (practically always present in real devices), allows for the redistribution of light and an increase of emission in the desired direction.

First studies on grating-couplers [66] focused on the vertical structure — waveguide thickness, etching depth and bottom oxide thickness — then available. In this way the directionality was more or less kept fixed. Shortly after, also thanks to more refined fabrication techniques, for example the possibility of adding poly-silicon [196], structures with modified vertical profiles begun to appear. By careful optimization of the vertical structure, a reduction of insertion loss up to 3-4 dB has been achieved for both 1D [69, 197] and 2D [67, 198].

One straightforward way to increase the directionality is to put a mirror in place of the substrate. This approach is able to bring the directionality almost to 100%, since any light scattered towards the substrate is reflected back, but usually at the cost of a substantial increase in fabrication complexity. Indeed, the mirror is usually placed under the grating either by substrate removal and metal deposition [199], a well-performing but hardly CMOS compatible solution, or by the realization of a Distributed Bragg Reflector (DBR) [200], which is CMOS compatible but still of difficult realization.

However, changing the vertical structure is not the only method to im-

(a) The emission profile of an uniform grating results in a poor overlap with an ideal fiber mode.

(b) By mean of apodization the emission profile can be changed, improving the overlap.

Figure 2.10: Mode overlap with and without apodization.

prove the directionality. Indeed, it can be changed also modifying the horizontal structure of the grating. For example, by changing the phase relation between adjacent scattering sites it is possible to create constructive interference for light scattering in one direction and destructive in the opposite. This kind of phase manipulation usually requires a sort of double grating, realized either with two juxtaposed and shifted gratings [201, 202] or by a double etch approach [49, 203]. This is a valid solution, since it decouples the problem of directionality from the vertical structure surrounding the grating, which is often fixed by foundries to values not always optimal for coupling purposes. The main disadvantage is that it requires multiple etching steps, which can be expensive to realize.

Besides directionality, the main other way to reduce insertion losses in grating-couplers is to reduce the mode mismatch between the optical fiber mode (usually assumed Gaussian) and the mode emitted by the grating. In standard uniform gratings the emission profile is a simple decaying exponential — see Fig. 2.10a — which yields poor mode overlap with the fiber mode. This geometrical mismatch limits the coupling efficiency to a maximum value of about 80%. To go beyond this value it is essential to abandon uniform gratings and to adapt the scattering strength along the grating to recover an output mode as similar as possible to a Gaussian [66] — see Fig. 2.10b. This technique is called *apodization*. Various procedures have been implemented over the years to design good apodized grating-couplers, going from semi-analytical approaches[71, 204, 205] to numerical optimization, for example with mutative [70, 206], genetic [196, 207, 208] or particles swarm algorithms [208, 209].

More sophisticated apodization techniques resort to more complex structures to improve the design freedom and reach better performance. For example, by using particular etching procedures, it is possible to vary the etching depth of each groove (thinner grooves are etched less). This allows an even larger decrease of scattering strength in the first part of the grating, leading to a better mode matching [210]. Another solution is to employ sub-

wavelength structures, allowing for the tuning of the effective index of the material in addition to the geometrical properties [209, 211, 212].

Such approaches can reach very high performances, but usually at the expense of a long and complex optimization procedure. Moreover, optimal mode matching usually requires shrinking the first few teeth of the grating to very small values, down to few tens of nanometers in width. Current fabrication techniques, based on lithography, have limited resolution and have a minimum size in the features that can be handled. In order of increasing cost, it goes from around 200-300 nm of UV lithography, to 100 nm of standard deep UV ($\lambda = 193$ nm), to around 40-50 nm of e-beam lithography, which is however a serial process and cannot reach the high volumes of UV. Although these constraints are nowadays being relaxed, for example with the development of deep-UV immersion lithography [213], they have to taken into account at the design stage, thus resulting in a forcefully diminished mode matching with respect to the ideal case.

In almost all the cases reported above, the main focus of the research was to reduce the insertion loss as much as possible, while little attention had been given to the bandwidth, which always remained in the common range around 30-40 nm (measured at -1dB from the maximum coupling).

Some studies on how to increment the bandwidth of grating-couplers have been performed in the past years, based on a few different methods. An efficient one is to lower the refractive index of the waveguide, both using materials other than silicon, such a silicon nitride [214, 215], or employing a sub-wavelength patterning [216]. Possible other solutions are the use of fibers with a smaller MFD [201, 217] or the zero-order approach [48]. All these approaches can indeed deliver an almost threefold increase over typical 1-dB bandwidths, ranging from 80-90 nm for conventional (first-order) gratings up to almost 130 nm for the zero-order one, while retaining an insertion loss lower than a few dB. However, a simultaneous CE-bandwidth apodization procedure for conventional grating couplers has never, to my knowledge, been reported.

2.3.2 Optimization procedure

In this section, the procedure of apodization is extended, optimizing the width and position of each groove of the grating using a multi-objective algorithm, in such a way that a simultaneous optimization of both coupling efficiency and bandwidth is carried out. Multi-Objective optimization takes a different approach to the problem than standard Single-Objective optimization. In Multi-Objective optimization, in fact, two ore more performance measures, each expressed by a different fitness function, have to be taken

into account. In these conditions, it is almost never the case of all the functions to be simultaneously maximized by the same structure. Indeed, in the most common situation, such as the CE-bandwidth problem here analyzed, the increasing of a fitness function causes the decreasing of at least one other. Consequently, the same of concepts of "best" and "better" cannot be applied anymore, and new definitions are needed.

Thus, the notion of "better" is replaced by the notion of "dominance": a solution $\mathbf{x}$ is said to dominate the solution $\mathbf{y}$ when:

$$f_i(\mathbf{x}) \geq f_i(\mathbf{y}) \, \forall i \text{ and } \exists j : f_j(\mathbf{x}) > f_j(\mathbf{y}), \tag{2.14}$$

namely a dominating solution is strictly better on at least one fitness function while being no worse in all the others. With such definition, the "best" solution can be defined as one which is not dominated by any other solution. It is clear that with this definition it is almost impossible to indicate a single solution as the global best. Instead, an ensemble of non dominated solutions should be identified for each problem, which together form the so-called Pareto front. Moving along this front gives solutions with different trade-offs between the different fitness functions. The aim of a Multi-Objective optimization is thus to find such front, usually by employing an iterative procedure which approximates the Pareto front better and better after each iteration, until final convergence occurs.

All optimizations in this chapter, both single- and multi-objective, are carried on with variations of the Particle Swarm Optimization algorithm [218], developed for heuristic optimization by taking inspiration from the behavior of swarms of bees looking for the higher flower-density point in a field — see Appendix C for a complete description of the method.

During this work, the multi-objective apodization procedure will be applied to grating-couplers employing as excitation Gaussian Modes with different MFD, achievable in practice with lensed or high numerical-aperture optical fibers. The chosen value, beyond the standard 10.4 µm, are 8.0,6.0, and 4.0 µm. The goal is to take advantage of the finite size contribution to the bandwidth to achieve better performances. As in the previous sections, each grating-coupler is simulated using the FDTD method available through the commercial software Lumerical FDTD Solutions. Moreover, the same scripting language available from the software is employed for the implementation of the PSO algorithms, both single- and multi-objective.

In order to apply the multi-objective apodization procedure, it is important to choose a good starting point in terms of general parameters of the grating. To this end, a two step optimization procedure is employed to ensure a starting point for the Multi-Objective optimization with a good coupling

efficiency. In the first step a single objective PSO algorithm is employed to optimize the uniform grating for the maximum coupling efficiency. The parameters available to the algorithm at this point are only four: the etching depth Etch, the duty cycle DC, the bottom oxide thickness Tbox, and the fiber offset FIB (the distance of the center of the fiber from the first tooth of the grating). The period of the grating is still tuned to give the maximum coupling efficiency at λ =1.55 µm.

Then, the knowledge of the best uniform grating for each MFD is employed as starting point for the second single-objective PSO, which is designed to optimize the coupling efficiency of a linearly chirped grating. Applying a linear chirp to a grating coupler amounts, in general, to varying the duty cycle along the grating in a linear way from a starting DC_0 to a maximum DC_{max} in a distance L_{chirp}, namely:

$$DC(x) = \begin{cases} DC_0 + x(DC_{max} - DC_0)/L_{chirp} & \text{for } x < L_{chirp} \\ DC_{max} & \text{for } x > L_{chirp} \end{cases} \tag{2.15}$$

which can be thought as a simple apodization procedure. The parameters available to the optimization are thus DC_0, DC_{max}, L_{chirp}, Etch, Tbox, and FIB. At this point the period is still tuned and constant along the grating.

After that, the Multi-Objective PSO algorithm can be applied. The free parameters of the optimization at this point are the widths and the positions of each groove in the grating, which are varied around the widths and positions obtained in the previous step. While in the preliminary optimizations the gratings are always tuned to the right operational wavelength , during the Multi-Objective PSO this is no more enforced. Instead, it is left to the definition of the search space of the optimization to generate structures which keep the targeted wavelength (1.55 µm) inside the 1dB bandwidth. This constraint is then verified a posteriori and found to be satisfied.

In practice, to better ensure convergence of the Multi-Objective optimization in the high CE part of the Pareto front, a prior dedicated Single-Objective optimization with the same free parameters of the Multi-Objective one is run and the obtained knowledge is inserted as a starting point for the Multi-Objective optimization. This procedure is carried out only for the three smaller values of MFD, since the apodized structure with best coupling efficiency for the standard 10.4 µm is assumed known from literature [70].

All Single-Objective PSOs are run with 10 agents and 150 iterations, which is usually more than enough to get convergence. The Multi-Objective PSO, due to its greater complexity, since it requires the much slower convergence of a set of structures, is instead run with 20 agents and 1000 iter-

MFD (µm)	CE (%)	BW (nm)	DC_0 (%)	DC_{max} (%)	L_{chirp} (µm)	Etch (nm)	Tbox (µm)	FIB (µm)	Per. (av.) (nm)
4	56.7	89	10	35	2.13	150	2.10	2.48	684
6	60.1	67	10	40	4.97	120	2.02	3.68	662
8	61.6	54	10	40	4.98	100	2.00	4.19	644
10.4	—	—	—	—	—	100	2.00	7.50	634

Table 2.3: Final parameters after the double stage optimization of the linearly chirped gratings. The values of Etch, Tbox and FIB are also the ones used for the Multi-Objective optimization. A few values in the last row are missing since no chirped structure is optimized and the reported values are taken directly from [70].

ations, thus exploring a total of 20K structures (with the exception of the MFD=10.4 µm, which is instead run for 1500 iterations).

2.3.3 Main results and discussion

The results of the preliminary optimizations (research of the linearly chirped grating with maximum CE) are reported in table 2.3. It is evident that for the optimized linearly chirped structures the CE increases and the bandwidth decreases on increasing the MFD. This is expected: increasing the MFD also increases the number of grooves in the grating, thus making the adjustment of scattering-strength along the grating more gradual and less coarse, allowing for a more efficient mode matching, while at the same time reducing the finite-size contribution to the bandwidth. Moreover, it is worth noting that, while the thickness of the bottom oxide remains almost constant (the condition for constructive interference in the upward direction is more or less the same independently on MFD), the etching depth has to increase on decreasing MFD, since the scattering-strength has to be raised in the shorter gratings.

This intermediate step gives the general parameters (Etch,Tbox, and FIB) for the Multi-Objective optimization, as well as defining the parameter space for the algorithm. After the MO-PSO is run to the end, the resulting Pareto fronts are the ones reported in Fig. 2.11. As already stated, those fronts represent the ultimate trade-off between coupling efficiency and bandwidth, at least relative to the parameter space here explored. It is thus evident from the data that such trade-off does exist, and that different forms of the trade-off can be reached through multi-objective apodization.

As a function of decreasing MFD, a general increase in bandwidth and decrease in Coupling Efficiency can be seen. This is essentially the same behavior observed for the linearly chirped gratings, and is expected for the

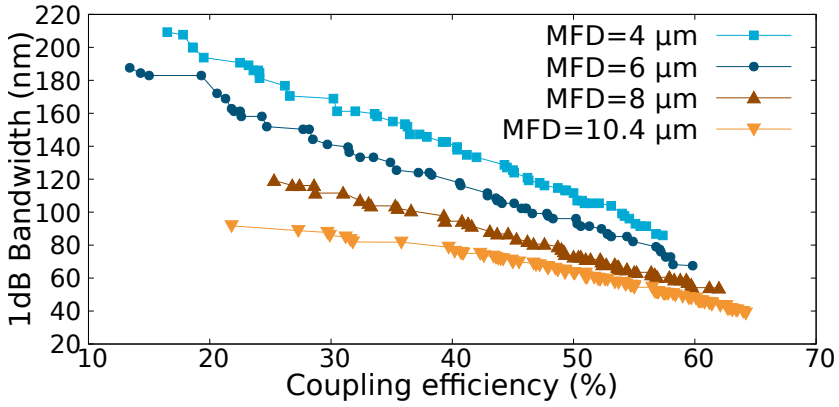

Figure 2.11: Representation of the obtained Pareto fronts for each value of MDF.

same reason. From these data, it is apparent that the target bandwidth of 100 nm cannot be reached with standard (MFD=10.4 µm) optical fibers. It can however be reached employing smaller fibers (both lensed or high numerical aperture ones), and Coupling Efficiencies up to 36%, 46%, and 53% can be obtained for MFD equal to 8,6, and 4 µm, respectively. This shows that, by combination of smaller-than-normal MFDs and dedicated optimization 3dB insertion loss can be reached together with 100 nm bandwidth. It is worth noting that the overall performances of such grating-couplers are somehow inferior to other solutions presented in literature, which are able to demonstrate $\approx$ 100 nm 1dB bandwidth with sub-decibel insertion losses. However, it is fair to say that such increase in performance is obtained at the price of more complex structures, requiring for example a double grating [201, 217], sub-wavelength pattering [216], or the addition of a prims placed at a very precise angle above the grating [48].

For the complete results of the optimization see Supplementary Materials of [219], where all the geometrical parameters (including grooves' widths and positions) of each solution on the Pareto fronts are reported.

2.3.4 Tolerance analysis

To give robustness to this analysis, which involve quite complicated structures, in the absence of experimental realizations, a campaign of numerical simulations devoted to analyzing the tolerance to variations has been performed. Such tolerance analysis is divided in two parts: in the first part attention is placed on the effect of variation of etching depth, while the second one is dedicated to random variations in the widths and positions of the

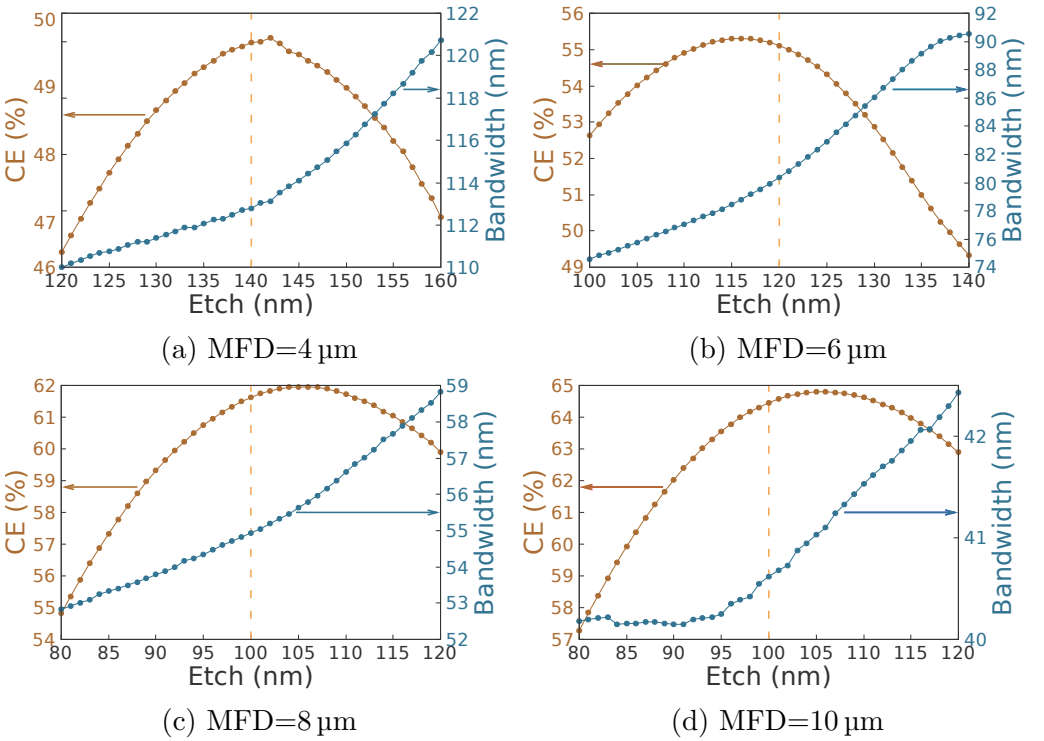

(a) MFD=4 µm (b) MFD=6 µm

(c) MFD=8 µm (d) MFD=10 µm

Figure 2.12: Etch depth tolerance analysis for 4 structures from the four different Pareto fronts. The vertical line represent the design etch depth.

grooves.

Etching depth

Finely controlling the etching depth of a typical fabrication run can be quite challenging. In fact, every time the etching depth is changed, an almost total re-optimization of the etching procedure is required. Thus, variation of the etching depth from the nominal design, however usually contained in the ±10 nm, can happen. Since this type of effect tends to affect all the grooves at the same extent, the tolerance analysis regarding the etching depth is performed with a sweep on the Etch parameter (with 1 nm steps) for some selected structures on the Pareto front. During these simulation the FDTD mesh in the region of the grating was chosen with a vertical maximum step of 1 nm, to be able to appreciate even the smallest changes.

It is evident that the tolerance to etching depth variation is quite good. In fact, all investigated structures show a window of 10-15 nm where the coupling efficiency is fairly constant, although not always centered at the design etching. This is mainly because the etching depth is chosen as the

one of the linearly chirped grating with maximum CE, which may not always be the optimal one for every structure on the front. Moreover, during the preliminary Single-Objective optimizations the minimal variation permitted to the etching depth is 10 nm, so the more subtle features here presented could be missed. However, given such premises, it is possible to conclude that these designs are quite robust with respect to etching depth variations.

Disorder

The other source of deviation from the design in fabrication phase could come from the mask, which usually causes errors in the definition and placing of the grooves. While the errors in the positions are usually uncorrelated, the errors in the widths can be, since they are normally the results of under- or over-etching, which tends to uniformly decrease or increase the groove's width, respectively. Taking this into account, a sort of Monte Carlo analysis on the structures on the Pareto fronts is performed. It starts from a structure on the fronts and, by applying random variations to the width and position of each groove (extracted from a ± 10 nm uniform distribution), generates a new grating which is then analyzed. The procedure is repeated, generating 20 different structures for each grating on the Pareto fronts. The coupling efficiency and bandwidth of each obtained structure is reported in Fig. 2.13 for all four values of MFD. It can be seen that the spreading of performances around the Pareto fronts is quite limited, suggesting a good tolerance to this kind of disorder.

It can also be noticed that this Monte Carlo procedure also generated very few structures above the Pareto fronts. The number of the points above can be interpreted as a measure of the state of convergence of the algorithm. In fact, this is the reason why the MO-PSO for the 10.4 µm MFD was performed with 1500 iterations: the tolerance analysis on the 1000 iterations Pareto front showed poorer convergence.

Although complete convergence cannot be seen in all the Pareto fronts, the deviation above the front is definitely inside the variation expected from fabrication errors. For this reason, theoretical improvements on this scale would be difficult to translate in actual improvements of the real structure, and the convergence seems thus to be sufficient for the scope of this work.

2.4 Conclusions

In this chapter, a theoretical study of the problem of bandwidth in grating-couplers has been presented, focusing on standard SOI platform with a silicon

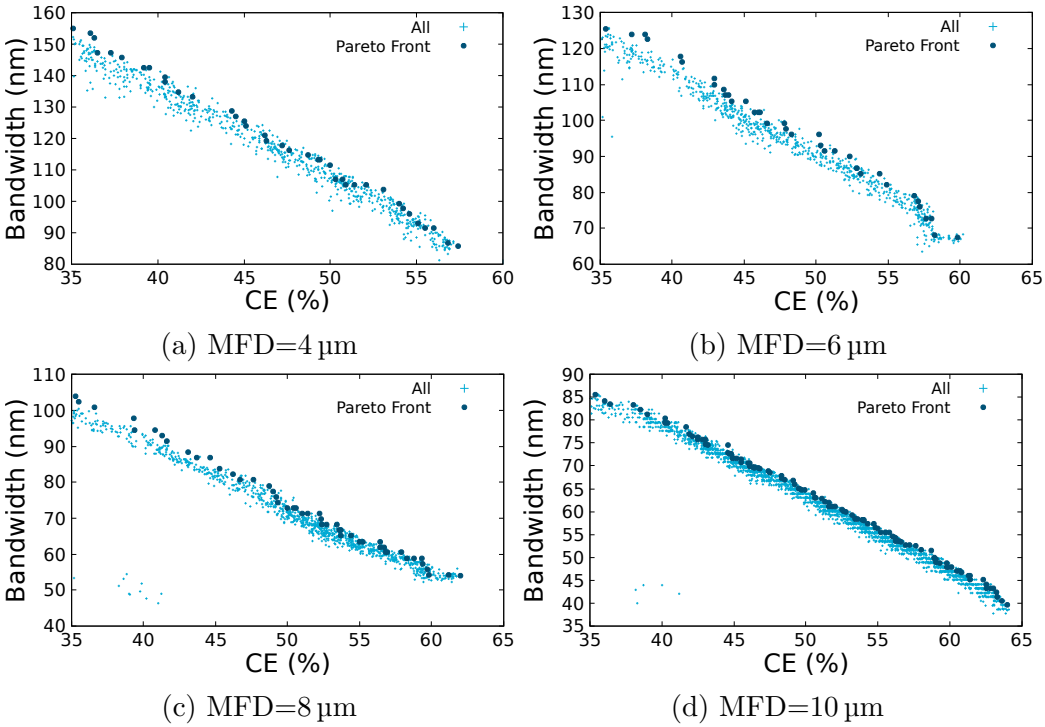

(a) MFD=4 µm (b) MFD=6 µm

(c) MFD=8 µm (d) MFD=10 µm

Figure 2.13: Disorder tolerance analysis for the four different Pareto fronts.

thickness of 220 nm operating at standard telecom wavelength of 1.55 µm. Through a campaign of numerical simulations, both FDTD and RWCA, the mechanisms beyond the bandwidth formation have been investigated. In particular, two processes behind the bandwidth formation have been found. The first one is a finite size contribution, of Gaussian nature, decreasing in strength as the extension of the exciting mode increase. The second one is coming from the intrinsic width of the photonic mode inside the grating, it has a Lorentzian nature and does not depend on the excitation. By varying the diameter of the Gaussian Mode used as a source it is possible to modify the relative strengths of these two components. In the typical operational condition of grating-couplers, with an MFD around 10 µm, the finite-size Gaussian contribution usually dominates, suggesting that to increase the bandwidth it would suffice to move to smaller MFD.

In addition, a multi-objective numerical optimization of grating-couplers with various values of MFD has been performed, with the goal of simultaneously optimizing Coupling Efficiency and bandwidth. Through this procedure, widths and positions of each groove in the grating can be optimized to explore the better trade-off between coupling efficiency and bandwidth. It is shown that combining suitable optimization with smaller-than-standard

MFD, great increase in bandwidth can be achieved. In detail, the target 100 nm can be achieved with 36%, 46%, and 53% CE using a MFD equal to 8,6, and 4 µm, respectively. Further improvement of performance could be achieved by the use of a thicker silicon layer (e.q. 300 nm).

Chapter 3

Grating-Couplers: PIC-to-PIC

3.1 Introduction

Although born in the context of fiber-to-chip light coupling — see Fig. 3.1a, more recently grating-couplers have been proposed as valid candidates also for other applications. In particular, applications such as inter-layer or inter-chip coupling have been explored, since they can greatly benefit from the efficient out of plane coupling grating-couplers are able to provide.

A notable feature, but also a drawback, of current photonic and electronic technology is that every circuit is basically a 2D device. Both photonic and electronic circuits are indeed patterned on two dimensional slabs of materials, thus limiting the placement freedom and the density of components. The straightforward solution, namely going to a full 3D technology, is not of easy realization. A solution compatible with current technology could be the realization of multiple 2D layers inside the same chip, but it would require an efficient way to couple light between layers. Since the distance between the layers has to be large enough to avoid cross-talk, direct adiabatic coupling is practically out of question, and a system composed of two grating-couplers (one in each layer) seems a valid solution [220, 221].

The same grating-to-grating approach can be useful even for light coupling between two different chips stacked on top of each other [222], for example using flip-chip technology [223] — see Fig. 3.1b. This approach could provide a cost-efficient and compact way to connect together one or more different photonic chips.

Designing grating-couplers for this grating-to-grating application is not without challenge. In fact, if two uniform grating-couplers were employed, the modal mismatch would be even worse than in the fiber-to-grating case. Apodization — see Fig. 3.2 — is thus a crucial step of the design [224].

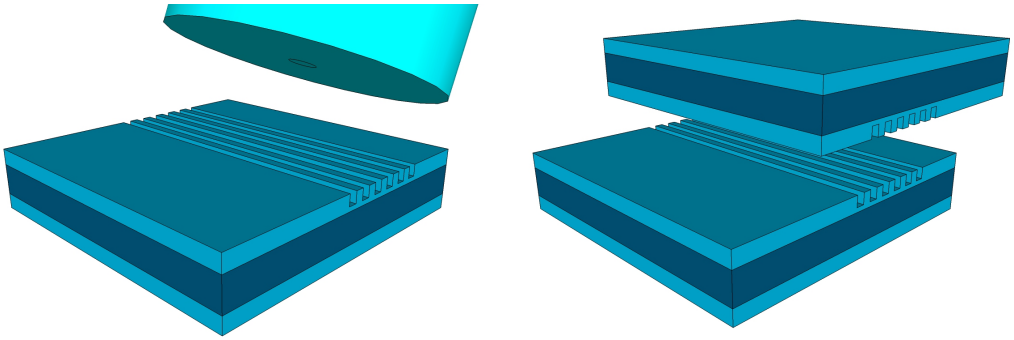

(a) Fiber-to-chip coupling. (b) Chip-to-chip coupling.

Figure 3.1: Two possible applications of grating-couplers.

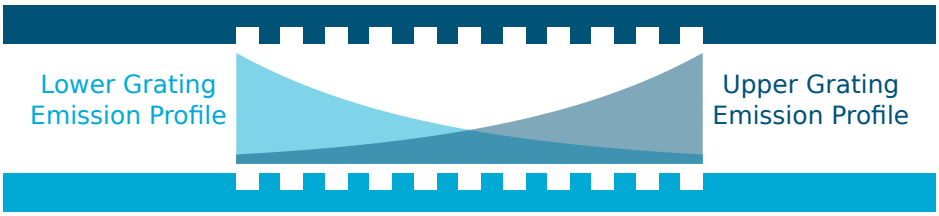

(a) Non apodized.

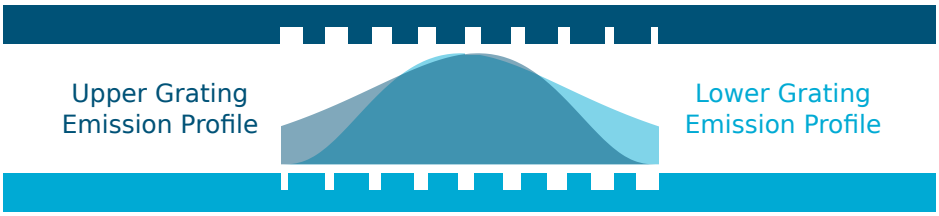

(b) Apodized.

Figure 3.2: Role of the apodization on the modal mismatch in the case of grating-to-grating coupling.

The great majority of the studies on grating-to-grating coupling have been carried on considering a couple of identical gratings, or a least within the same materials and vertical structures. This greatly simplify the design process, since after the mode matching procedure has been performed, the angular dispersion of the emission as a function of wavelength is automatically taken into account. In fact, if the Bragg condition:

$$kn_{eff} = k_{\parallel}^{inc} + \frac{2\pi}{\Lambda} \tag{3.1}$$

is satisfied for one grating, it is automatically satisfied by the other. As a consequence, the typical bandwidth of a grating-to-grating connection is fairly wide, featuring 1dB bandwidth up to 100 nm or more.

A few attempts have been made to design inter-layer coupling when different materials are involved, for example coupling between Si and SiN layers [225], where the problem of the tuning between the two gratings is solved though a numerical optimization based on a Genetic-Algorithm, which simultaneously optimizes the parameters of both gratings. Due to the huge parameter space involved, such optimizations are often quite expensive, and the physics involved in the process could be missed.

In this chapter, the same grating-to-grating approach is used to solve the problem of light coupling between two chips of different platforms, in particular the conventional SOI and an InP based platform. Realizing efficient and cost-effective light coupling between SOI and a III-V semiconductor platform could open interesting possibilities, allowing for the integration of typical III-V features, such as gain for the realization of lasers and amplifiers, in silicon. Such connection is usually made by different approaches, such as wafer-bonding or transfer printing, which suffer from serious drawbacks, such as considerable material wastage (wafer-bonding) or sub-µm alignment (transfer printing). A successful grating-to-grating coupling scheme could overcome these problems by switching to the easier technology of flip-chip [226].

The gratings are considered to work at the standard telecom wavelength λ =1.55 µm. The following of the chapter will contain a description of the platforms, the gratings design, and discussion of the results.

3.2 Grating-couplers design

3.2.1 The platforms

The platforms available for this chapter, namely standard SOI and an InP-based platform, are the ones shown in Fig. 3.3.

Material	Refractive Index
Si	3.44
SiO_2	1.44
InP	3.17
Fe – InP Q(1.3)	3.36
Fe – InP Q(1.06)	3.26

Table 3.1: Refractive indexes of the materials involved.

Regarding the InP platform, the one available at Fraunhofer Heinrich-Hertz-Institute (HHI) [227] is taken as a model — see Fig 3.3b. Light is guided inside a 250 nm layer composed of a Fe doped InP, embedded in pure InP. A 100 nm thick layer of doped InP with different Fe concentration is embedded 1180 nm under the waveguide, and the whole structure rests on an InP substrate. The InP layer composing the top cladding is 1.6 µm thick. The etching depth is variable, as well as the etching direction, which can be chosen to have an arbitrary angle β with respect to the vertical direction. The layers composition and thickness are fixed by the foundry for various reasons, and will not be optimized during this work.

On the contrary, due to the greater number of standards and of foundries, more freedom is assumed for the SOI platform. Basically, the only constraint is the 220 nm thick waveguide layer. All the other vertical parameters, such as top and bottom oxide thickness, are taken as free. Moreover, two different configurations will the explored: a conventional one with the grating defined by etching, and one in which the grating is defined by silicon teeth added on top of the waveguide. Since the teeth of the second solution could be realized with deposition and subsequent etching of poly-silicon, this second solution could provide a viable route to the realization of grating-couplers with tailored scattering-strength, without requiring the re-adjustment of the etching process each time.

Regarding the horizontal geometry, almost complete freedom is assumed. The gratings are apodized, and the parameters of the optimization are set to keep the minimum feature size around 50 nm.

3.2.2 The scattering strength problem

Since this InP platform has never, to my knowledge, been optimized for grating-coupling, a more detailed study is needed before entering the core of the optimization. In particular, the relatively low index contrast available greatly limits the maximum achievable scattering-strength. To prove that, a

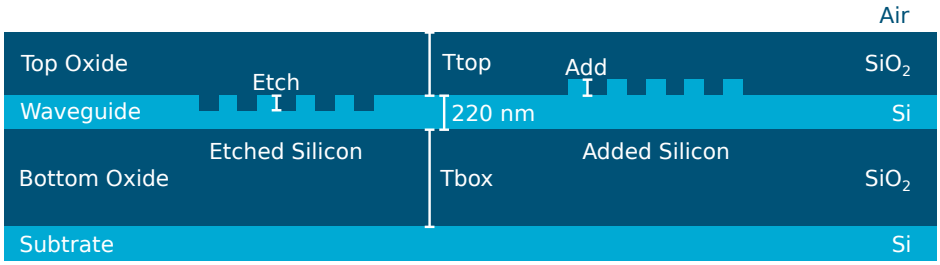

(a) Silicon platform.

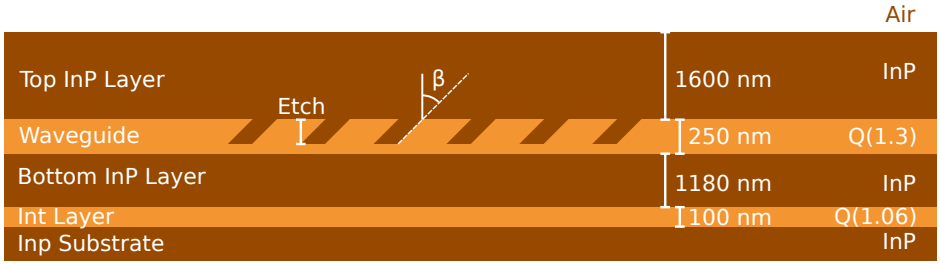

(b) Indium phosphide platform.

Figure 3.3: Graphical representation of the structure of both platform here involved. Whenever a number is indicated, that parameter is kept fixed throughout the whole chapter. Refractive indexes are reported in Tab. 3.1.

quick sweep over the parameters of the uniform grating is performed. A good combination of parameters giving scattering-strength close to maximum is: full-etching, filling-fraction F (ratio between etched part and period) of 0.45, blaze angle $\beta = 45°$ and a period of 516 nm.

The scattering performance of this configuration is then carefully studied. An analysis of how the light entering the grating from the waveguide is distributed across the 4 relevant channels — upward, downward, backward, and forward emission — as a function of grating's length is reported in Fig. 3.4. The low scattering-strength is clearly evident, as the forward propagation is attenuated with a rate of 0.06 dB/µm, which is at least one order of magnitude lower than typical scattering-strength in SOI. The upward and downward emission obviously increase as the length is incremented, showing a directionality (ratio between the upward emission over the total out-of-plane emission) of about 70%. Given such values, to obtain a useful upward scattering the grating has to be made quite long, up to 150 µm, where only 10% of the light remain in the forward direction.

A favorable feature is that the backward emission is very low, below 30 dB. This is less than the rule-of-thumb value of 25 dB usually assumed as safety limit when operating near back-reflection sensitive devices, such as

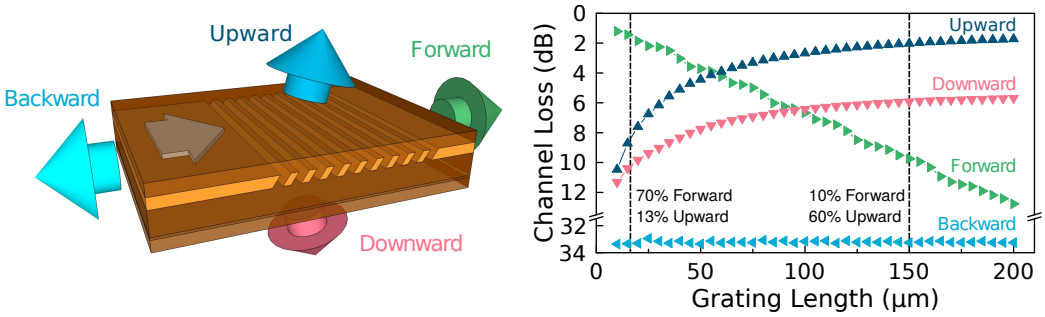

(a) Definition of channels.

(b) Distribution between channels.

Figure 3.4: Distribution of light between the four available output channels.

lasers or amplifiers [228].

This analysis suggests that the best way to obtain relevant performances from a InP grating is to resort to longer-than-normal grating-couplers. This is not a problem here, since the dimension of the radiative mode is not fixed from some external constraint (such as the dimension of an optical fiber), but rather decided by the other grating. The downside of this approach is that the length and scattering-strength of the InP grating would have to be matched by the Si one, requiring both gratings to be optimized for joint operation.

3.2.3 Optimization procedure and results

When dealing with the optimization of two coupled systems, two possibilities arise: optimize the two sub-systems together as a joint one or optimize the two sub-systems separately using some constraints which could guarantee a good behavior when the sub-systems are joined. In this case, a joint optimization would greatly add to the complexity of separated single grating-coupler optimizations, since the problem of tuning the periods of both gratings to emit/adsorb the same frequency at the same angle cannot be easy handled by a numerical optimization. Moreover, such a procedure tends to overlook the details of the physics involved.

Thus, in this chapter the latter approach is adopted. For each length L, the gratings are optimized as in-couplers using as excitation a Gaussian mode with a MFD equal to L. The gratings are tuned by forcing the emission at 14.4° (in air) to be the central operational wavelength of 1.55 µm, with a tolerance of 1 nm. This angle is chosen because it is a common one in fiber-to-chip setups, although in this case probably a wide range of angles (as long as it is different from 0) could be chosen, with minimal effect on the

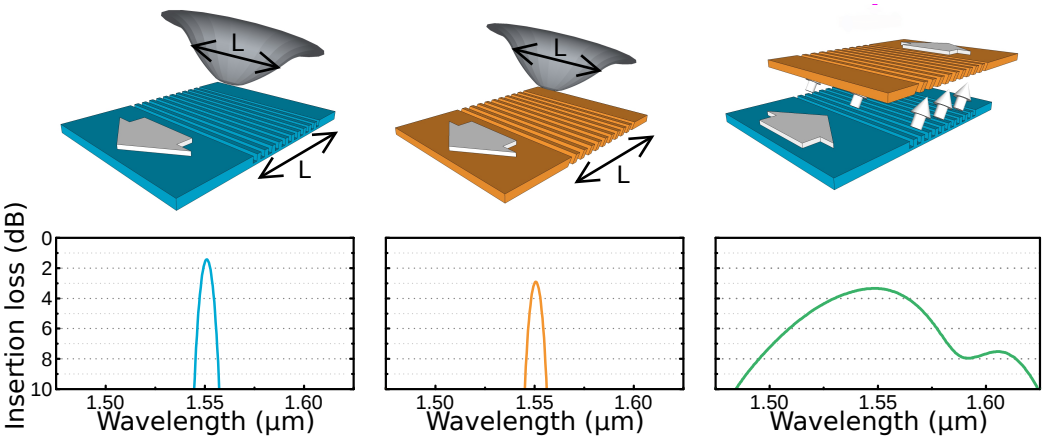

Figure 3.5: Graphical representation of the double optimization approach and example of coupling spectra — Etched Si and InP, L=100 µm.

performance. The hope is that optimizing the gratings on the same emission profile, at the same emission angle and the same wavelength, would ensure a good coupling when the gratings are coupled together — see Fig. 3.5.

The main advantage of this approach lies in the fact that two simple optimizations are carried out, instead of a single complex one. Moreover, this split approach allows for the realization of building blocks which can then be replaced as needed, for example using the same InP grating for both SOI configurations.

Each grating is optimized by employing the design rule developed by Marchetti *et al.* [71], in combination with a single-objective Particle Swarm Optimization. In detail, the design rule allows for a representation of the apodized grating dependent only on a small set of parameters, which are numerically optimized using the PSO algorithm.

The design rule [71], along with a few modifications, will be here recalled. It starts from a simple linearly chirped grating, namely a grating in which the filling fraction is adjusted as a function of the position x along the grating as:

$$F(x) = \min(F_0 + Rx, F_{max}) \tag{3.2}$$

where F_0 and R are the starting filling fraction and the apodization coefficient, respectively. The quantity F_{max}, namely the maximum filling fraction, is here inserted for reasons of numerical stability because of the longer-than-normal gratings. It indeed forbids the filling fraction to grow indefinitely, which could cause some problems during the PSO algorithm. Moreover, the grating is not uniform, but rather adjusted along x by simply inverting the

Bragg condition (Eq. 3.1):

$$\Lambda(x) = \alpha \frac{\lambda}{n_{eff}(x) - \sin(\theta)} \tag{3.3}$$

where $\Lambda(x)$ is the variable period of the grating and λ, θ are the wavelength and angle of incidence (in air) of the incoming radiation. The effective index n_{eff} is a function of x through its dependence on the filling-fraction:

$$n_{eff}(F) = F n_e + (1 - F) n_w \tag{3.4}$$

where n_w and n_e are the effective phase indexes of a uniform slab waveguide with the thickness of the waveguide and of the etched or added part, respectively. The factor α inserted in Eq. 3.3, absent in the original formulation, is there to force the grating to be tuned to the desired wavelength (λ=1.55 µm at 14.4°), compensating for the fact that Eq. 3.4 for calculating the effective index is only an, however good, approximation. The factor α is chosen by an iterative procedure to keep the grating emission tuned at 1.55 µm within a certain tolerance, which is assumed to be 5 nm during the PSO and 1 nm on the final structure.

Employing such rule greatly simplifies the design flow. Each grating can now be modeled with a small number of parameters, which can be easily handled by a numerical optimization. For the InP grating-coupler the parameters are: the starting filling-factor F_0, the apodization coefficient R, the maximum filling-factor F_{max} and the blaze angle β. Although in principle the technology could allow for variable etching, full-etch is chosen to maximize the scattering-strength and simplify the optimization. As stated before, the parameters regarding the layer thicknesses are kept fixed.

Regarding the Si grating, more parameters are needed. In addition to F_0, R, and F_{max}, with the same meaning as the InP case, there are the vertical parameters: the top and bottom oxide thicknesses Tbox and Ttop, and, depending on the configuration, the etching depth Etch or the thickness of the added poly-silicon Add.

The optimization procedure is carried out for different values of length, namely 15,25,50,100, and 150 µm. Greater lengths are not explored since the expected improvements are not important enough to justify the additional computational effort, which, since the FDTD method is used, scales linearly with the length. Each PSO optimization is run with 10 agents and 150 iteration on a nine-core desktop workstation, with computational time going from a few hours to about a day for the optimization of a single structure, depending on the length.

L (µm)	F_0	F_{max}	R (m^{-1})	β (deg.)	$100(\alpha - 1)$
15	0.38	1.0	5387	49	-0.741
25	0.37	0.55	5020	51	-0.756
50	0.39	0.44	4753	50	-0.674
100	0.36	0.42	2449	54	-0.725
150	0.36	0.40	1375	57	-0.775

Table 3.2: Optimized parameters for the InP gratings.

L (µm)	Etch (nm)	F_0	F_{max}	R (m^{-1})	Tbox (µm)	Ttop (µm)	$100(\alpha - 1)$
15	110	0.1	1.0	27500	2.00	0.72	0.00[71]
25	85	0.1	0.59	9925	1.97	0.21	0.417
50	53	0.1	0.47	6552	1.95	0.24	0.052
100	35	0.1	0.53	4276	1.93	0.25	-0.035
150	30	0.1	0.55	2198	1.93	0.25	-0.024

Table 3.3: Optimized parameters for the Si etched gratings.

L (µm)	Add (nm)	F_0	F_{max}	R (m^{-1})	Tbox (µm)	Ttop (µm)	$100(\alpha - 1)$
25	100	0.12	0.61	9893	1.84	0.36	0.120
50	70	0.10	0.62	5861	1.86	0.32	0.017
100	37	0.10	0.58	4561	1.88	0.29	-0.124
150	30	0.10	0.53	2917	1.89	0.29	-0.064

Table 3.4: Optimized parameters for the Si added gratings.

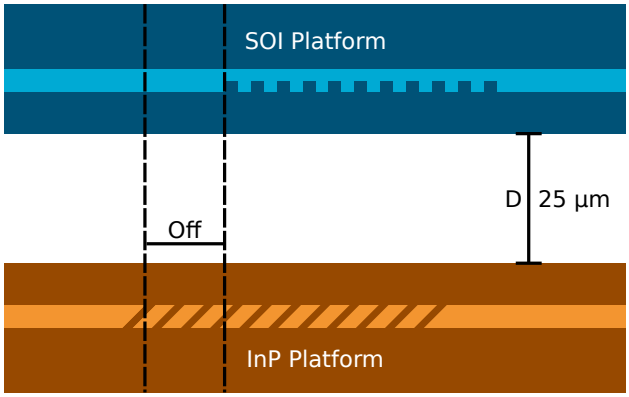

Figure 3.6: Structure of the grating-to-grating simulation.

After the optimization is complete, two of the resulting gratings are placed one above each other — see Fig. 3.6 — at a distance D of 25 µm, compatible with flip-chip technology. The optimal value of the offset between the gratings, Off, is then identified through a sweep, which also provides the alignment tolerance.

A summary of the results of the optimizations can be seen in Fig. 3.7, where insertion loss and 1dB bandwidth are plotted as a function of grating length. It is evident, in both cases, that increasing the length of the gratings leads to a decrease in both insertion loss and bandwidth. The decrease in insertion loss is expected and mainly due to the increase of the total scattering-power of the InP grating, which allows it to scatter/capture a greater fraction of the light. The decrease of bandwidth is also expected, due to the decrease of the finite size contribution — see Chapter 2 — which, due to the non perfect matching of the dispersions in the two gratings, plays a role here.

The parameters of the optimal structures are reported in tables 3.2 (InP), 3.3 (Si etched), and 3.4 (Si added). Analyzing the trends in the optimal parameters can indeed give useful information. In the InP part it can be seen that the optimal parameters are more or less the same. This is in agreement with the fact that, given the sub-optimal scattering-strength of the InP platform, the optimal configuration is always the one which maximizes the scattering-strength, and the total scattering-power increases on increasing length.

On the Si side, the opposite is true. The high scattering-strength reachable allows even a short grating to have a sufficient total scattering-power. Thus, when increasing the length, the total scattering power has to be constant, which requires a reduction of the scattering-strength. This is the

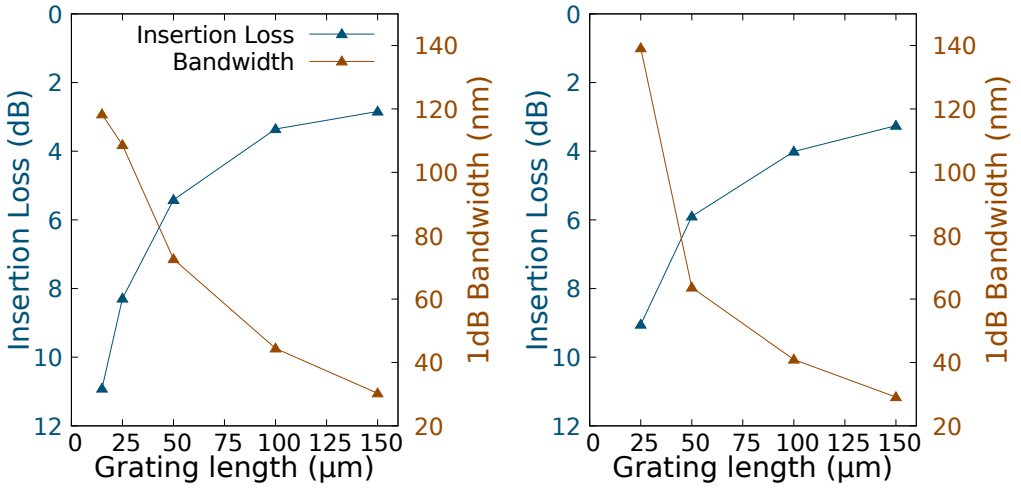

(a) Etched grating-coupler.

(b) Added grating-coupler.

Figure 3.7: Performance summary of the grating-to-grating coupling for both configurations. Operation in both direction has been simulated, showing very similar behavior.

reason why both the optimal etching depth and the optimal thickness of the added silicon layer decrease on increasing length.

The minimum of insertion loss is obtained for a small value of the offset Off, between 3 and 5 µm for every configuration. The tolerance on this parameter is however quite relaxed, starting from a 5 µm alignment tolerance for the shorter gratings and increasing as length increase.

With all these adjustments, an insertion loss of 2.8 dB and 3.2 dB can be reached for the etched and added grating, respectively —see Fig. 3.8. Moreover, the 1dB bandwidth, although much smaller than SOI-to-SOI grating-to-grating coupling, is still around 30 nm, a value comparable with typical fiber-to-grating coupling.

Considering all this, the performances are enough to justify the investigation of this kind of approach as a viable route to efficient and cost-effective light coupling between SOI and InP-based platforms.

3.3 Far-field analysis

Useful information on the performance trends in Fig. 3.7 can be extracted by looking at the emission profiles of the gratings in the far-field. In fact, assuming that the emission of a grating-coupler coincides with the profile it

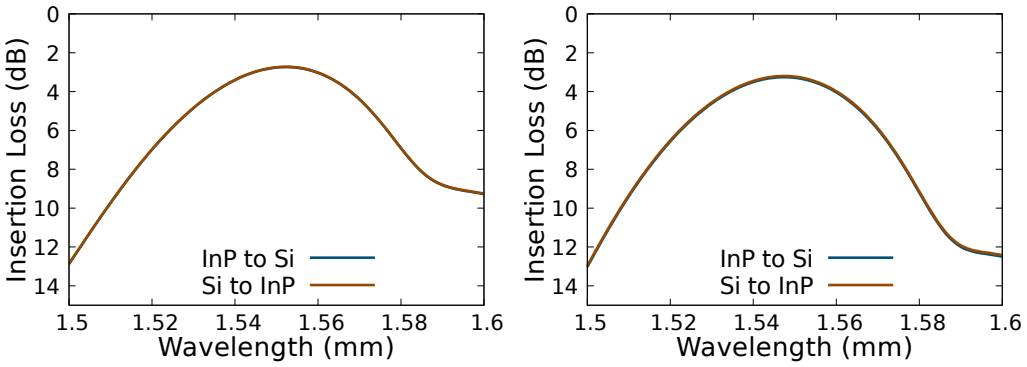

(a) Etched silicon.

(b) Added silicon.

Figure 3.8: Coupling spectra for the best performing case (L=150 µm) of the two coupling configurations here studied. Performances in both directions (Si-to-InP and InP-to-Si) are reported.

can accept as input, coupling between the gratings can take place only when the two far-field profiles overlap.

In the case of two identical gratings, once the mode matching is adequately addressed, the superposition of the far-filed profiles is automatically guaranteed, and almost no finite size effect is visible. This is the reason for the very broadband spectrum experimentally observed [223].

When the two gratings are different, the two far-field profiles do not coincide, and so finite size effects are relevant. For example, in Fig. 3.9 two far-field profiles are plotted for the case of the InP/etched Si coupling and for two different values of the length (25 and 150 µm). It is evident that for the 25 µm long gratings both InP and Si far-field profiles are very broad in angle, thus the overlap region spans all the interesting wavelengths and justifies the broadband behavior. Instead, in the 150 µm long gratings the far-field profiles are much narrower, thus reducing the overlap region and consequently the bandwidth.

In addition, this kind of analysis could also provide some insight on fabrication and alignment tolerances. In particular, errors in the fabrication or in the alignment could determine a small tilt or shift of the far field curve. Due to their very broad profiles, the shorter grating would be quite robust to this kind of errors, since a pretty large deviation would be required to disrupt the overlap. The situation is not the same for the longer grating, whose narrower peaks cause greater sensitivity to small changes. From Fig. 3.9 a tolerance of about 1° on the emission can be estimated.

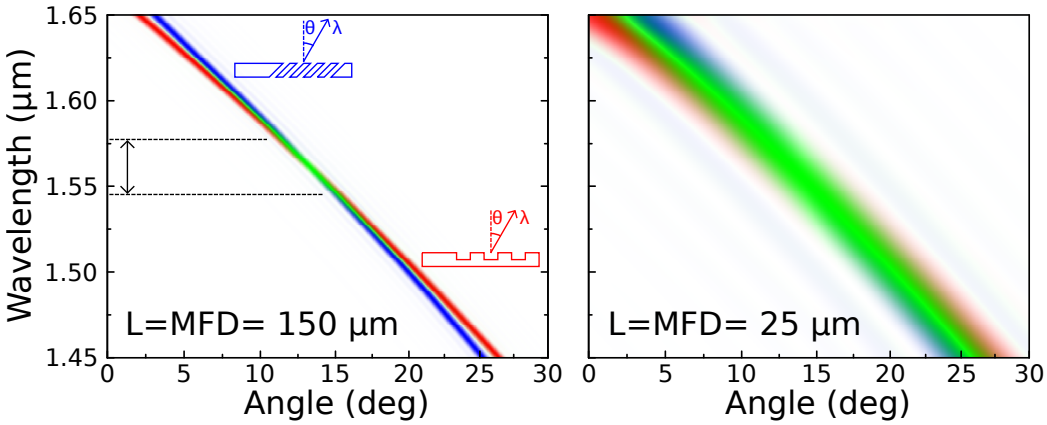

Figure 3.9: Far-field emission profiles of the etched grating for two value of the grating's length. Blue represent Si, red InP and the overlap region is enlightened in green.

3.4 Conclusion

In conclusion, this chapter provides a feasibility study through FDTD simulations of the application of a grating-to-grating approach to the problem of light coupling between Photonic Integrated Circuits of different platforms. In particular, standard SOI and an InP-based platform have been chosen. It has been shown that, due to the limited scattering-strength available in the InP platform, the most straightforward solution to decrease insertion loss is to employ longer-than-normal grating-couplers, which also requires the re-thinking of the SOI grating. By combination of a design rule for apodization and numerical optimization trough PSO algorithm, InP and Si grating-couplers of different lengths have been co-designed, showing that insertion losses of around 3 dB are possible with usable bandwidth. This study could open the way to the use of flip-chip technology for optical connection between different platforms, allowing for easy and cost-effective hybrid integration.

Chapter 4

Slow-light

4.1 Introduction

4.1.1 Slow-light: basic facts

Light propagation, once the constitutive relations are specified, is fully determined by Maxwell equations. For solutions in the form of traveling waves, almost all the important information can be summarized in the so-called dispersion relation, namely the relation between the frequency and wavevector of the wave:

$$\omega = \omega(k) \tag{4.1}$$

Starting from this relation, two different velocities (and related indexes) can be defined:

$$v_p = \frac{\omega}{k} \qquad n_p = \frac{c}{v_p} \tag{4.2a}$$

$$v_g = \frac{\partial \omega}{\partial k} \qquad n_g = \frac{c}{v_g} \tag{4.2b}$$

which are called phase velocity (4.2a) and group velocity (4.2b). Their meaning is different: the phase velocity describes the speed at which local maxima or minima of the field travel through space, while the group velocity gives the speed of the general envelope of the field, and is usually regarded as the speed at which information coded in light can travel. In uniform and non-dispersive media, such as vacuum, these speeds are the same, but in general no direct relation exists between the two. Indeed, phase and group velocities can be equal, different in values, or even with opposite sign.

Thus, when speaking of slow-light, it is of paramount importance to clarify which velocity is being referred to. In the most used definition, slow-light

refers to a situation in which the group velocity is made very low (or equivalently the group index is made very high).

Early attempts to finely controlling light dispersion have relied on complex material properties and techniques, such as Electromagnetically Induced Transparency (EIT) [229], coherent population oscillations [230], and even Bose-Einstein condensates [231]. Typically, these setups are quite complex to realize, especially Bose-Einstein condensates, which require nano-Kelvin temperatures.

More recently, the advent of nano-photonics has opened the way to systems in which slow-light features can arise only by the geometrical properties of the structure, even in the presence of non dispersive materials [232]. Even within this particular application, Silicon Photonics has offered itself as an ideal platform, both due to its physical properties and its mature level of technology.

Slow-light has indeed the potential to bring great benefits to typical Photonic Integrated Circuits, being able both to provide new functionalities or to improve on existing ones. Slow-light can in fact provide a field enhancement effect similar to the one found in cavities, but retaining all the features of a traveling wave [233]. This enhancement in light matter interaction can be exploited in many fields, such as non-linear optics [234, 235], sensing applications [236, 237], and electro-optical modulators [154, 156, 158, 238]. Possibilities of using slow-light for the realization of all-optical buffers and memories have also been investigated [239].

When dealing with slow-light in integrated circuits, various figures of merit have to be taken into consideration. The main concerns are off course maximum group index, operational bandwidth, and the Group Velocity Dispersion (GVD). The first two figures of merit are usually summarized in their product, called group-bandwidth product or GBP. This because usually slow-light is based on some sort of resonant mechanism, and thus reaching very high group index is not a problem in itself, but usually happens at the expense of bandwidth. Thus, the GBP is a good indicator of the performance of a slow-light device. Almost as important is the GVD, namely the derivative of the group index as a function of frequency. Since this value is directly proportional to the amount of distortion suffered by a signal traveling through the slow-light device, it is important to keep GVD as low as possible. Other important figures of merit are of course the amount of losses, the ease of fabrication of the structure, the coupling losses to a conventional waveguide and the total footprint of the device.

Many ways to generate slow-light in nano-photonics have been explored over the years. The first one is without doubt band-edge slow-light, which relies on the fact that band dispersion in a periodic patterned structure,

whenever a band gap exists, has to arrive flat at the edges of the gap [240]. One simple way to realize that, while retaining waveguiding along one dimension, is to use the fundamental band of a grating waveguide [241, 242]. This approach is not so optimal for GBP and GVD, but is surely the simplest, and it provide quite low losses.

Another approach is to tailor the waveguide parameters to obtain slow-light features away from the band gap, for example by using non-fundamental bands in grating waveguides [243], slotted or holey waveguides [244, 245], or W1 waveguides in PhC Slabs [37, 246, 247, 248]. This approach can indeed deliver high GBP and low GVD, but usually with the drawback of a much more complex design or fabrication and increased losses, especially due to disorder.

Still, another approach is the one of Coupled Resonator Optical Waveguides (CROWs) [249], where the slow-light effect can arise, in a sort of thigh-binging model, from the interaction between many cavities. Early solutions were based on micro-ring [250] or micro-disk [251] resonators, but other configurations are possible, such as nano-beam [252] or PhC Slab based [253] resonators. In the last class, in particular, a great variety of structures has been proposed, such as simple defect cavities [254, 255], L3 cavities [256, 257], and waveguide-coupled cavities [258]. These solutions can indeed deliver impressive performance when considering GBP and GVD, but usually at the price of more complex fabrication and higher losses. In addition, the flexibility of PhC Slabs allows for other approaches, such as the all-optical analog of the EIT [259] or adiabatic bandwidth compression [259].

4.1.2 Silicon grating waveguides

This chapter of the thesis is devoted to the analysis of slow-light arising from the band-edge effect in silicon grating waveguides. Although better approaches in terms of performance have been proved, grating waveguides remain the best approach in terms of fabrication ease, and the most suited to be integrated in current high-volume photonic technology. Moreover, due to the operation below the cladding light line, the relevant loss mechanisms are only the extrinsic ones, such as disorder induced loss or Rayleigh scattering, which are technology dependent and are expected to go down as technology improves.

The research here presented is carried out in the framework of the European Project COSMICC — CmOs Solutions for Mid-board Integrated transceivers with breakthrough Connectivity at ultra-low Cost. The main aim of this project is the realization of low-cost and energy-efficient integrated transceivers. At this scope, slow-light devices could be used to enhance the

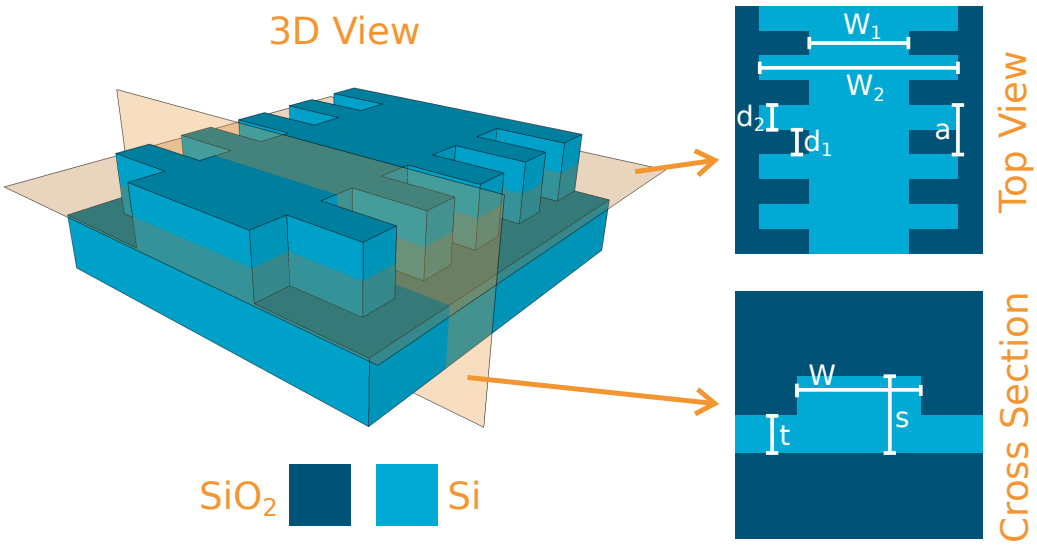

Figure 4.1: Graphical representation of the structure and geometrical parameters of the silicon grating waveguide analyzed in this chapter. The only fixed parameter is the silicon thickness s=310 nm.

modulation effect in integrated silicon phase shifter, leading to more compact and efficient integrated Mach-Zehnder modulators.

For the structure under examination — see Fig. 4.1 — the platform available at STMicroelectronics [260, 261], partner of the COSMICC project, will be assumed as a guide. The features of the platform are a 310 nm thick silicon layer (s=310 nm) with the possibility of two etching depths, of 160 and 260 nm (thus, t=150 or 50 nm, respectively). Consequently, with the exception of the silicon thickness s, all other parameters will be varied during the analysis. The period a is chosen different for each structure, in order to keep the lower band edge at the standard telecom wavelength of 1.3 µm.

The study is carried out using the High Performance Computing resources granted by CINECA under the ISCRA initiative, in the framework of two projects: SlowWave and TapeSlow. The calculations here presented have required a total of about 60000 CPU hours.

The chapter is organized as follows: in the first part the slow-light performance as a function of the geometrical parameters is analyzed, while in the second the problem of the coupling of light to/from conventional waveguide is discussed.

4.2 Numerical method and band calculation

The numerical calculations are performed using the Aperiodic-Fourier-Modal-Method [183], a frequency-domain method based on the scattering matrix method [182, 262], with a modification allowing for the treatment of aperiodic systems — see Sec. 1.3.3 and Appendix A and B for a complete description of the method.

Since this is a frequency based method, direct calculation of the photonic bands, especially in the region of high group index near the band edge, would require a very fine grid of energy points, up to hundreds for each structure. Even recurring to High-Performance-Computing (HPC), the computational effort of such direct approach would be too heavy and time-consuming.

Thus, taking inspiration from [241], a simple analytical expression of the photonic band near the band edge is used to fit the dispersion curve calculated only in a few energy points. This allows for a reduction of the computational effort by at least one order of magnitude. The more this analytical expression is close to the actual dispersion curves, the less error is introduced in this step. For this reason, the simple quadratic model presented in [241], although quite good, is improved in favor of an expression derived from perturbation theory.

In the following, the derivation of such analytical expression is discussed, followed by an example showing the goodness of such approach.

4.2.1 Fitting function from perturbation theory

The derivation here presented, which takes inspiration from the Nearly-Free Electron model in Solid State Physics [263], is based on the perturbation of free-space propagation with a dielectric constant variation $\Delta\varepsilon(\mathbf{r})$ containing only one Fourier component.

It starts from the master equation (Eq. 1.6) for the magnetic field, which is here recalled:

$$\nabla \times \left(\frac{1}{\varepsilon} \nabla \times \mathbf{H} \right) = \frac{\omega^2}{c^2} \mathbf{H} \tag{4.3}$$

From this starting point, by employing 2D approximation (propagation only in the xy plane), focusing only on H, or TE, modes (even modes with respect to the xy mirror symmetry), and defining $\eta = 1/\varepsilon$, it is possible to write for the H_z component of the magnetic field the following equation:

$$-\partial_x \left(\eta \partial_x H_z \right) - \partial_y \left(\eta \partial_y H_z \right) = \frac{\omega^2}{c^2} H_z, \tag{4.4}$$

which, by expanding the magnetic field on pseudo-Fourier basis :

$$H_z(\mathbf{k}) = \sum_{\mathbf{G}} c_{\mathbf{k}+\mathbf{G}} e^{i(\mathbf{k}+\mathbf{G})\cdot\mathbf{r}}, \tag{4.5}$$

can be rewritten as:

$$\sum_{\mathbf{G}'} \left[(\mathbf{k}+\mathbf{G})\cdot(\mathbf{k}+\mathbf{G}')\eta(\mathbf{G}-\mathbf{G}') - \frac{\omega^2}{c^2}\delta_{\mathbf{G}\mathbf{G}'} \right] c_{\mathbf{k}+\mathbf{G}'} = 0. \tag{4.6}$$

At this point, the term $\eta(\mathbf{G}-\mathbf{G}')$ is split in a background uniform index plus a small perturbation $\Delta\eta$:

$$\eta(\mathbf{G}-\mathbf{G}') = \eta_0\delta_{\mathbf{G}\mathbf{G}'} + \Delta\eta(\mathbf{G}-\mathbf{G}'), \tag{4.7}$$

so that Eq. 4.6 can be rewritten:

$$\left[(\mathbf{k}+\mathbf{G})^2 - \frac{\omega^2}{c^2} \right] c_{\mathbf{k}+\mathbf{G}} + \sum_{\mathbf{G}'} (\mathbf{k}+\mathbf{G})\cdot(\mathbf{k}+\mathbf{G}')\Delta\eta(\mathbf{G}-\mathbf{G}')c_{\mathbf{k}+\mathbf{G}'} = 0. \tag{4.8}$$

Now, if $\Delta\eta$ is set to 0, all equations decouple and all that is left is:

$$\omega(\mathbf{k}+\mathbf{G}) = c\sqrt{\eta_0}|\mathbf{k}+\mathbf{G}| = \frac{c}{n}|\mathbf{k}+\mathbf{G}| \tag{4.9}$$

which is just the empty lattice approximation, or an alternative way to see the standard linear dispersion of electromagnetic waves in a uniform medium.

The interesting physics is obtained when $\Delta\eta$ different from 0 are allowed. In particular, if the problem is reduced to 1D (only vectors along x are permitted) and in the expansion of $\Delta\eta$ only the fundamental Fourier component $G = -2\pi/a$ is retained (where a is the period of the perturbation), Eq. 4.8 can be cast in matrix form:

$$\begin{vmatrix} \eta_0 k^2 - \frac{\omega^2}{c^2} & k(k+G)\Delta\eta(G) \\ k(k+G)\Delta\eta(G) & \eta_0(k+G)^2 - \frac{\omega^2}{c^2} \end{vmatrix} = 0, \tag{4.10}$$

whose analytical solution leads to:

$$\frac{\omega^2}{c^2} = \frac{\eta_0[k^2+(k+G)^2] \pm \sqrt{\eta_0^2[k^2+(k+G)^2]^2 + 4[k(k+G)]^2\Delta\eta^2(G)}}{2}. \tag{4.11}$$

By inserting $G = -2\pi/a$ and defining $U = \Delta\eta(G)/\eta_0$ and $n = \sqrt{1/\eta_0}$, it can be expressed as:

$$\frac{\omega^2}{c^2} = \frac{k^2 + \left(\frac{2\pi}{a}\right) \pm \sqrt{\left[k^2 - \left(\frac{2\pi}{a}-k\right)^2\right]^2 + 4k^2\left(\frac{2\pi}{a}-k\right)^2 U^2}}{2n^2}. \tag{4.12}$$

By redefining in terms of the adimensional distance from the band edge ($k = \pi/a(1-\delta)$) and adimensional frequency ($\Omega = \omega a/2\pi c$), Eq. 4.12 can be rewritten as:

$$\Omega^2 = \frac{1+\delta^2 \pm \sqrt{4\delta^2 + (1-\delta^2)^2 U^2}}{4n^2}. \tag{4.13}$$

At this point it is worth recalling that the unperturbed starting point should be a ridge waveguide, and not the free space. The easiest way of including that is to insert another parameter which allows for the shifting in energy of the center of the band gap. Thus, choosing the minus sign for the solution, since the interest lies in the lower band, the fitting formula becomes:

$$\Omega(\delta, \Omega_0, n, U) = \left[\Omega_0^2 + \frac{\delta^2 - \sqrt{4\delta^2 + (1-\delta^2)^2 U^2}}{4n^2}\right]^{\frac{1}{2}}. \tag{4.14}$$

This gives an analytical expression of the lower photonic band near the band edge, which is then used for the fitting of the numerically calculated bands.

4.2.2 Numerical calculation and fit testing

In this section, a discussion on the validity of the fitting procedure is presented. An example of the results obtained by direct calculation of the bandstructure of a grating waveguide is reported in Fig. 4.2a. As can be seen, the full band map is quite complex and complicated by spurious solutions due to the use of a supercell, but the interesting band, namely the lowest band near the band edge, is quite easy to isolate from the others.

Once the fundamental band is isolated, the fitting procedure can be carried out. As an example, in Fig. 4.2b a fit of the fundamental band using only few energy point is presented. It is evident that the agreement between the fitting procedure and the direct calculation is quite good. This is indeed remarkable, since the very coarse grid used for the calculation does not always provide an energy point near the band-edge, and nevertheless the dispersion in the slow-light region is reproduced by the fit with great accuracy.

Moreover, this fitting procedure shows enough precision to capture the difference in the bandstructure and in the group index when different structures are examined, as it is shown in Fig. 4.3. Thus, this procedure allows for the analysis of the slow-light performances of a broad space of parameters, which would be prohibitive otherwise.

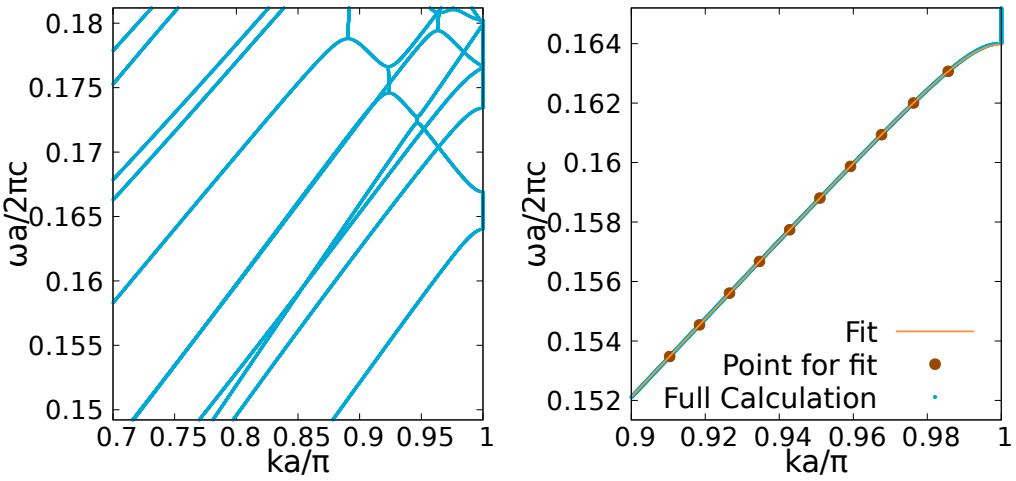

(a) Full bandstructure.

(b) Fundamental band and fit.

Figure 4.2: Full bandstructure and fit for the configuration with parameters W_1 =400 nm, W_2 =400 nm, $d_2/a = 0.5$, t =150 nm, and a =213 nm.

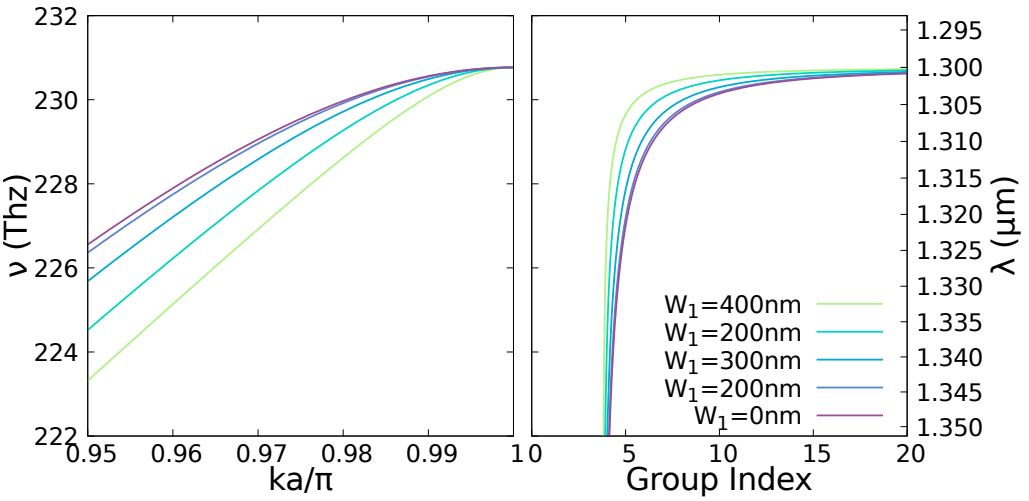

Figure 4.3: Fundamental bands and related group indexes for different values of W_1 reproduced by the fitting procedure. All other parameters are as in Fig. 4.2, except the period a which is chosen to give the band edge at λ =1.30 μm.

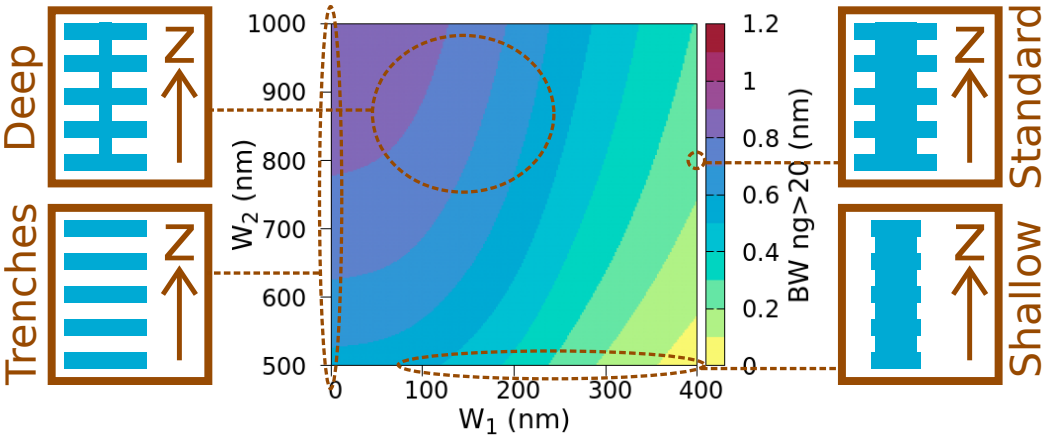

Figure 4.4: Visualization of the slow-light bandwidth ($n_g > 20$) as a function of W_1 and W_2.

4.3 Results

Once a valid method for the calculation of the bandstructure is available, what is missing is a quick way to compare the performances of different structures. To this scope, the definition of one or more figures of merit, allowing to capture the slow-light performances with only a few numbers, is of great importance. Maximum group index is not a good figure of merit in this case, since it diverges at the band edge. A valid figure of merit is instead found in the slow-light bandwidth, namely the width of the region in which the group index is higher than a certain target value.

By using this new figure of merit, general trends in the slow-light performances as a function of geometrical parameters can be easily visualized. For example, in Fig. 4.4 the slow-light bandwidth ($n_g > 20$) as a function of W_1 and W_2 is reported, for t and d_2/a fixed at 150 nm and 0.5, respectively. As can be seen, it is possible to affect the slow-light bandwidth by properly tuning the geometrical parameters. In particular, the slow-light bandwidth can be increased form $\approx$0.2 nm of the standard structure [242] known in literature, up to almost 1 nm.

A few things can now be noted: first, the absolute value of the slow-light bandwidth. Although it can be increased using the right geometrical parameters, it remains always very small, no greater than 1 nm. Thus, it seems that grating waveguides are not the most suitable candidates for obtaining very high group index. A more realistic use of these structures would probably be to settle for a moderately high group index, such as 10, while retaining a

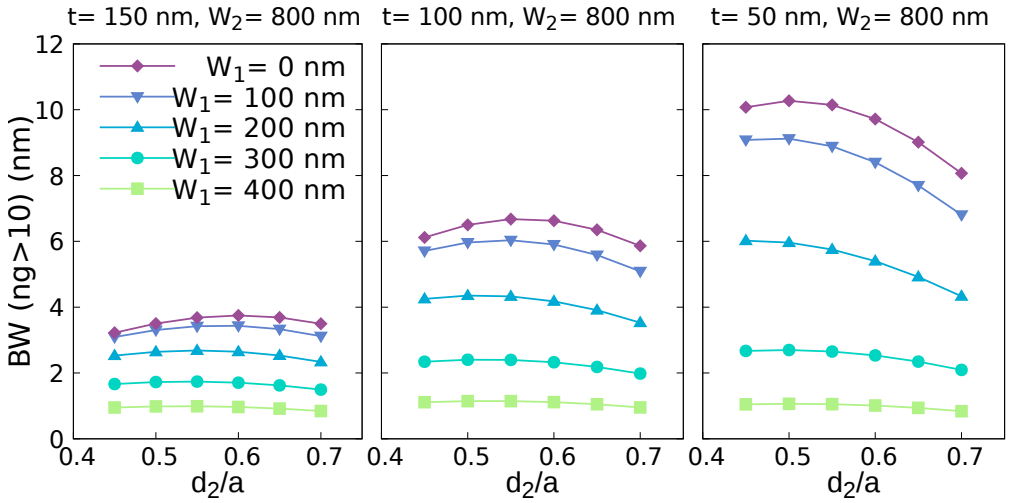

Figure 4.5: Representation of the slow-light bandwidth ($n_g > 10$) as a function of d_2/a for different values of W_1 and t.

more meaningful bandwidth, at least of a few nm.

Second, it is worth noting that the general trend in the slow-light bandwidth as a function of W_1 and W_2 is quite simple: it increase monotonically on decreasing W_1 and increasing W_2. A a consequence, the best structures in term of slow-light bandwidth are the ones in which $W_1 = 0$, namely a lattice of trenches. However, it is important to notice that even structures with a W_1 different from 0 can express good performance, almost at the level of the lattice of trenches, provided W_1 is kept sufficiently small ($\approx< 100\,\text{nm}$).

Keeping these consideration in mind, the analysis is expanded to other geometrical parameters, such as the Si thickness in the cladding region t and the ratio d_2/a. Some of the results obtained are reported in Fig. 4.5 and 4.6.

As can be seen, the slow-light bandwidth in not much affected by the ratio d_2/a. In fact, for the sets of parameters analyzed, the bandwidth-d_2/a curves are nearly flat, with a maximum between 0.5 and 0.6.

The effect of the cladding silicon thickness t is, instead, much more pronounced, as its reduction produces a great increase in the slow-light bandwidth, up to a value of almost 10 nm for t =50 nm. Full etched configurations are not explored, although they would probably yield even better performances, since they would not permit electrical contact to be realized, impairing one of the targeted application of such structures, namely phase shifters for electro-optical modulators.

For details on all the simulated structures, see Supplementary Materials of [264], where the fit parameters representing the photonic bands through

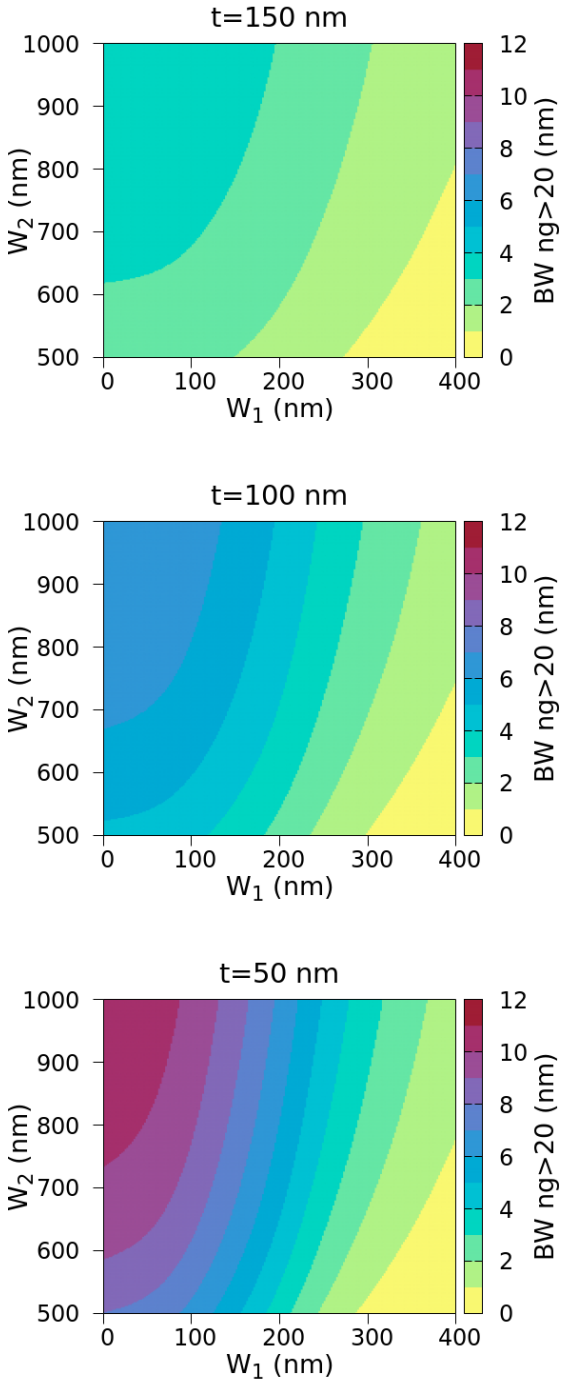

Figure 4.6: Representation of the slow-light bandwidth ($n_g > 10$) as a function of W_1 and W_2 for different values of t and $d_2/a = 0.5$.

Eq.4.14 and the related periods are reported for every analyzed waveguide (for a total of 37 638 different parameter configurations).

In conclusion, in this section it has been shown that by changing the geometrical parameters of grating waveguides it is possible to increase the slow-light bandwidth to values higher than the ones reported until now for silicon grating waveguides [242]. As a general guideline, the slow-light bandwidth seems to be proportional to the effective index contrast between the thin and thick sections of the waveguide, which can be increased by shrinking the internal width W_1 or the cladding Si thickness t.

4.4 Adiabatic taper

4.4.1 The problem of light coupling

Although obtaining the best possible slow-light performances is an interesting theoretical topic, in view of device applications, they are only a part of a more complex system, and the problem of light coupling from a conventional rib waveguide has to be taken into account. Due to the high index and modal mismatch between conventional and slow-light waveguides, direct butt-coupling between the two could lead to significant back-reflection and scattering losses.

Thus, a dedicated device is required to bridge the gap between conventional and slow-light waveguides. This is usually done by an adiabatic taper (simple [242] or optimized [241, 265]), a sub-wavelength taper [114], or a dedicated mode converter [266] (usually employed for coupling to bands other than the fundamental one).

All these approaches, with the exception of the mode converter and, if done properly [191], of the sub-wavelength taper, require a sort of continuous adaptation of the geometry from a conventional rib waveguide to a grating one. Unfortunately, all current fabrication techniques have to deal with a minimum feature size problem, thus making a continuous adaptation to the best performing grating waveguide, i.e. the trenches one, not practically possible. However, by carefully looking at Fig. 4.6, it is possible to notice that only a small drop in slow-light bandwidth is expected when taking a value of W_1 which is not zero, but just high enough to be compatible with fabrication. Thus, in the following, a deeply corrugated waveguide (W_1=100 nm and W_2=800 nm) will be taken as the ideal candidate for slow-light applications, since it features good performance and compatibility with all current lithographic techniques.

The design of a suitable structure for light coupling from conventional

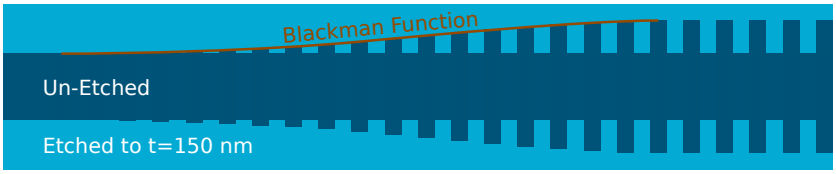

(a) Standard waveguide [242].

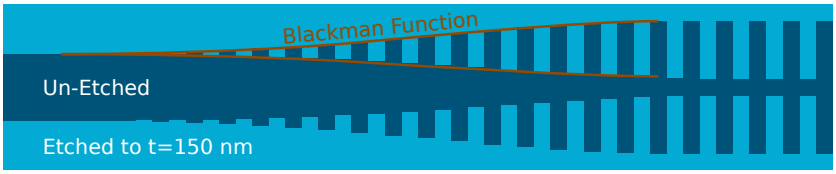

(b) Deeply corrugated waveguide.

Figure 4.7: Sketch of the structure of a simple Blackman taper for standard and deeply corrugated waveguides.

to slow-light waveguides can still be addressed with the A-FMM method. Such method, in fact, allows for the calculation of the transmission and reflection spectra of a finite length of slow-light waveguide, surrounded by an arbitrary coupling structure. However, such calculations can be quite heavy, especially if the coupling structure requires many different layers to be correctly reproduced. Indeed, the calculation of a single transmission spectrum through a structure composed of hundreds of layers can take up to 1000 CPU hours. Consequently, numerical optimization of the coupler, which would require many evaluations of the transmission, is almost impossible, thus ruling out solutions based on optimized tapers or mode converters. For this reason, the only solutions analyzed in this thesis are the simple adiabatic taper and the subwavelength one.

4.4.2 Simple adiabatic taper

In this section the simpler solution for the taper will be analyzed, taking inspiration from [242], where the adiabatic taper is designed by gradually turning on the periodic patterning using a simple Blackman function. This solution is proven to work with low group index waveguide (W_1 =400 nm, W_2 =800 nm, and t =150 nm — see Fig. 4.7a), and now its use for deeply corrugated waveguides — see Fig. 4.7b — will be analyzed.

To do this, A-FMM is employed to calculate the transmission through a finite length of slow-light waveguide, joined at both ends to conventional rib waveguides by two tapered sections of variable length. The results of such calculations, showing the transmission through a 128 period long grating

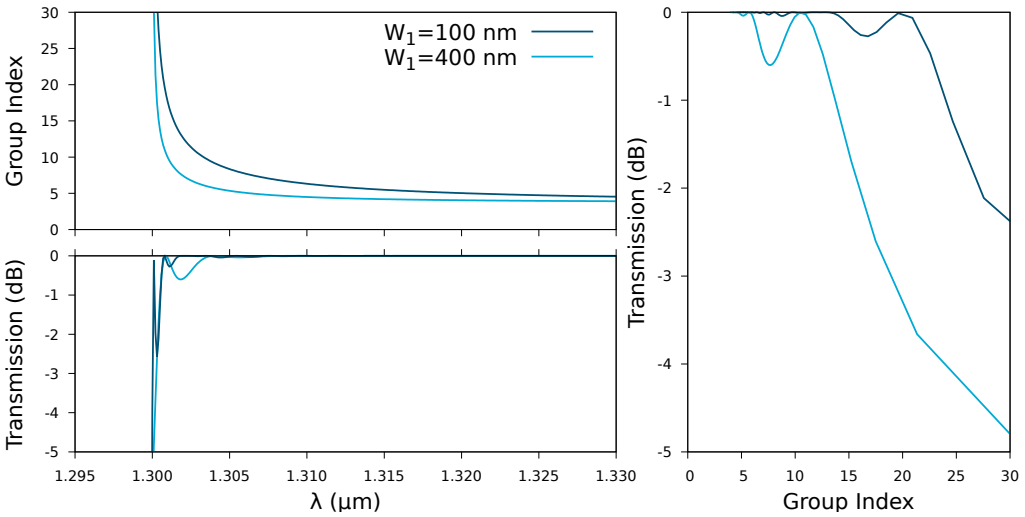

Figure 4.8: Representation of the transmission as a function of wavelength and group index. For completeness, the group index as a function of wavelength is also reported.

waveguide between two 150 periods long tapers, are reported in Fig. 4.8 for two values of W_1: 400 and 100 nm. The period is kept constant throughout the structure, equal to the one of the slow-light section, namely 213 and 218 nm for W_1 equal to 400 and 100 nm, respectively. Such calculations show that a 150 period long taper (≈30 µm) is more than enough to give high transmission, and that the reduction of W_1 from 400 to 100 nm does not significantly alter the performance of the taper. On the contrary, this allows the structure to keep high transmission up to a greater value of n_g. Indeed, the transmission remain better than 1 dB up to a n_g value of ≈ 15 for W_1 =400 nm, which increases to ≈ 25 for W_1 =100 nm.

At this point, it is time to consider the effect of the Si thickness in the cladding region t, in order to design an adiabatic taper for the more convenient thicknesses t =100 nm and t =50 nm. The same strategy has been followed, and the transmission through a slow-light line consisting of 256 periods, connected using Blackman tapers of variable lengths, is reported in Fig. 4.9 for two different values of t, namely 100 and 50 nm (W_1 =100 nm, W_2 =800 nm, and a=226 and 234 nm for t=100 and 50 nm, respectively). It is quickly evident that the taper performances are much worse than in the t =150 nm case. For t =100 nm, to obtain useful transmission up to near the band edge tapers between 300 and 400 period long (≈80 µm) are needed. For t =50 nm, even a 1000 period long taper (although only the transmission up to a 500 period long taper is reported) is not enough to keep the transmission

at acceptable levels.

Moreover, in particular for the t =50 nm case, the behavior of the transmission as a function of wavelength is not trivial at all, as it features very finely spaced oscillations, modulated by an envelope which also oscillates, but at at a much slower rate. The rapid oscillations are easily explained, since they are compatible with Fabry-Perot oscillations of the entire delay line. Proof is offered by Fig. 4.10, in the fact that the rapid oscillations become denser and denser as the length of the slow-light section is increased.

Another interesting feature of Fig. 4.9 is how the envelope of the transmission does not seem to depend on the length of the line, marking it as a feature of the taper alone. To understand the reason of the envelope oscillations, it is important to recall that reflections inside such a taper arise mainly due to contra-directional coupling between the two contra-propagating modes [267]. By this argument, oscillations in the reflection should show a dependence as $\sin^2(\overline{\Delta\beta}L/2)$, where $\overline{\Delta\beta}$ is the average difference in wavevector between the two contra-propagating modes, and L is the length of the taper.

Moreover, this behavior does not drastically change by changing the function defining the adiabatic taper, unless a proper optimization is carried out [265]. For example, in Fig. 4.11 the transmission is plotted as a function of the taper length, but using a linear function for the taper profile, instead of a Blackman function, and basically the same behavior of Fig. 4.9 can be seen.

Thus, the simple solution of the adiabatic taper has demonstrated good transmission near the band edge, provided the group index is not too high. Indeed, by moving to a more performing grating waveguide, characterized by a deeper etch, this solution quickly looses effectiveness.

4.4.3 Sub-wavelength taper

This section will be devoted to the analysis of the sub-wavelength taper. This solution employs a very fine patterning of the dielectric function to make the resulting structure behave as an uniform medium. Such approach has already been proven useful for light-coupling between waveguides with quite different characteristics, mainly in terms of modal index and size. Most notable examples include fiber-to-chip edge-couplers [44, 191] and Multi-Mode-Interferometers [58].

The adaptation of this concept to the slow-light waveguide of this thesis leads to the design of a kind of double-step taper — see Fig. 4.12. The first section is the proper sub-wavelength taper, where the geometry of the waveguide is linearly adapted from a conventional rib to a deeply corrugated waveguide. In this section the period is held constant, but it is smaller than the one needed for the slow-light waveguide. This pushes the band edge to

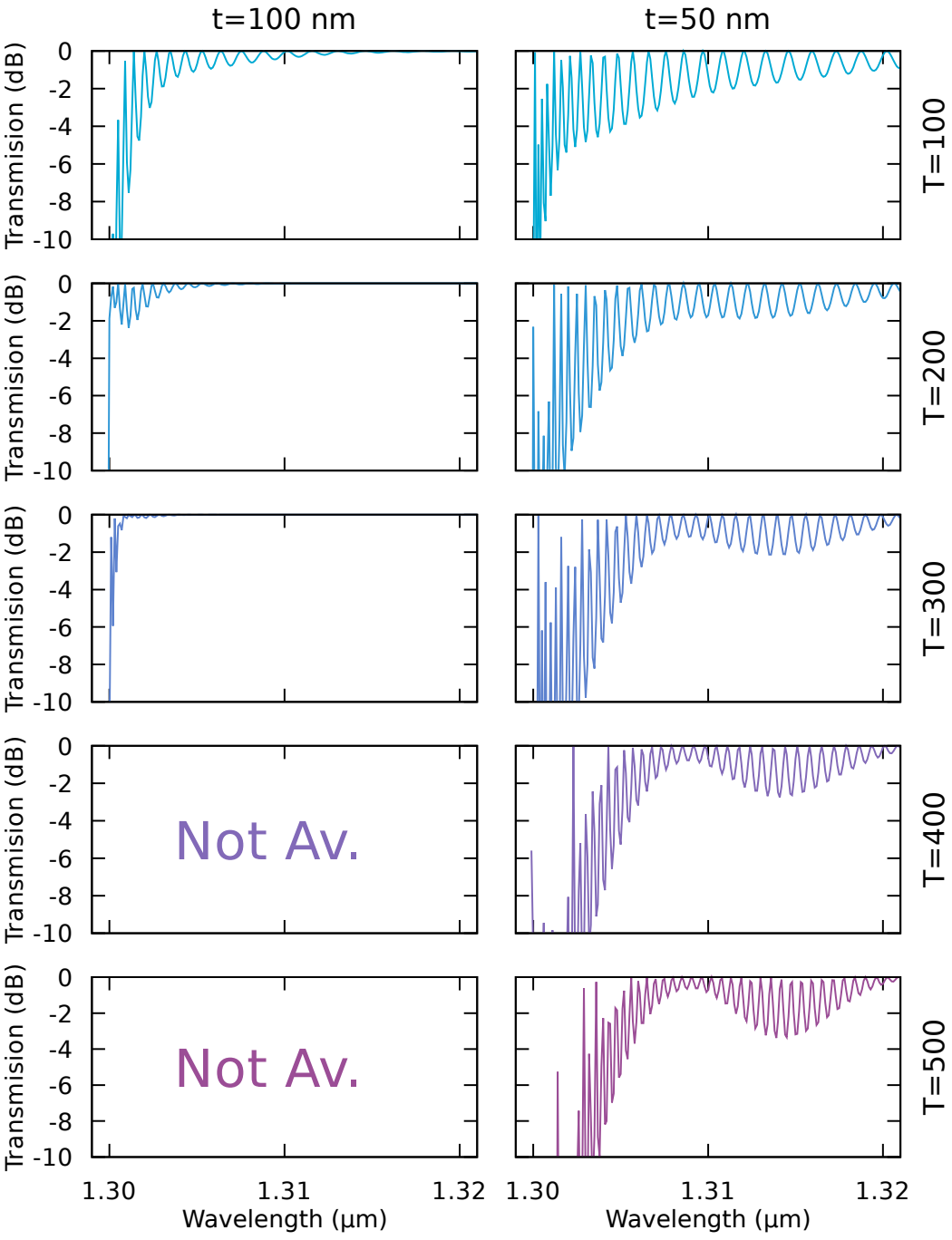

Figure 4.9: Transmission through a 256 long slow-light waveguide for different values of t and lengths of the tapers, measured in the number of periods T. Fixed parameters are W_1 =100 nm and W_2 =800 nm. The tapers are designed using a Blackman function.

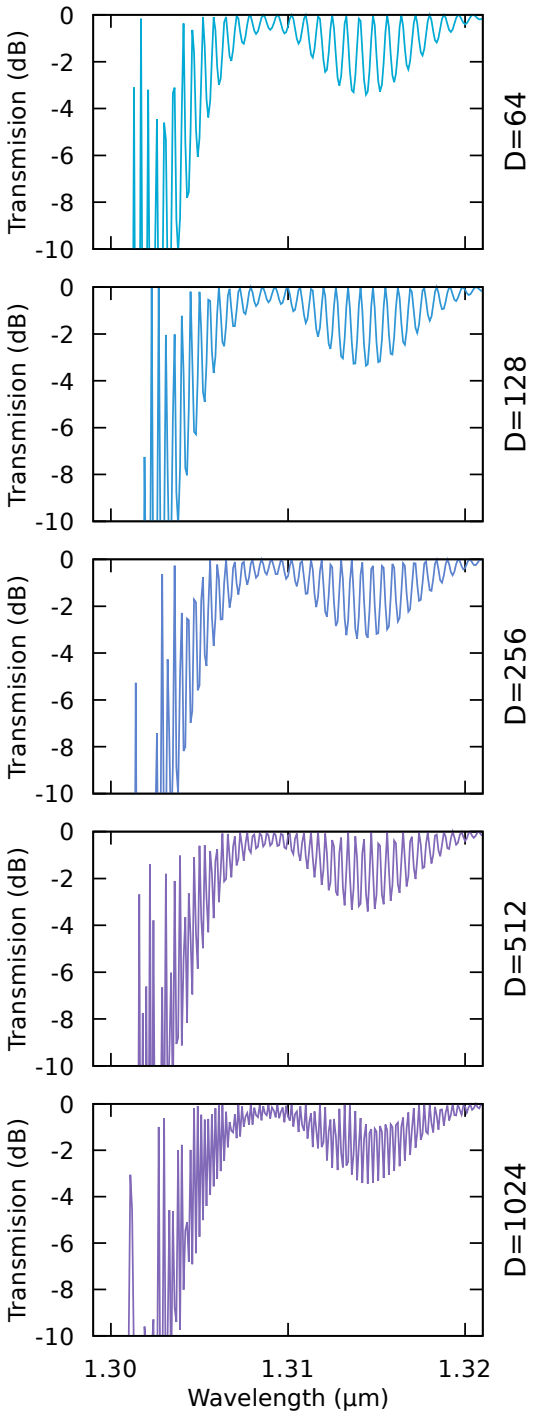

Figure 4.10: Transmission as a function of the length (D=number of periods) of the delay line. The taper length is fixed at L=500 periods. Other fixed parameters are W_1 =100 nm,W_2 =800 nm, and t =50 nm.

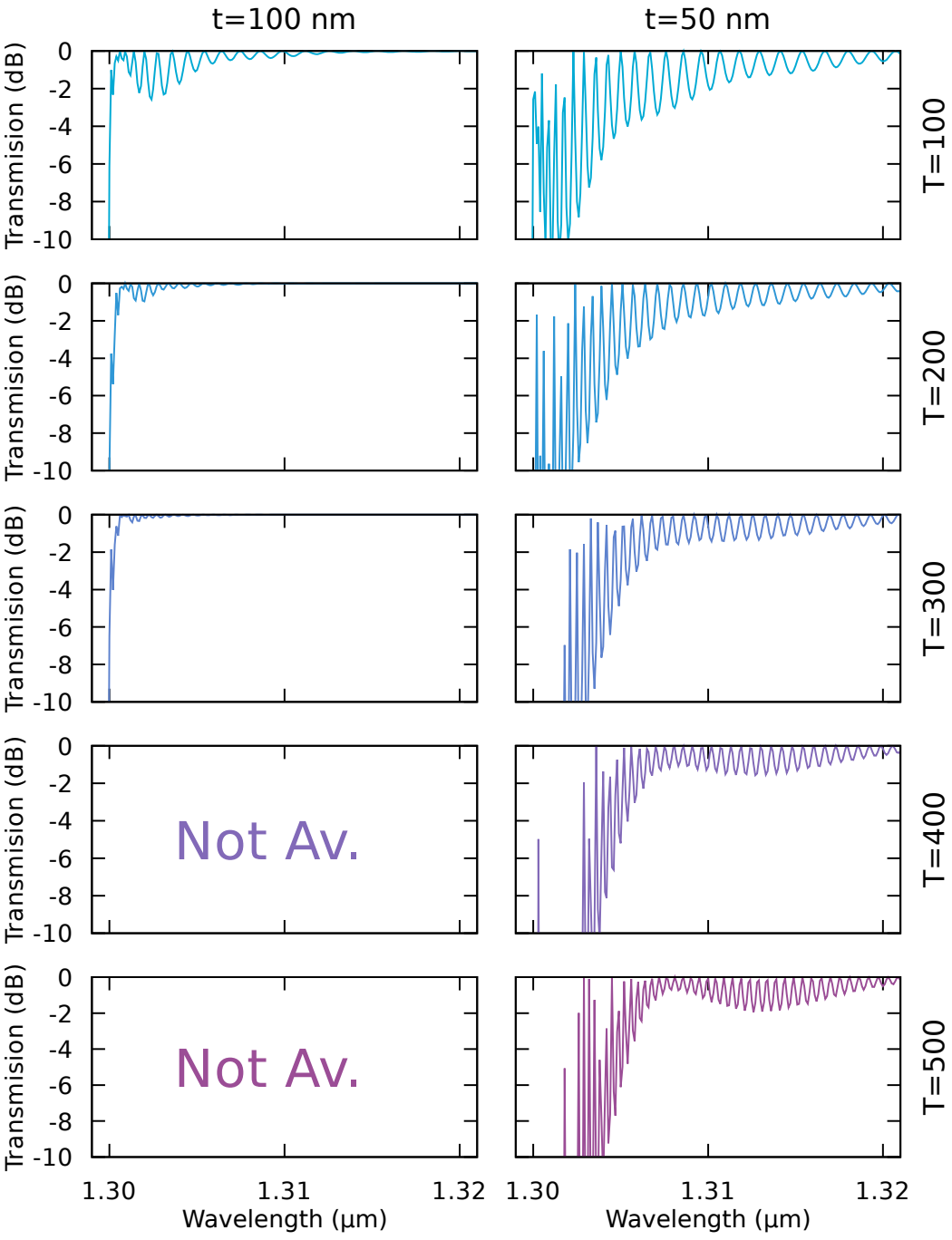

Figure 4.11: Transmission through a 256 long slow-light waveguide for different values of t and lengths of the tapers, measured in the number of periods T. Fixed parameters are W_1 =100 nm and W_2 =800 nm. The tapers are designed using a linear function.

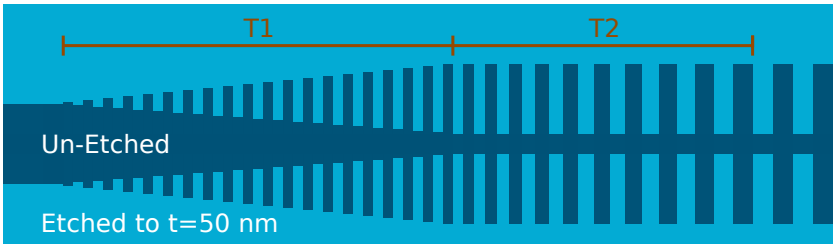

Figure 4.12: Sketch of the subwavelegnth taper for the case of the high group index waveguide (W_1=100 nm, W_2=800 nm, t=50 nm). The variation of the period is exaggerated for better visibility.

higher energies, forcing the waveguide to work in the sub-wavelength regime. In such regime, the waveguide behaves as if it were made of a single uniform material, and thus the optical properties of the mode are less sensitive to the details of the underlying geometry. Thus, it is possible for the light to be coupled from a standard waveguide to a deeply corrugated one (not in the slow-light regime) without incurring in great reflections.

In the second part of the taper the real adaptation to the slow-light waveguide takes place. In fact, in this section the transversal geometry of the wavelength is not modified, but the period is linearly adjusted to the one of the desired slow-light waveguide. The hope is to keep reflection low also in the second part, which is only responsible for the gradual modification of the group index, since the geometry of both the waveguide and, at least in part, of the optical mode have already been adjusted by the first part.

This solution has been analyzed only for the slow-light waveguide with deeper etch (t=50 nm), since it is for this configuration that the simple adiabatic taper does not work. The period of the sub-wavelength taper is taken to be 220 nm, which is a small enough value to move the band-edge up to a wavelength of around 1.24 µm, sufficiently far to keep low reflection in the first part of the taper. The period in then linearly varied in the second part up to 234 nm, the target value for the slow-light waveguide.

For these calculations, the same setup as the previous section has been followed. The transmission through a 256-period long slow-light waveguide for different lengths of the sections of the taper (measured in number of periods T1 and T2) has been calculated, and it is plotted in Fig. 4.13. It is promptly evident that this solution yields greatly improved performance in terms of transmission, although some reflection near the band edge is still present. As a matter of fact, the reflection seems to be much more dependent on the length of the second part than on the one of the first. Indeed, it can be seen from the figure that doubling the length of the first section (from 50 to

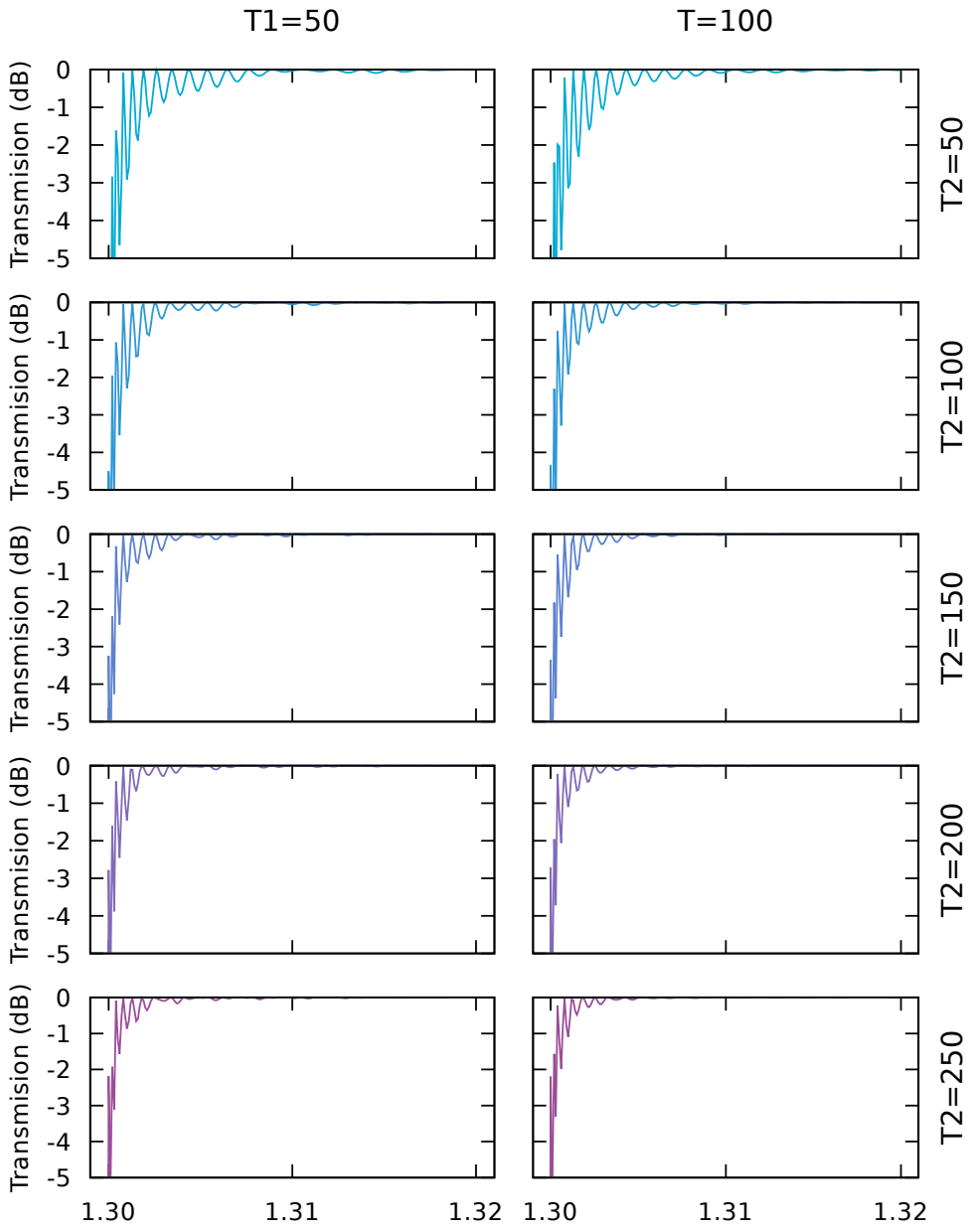

Figure 4.13: Transmission through a 256 long slow-light waveguide with high group index (t=50 nm). The transmission is plotted for different lengths of the taper's sections (expressed in number of periods).

100 periods), while keeping the length of the second part constant, improves the transmission only marginally.

In conclusion, it has been proven that the sub-wavelength approach has the potential to realize a good connection between conventional and slow-light waveguides, since, even in this simple case, it can deliver losses in the transmission lower than 1dB in a wide range of wavelengths, excluding 1 or 2 nm in the proximity of the band edge. Furthermore, it is worth noting that this design is still not optimized, and that by suitable optimization an improvement of performance could be expected. Indeed, such an approach could even be viable for coupling light in the marginally more performant trenches waveguide.

4.5 Conclusion

In conclusion, the slow-light performances of silicon grating waveguides have been theoretically analyzed. It has been shown that, by carefully optimizing the geometrical parameters, an almost tenfold increase in the slow-light bandwidth ($\approx$10 nm for group index $n_g > 10$) can be obtained with respect to structures known in the literature [242]. The best performing waveguide in term of slow-light bandwidth has turned out to be the lattice of trenches, namely all the structures in which $W_1 = 0$.

In addition, the problem of light coupling from conventional rib to a deeply corrugated waveguide in the slow-light regime has been addressed. Two solutions have been analyzed: a simple adiabatic taper and a double step sub-wavelength taper. The first solution has proven valid only for the slow-light waveguide with lower group index (namely the t=150 nm one), being able to keep high transmission with a relatively short taper (150 periods, $\approx$ 30 µm). However, the same solution is not viable for the slow-light waveguide with higher group index, i.e., t=50 nm. Indeed, even a very long taper (1000 periods, $\approx$ 250 µm) is unable to keep the transmission at acceptable levels.

Thus, a more complex solution, based on a double step taper, was analyzed. In this approach, the first part of the taper is used to perform the adaptation of the geometry of the waveguide in the sub-wavelength regime, using a smaller period than the one required for the slow-light effect to arise. Then, in the second part, the period is gradually increased until slow-light is reached. This solution is indeed able to limit transmission losses, even with a relatively short taper (between 25 and 100 µm). Suitable optimization of this approach could lead to improved performance, and even solve the problem of light-coupling to the lattice of trenches.

Conclusions

Recent advances in nano-photnics have enabled the development of light manipulation techniques that were unthinkable only a few decades ago. In particular, the silicon industry, relying on all the technology developed for the shaping of matter at the nano-scale, has provided an ideal platform for these new photonic applications, to the point that Silicon Photonics is now a vibrant and rapidly growing field.

The great freedom and the relative high cost of prototyping, typical of such technology, has stimulated the creation of theoretical design strategies, which often involve simulations of the physics underlying such components. The simulation part is nowadays a key component of the design flow if photonics, as it allows for a rapid and cheap exploration of a broad parameters spaces, which would not be feasible in practice.

In this thesis, a theoretical study of grating structures for Silicon Photonics has been performed. Specific targeted application have been grating-couplers for fiber-to-chip (second chapter) and chip-to-chip (third chapter) light coupling, and grating waveguides for slow-light applications (fourth chapter).

In the second chapter, in particular, a theoretical study of fiber-to-chip grating-couplers has been performed, posing special attention to the interplay between coupling efficiency and bandwidth. Through a combination of FDTD and RCWA calculations, the role of the interaction between grating and excitation on the formation of the bandwidth has been analyzed.

Indeed, it has been shown that the bandwidth is made up of two contributions. The first one, of Gaussian shape, comes from the finite dimension of the fiber mode used as excitation, and becomes smaller as the mode dimension increases. The second one comes from the intrinsic width of the photonic mode inside the grating, it has a Lorentzian lineshape and it does not depend on the fiber mode. Confirmation of such interplay comes also

from the fit of the coupling spectra, which start as Gaussian for small fiber mode, then evolve to Voigt and Lorentzian as the mode dimension increases.

In addition, a multi-objective numerical optimization has been employed to apodize the grating-couplers for simultaneous optimization of coupling efficiency and bandwidth, for different dimensions of the fiber mode. It has been shown that, by a combination of apodization and smaller-than-standard excitation spots (reachable using high numerical-aperture or lensed fibers), coupling bandwidth up to 100 nm can be reached with an insertion loss lower than 3 dB.

In the third chapter, a feasibility study of the light coupling between two different chips using a grating-to-grating approach has been presented. The selected chips have been chosen to come from two different platforms, namely conventional Silicon-On-Insulator (SOI) and a III-V, i.e., InP. Due to the low scattering-strength available in the InP platform, gratings longer than the standard 12-15 µm have to be employed, to allow an efficient light extraction and insertion at the InP chip.

Thus, a co-optimization of SOI and InP grating-couplers has been performed through FDTD simulations and a Particle Swarm Optimization algorithm. It has been shown that, by employing 150 µm long gratings with matching scattering-strengths, insertion losses as low as 3 dB are possible.

In the fourth chapter, band-edge slow-light properties of silicon grating waveguides have been analyzed. Taking as figure of merit the slow-light bandwidth, namely the width of the region in which the group index of the waveguide is greater than 10, it has been shown that the slow-light performance can be increased by careful optimization of the geometrical parameters. In particular, an almost tenfold increase (from 1 nm to almost 10 nm) over structures known in the literature is possible by increasing the modulation strength (by making the thin section of the waveguide thinner) and by decreasing the silicon thickness in the cladding region. In terms of slow-light bandwidth, the best performing structure is thus identified in the lattice of trenches.

Then, the problem of light coupling from conventional waveguides is also studied. It is shown that, for conventional silicon thickness in the cladding (150 nm), a simple and compact (≈30 µm) adiabatic taper is enough to get high transmission. However, the same solution does not scale well when the cladding thickness is reduced, since even a quite long (≈250 µm) taper fails to keep the transmission at acceptable values for a thickness of 50 nm. Thus, a more complex solution, based on a double taper with sub-wavelength structures, is proposed. It is shown that this second approach offers a viable

solution to the light-coupling problem, even if some optimization may still be needed.

Further studies are possible on all the analyzed topics. For the part on grating-couplers, refining the optimization procedure, for example by employing the Multi-Objective procedure right from the beginning, could lead to an increase in performances. It is the part on slow-light, however, which offers the greatest appeal. Indeed, the next logical step would be to further improve the sub-wavelength taper for coupling to slow-light, maybe addressing also the lattice of trenches. After that, joining optical and electrical simulations would allow for the design of a slow-light phase shifter, to be employed in slow-light Mach-Zehnder silicon electro-optical modulator.

Appendix A

Coordinate transformation for A-FMM

In this appendix, the formalism leading from the conventional Fourier Modal Method for crossed gratings [182] to the Aperiodic-Fourier Modal Method [183], through the addition of the coordinate transformation, is recalled. First of all, it is important to define the proprieties of this transformation. For the purpose of A-FMM, it is indeed crucial to choose a transformation which is able, by mapping the finite computational cell to the entire $\mathbb{R}^2$, to completely eliminate crosstalk between adjacent replicas of the structure under consideration. For simplicity only transformations involving one coordinate will be addressed, since it is always possible to build the entire 2D transformation by combining two independent 1D ones.

By indicating with x the coordinate in the physical $\mathbb{R}$ space and by x' the coordinate in the computational space (the interval $[-d_x/2, d_x/2]$), the coordinate transformation is uniquely identified by a function:

$$x = f(x') \qquad \left(-\frac{d_x}{2}, \frac{d_x}{2}\right) \to \mathbb{R} \tag{A.1}$$

which is at least C^1 and satisfy the conditions:

$$\lim_{x \to \pm d_x/2} = \pm\infty \tag{A.2}$$

In the following, the formalism leading to the eigenvalue problem of Eq. 1.16 will be discussed, followed by a brief description of the specific functions used for the coordinate transformation.

A.1 The eigenvalue problem

In order to apply the concept of the coordinate transformation to the formalism presented in ref. [182], all that is needed is to write Maxwell equations

in the physical space, then apply the coordinate transformation followed by the Fourier transform in the computational coordinate space. In order to insert the coordinate transform in Maxwell equations it is sufficient to modify the derivative operation along the coordinate which is transformed using the chain rule:

$$\frac{\partial}{\partial x} \rightarrow \frac{\partial x'}{\partial x}\frac{\partial}{\partial x'} \tag{A.3}$$

The function $\frac{\partial x'}{\partial x}$, which will be indicated as $\tilde{f}(x')$, is easily calculated invoking the theorem of the derivative of the inverse function:

$$\tilde{f}(x') = \frac{1}{f'(x')} \tag{A.4}$$

where f' is simply the derivative of f.

In the following, the formalism leading from Maxwell equations to Eq. 1.16 will be recalled. The treatment is, with the necessary modifications, the same as in ref. [182].

In addition, in order to make the dissertation self-contained, the Laurent's rules for the correct Fourier factorization [268] will be reported here. It is indeed known that 1D-periodic functions can be represented an a sum over their Fourier components :

$$f(x) = \sum_n f_n e^{ik_n x} \tag{A.5}$$

where f_n is the Fourier coefficient relative to the vector k_n of the reciprocal lattice. One important notice: since the aim of this theory are numerical calculations, all the summations here proposed are always taken on a finite set. When a continuous function h can be seen as the product of two continuous function f and g, the Fourier coefficients of h can be calculated from the ones of f and g using the standard Laurent's rule:

$$h_n = \sum_m f_{nm} g_m \tag{A.6}$$

where the matrix element f_{nm} is the Fourier coefficient of f relative to the vector $k_n - k_m$. However, when the function h is continuous, but f and g are not — a situation which is often found in electromagnetic problems for D, ε and E — Eq. A.6 is no longer accurate. Indeed, the correct equation to be used — called inverse Laurent rule — becomes:

$$h_n = \sum_m \left[\frac{1}{f}\right]^{-1}_{nm} g_m \tag{A.7}$$

where the matrix $[1/f]^{-1}$ is the inverse of the matrix constructed with the Fourier coefficients of the inverse if f.

Now that all the premises are set, the problem of deriving Eq. 1.16 can be tackled. The starting point is, as usual, the set of Maxwell equations, which can be rewritten:

$$\partial_y E^z - \partial_z E^y = ik_0 H^x \tag{A.8a}$$

$$\partial_z E^x - \partial_x E^z = ik_0 H^y \tag{A.8b}$$

$$\partial_x E^y - \partial_y E^x = ik_0 H^z \tag{A.8c}$$

$$\partial_y H^z - \partial_z H^y = -ik_0 \varepsilon E^x \tag{A.8d}$$

$$\partial_z H^x - \partial_x H^z = -ik_0 \varepsilon E^y \tag{A.8e}$$

$$\partial_x H^y - \partial_y H^x = -ik_0 \varepsilon E^z \tag{A.8f}$$

where $k_0 = \omega/c$ is the vacuum wavevector and nonmagnetic materials are assumed ($\mu = 1$). The components are indicated with a superscript to leave space as subscript for the labeling of the Fourier coefficients. When applying the coordinate transformation, Eqs. A.8 take the form:

$$\tilde{f}_y \partial_y E^z - \partial_z E^y = ik_0 H^x \tag{A.9a}$$

$$\partial_z E^x - \tilde{f}_x \partial_x E^z = ik_0 H^y \tag{A.9b}$$

$$\tilde{f}_x \partial_x E^y - \tilde{f}_y \partial_y E^x = ik_0 H^z \tag{A.9c}$$

$$\tilde{f}_y \partial_y H^z - \partial_z H^y = -ik_0 \varepsilon E^x \tag{A.9d}$$

$$\partial_z H^x - \tilde{f}_x \partial_x H^z = -ik_0 \varepsilon E^y \tag{A.9e}$$

$$\tilde{f}_x \partial_x H^y - \tilde{f}_y \partial_y H^x = -ik_0 \varepsilon E^z. \tag{A.9f}$$

To Fourier transform Eqs. A.9a,A.9b and A.9f the standard Laurent rule can be applied, leading to:

$$\sum_m i \tilde{f}^y_{nm} k^y_m E^z_m - \partial_z E^y_n = ik_0 H^x_n \tag{A.10a}$$

$$\partial_z E^x_n - \sum_m i \tilde{f}^x_{nm} k^x_m E^z_m = ik_0 H^y_n \tag{A.10b}$$

$$\sum_m i \left(\tilde{f}^x_{nm} k^x_m E^y_m - \tilde{f}^y_{nm} k^y_m E^x_m \right) = -ik_0 \sum_j \varepsilon_{nj} E^z_j. \tag{A.10c}$$

Eq A.10c can be inverted by multiplying for ε^{-1}_{ln}/i and summing over n:

$$\sum_n \varepsilon^{-1}_{ln} \left[\sum_m \left(\tilde{f}^x_{nm} k^x_m E^y_m - \tilde{f}^y_{nm} k^y_m E^x_m \right) \right] = -k_0 \sum_{nj} \varepsilon^{-1}_{ln} \varepsilon_{nj} E^z_j, \tag{A.11}$$

which since $\sum_n \varepsilon_{ln}^{-1}\varepsilon_{nj} = \delta_{lj}$ can be rewritten:

$$\sum_{nm} \varepsilon_{ln}^{-1}\left(\tilde{f}_{nm}^{x} k_m^x E_m^y - \tilde{f}_{nm}^{y} k_m^y E_m^x\right) = -k_0 E_l^z. \tag{A.12}$$

When inserted in Eq A.10a and A.10b and after dividing by ik_0, Eq.A.12 gives:

$$-\frac{i}{k_0}\partial_z E_n^y = -H_n^x - \frac{1}{k_0^2}\sum_{mjk} \tilde{f}_{nm}^{y} k_m^y \varepsilon_{mj}^{-1}\left(\tilde{f}_{jk}^{x} k_k^x H_k^y - \tilde{f}_{jk}^{y} k_k^y H_k^x\right) \tag{A.13a}$$

$$-\frac{i}{k_0}\partial_z E_n^x = H_n^y - \frac{1}{k_0^2}\sum_{mjk} \tilde{f}_{nm}^{x} k_m^x \varepsilon_{mj}^{-1}\left(\tilde{f}_{jk}^{x} k_k^x H_k^y - \tilde{f}_{jk}^{y} k_k^y H_k^x\right), \tag{A.13b}$$

which, defining the matrices $K_x(n,m) = k_n^x/k_0\delta_{nm}$ (and the same for K_y), can be recast in matrix form:

$$-\frac{i}{k_0}\frac{\partial}{\partial z}\begin{bmatrix} E_x \\ E_y \end{bmatrix} = \begin{bmatrix} F_x K_x \varepsilon^{-1} F_y K_y & 1 - F_x K_x \varepsilon^{-1} F_x K_x \\ F_y K_y \varepsilon^{-1} F_y K_y - 1 & -F_y K_y \varepsilon^{-1} F_x K_x \end{bmatrix}\begin{bmatrix} H_x \\ H_y \end{bmatrix}, \tag{A.14}$$

and thus Eq. 1.16a is demonstrated.

The difficulties arise when trying to demonstrate Eq. 1.16b, since it can involve discontinuous functions with concurrent jumps. To better clarify this part, a little change in notation has to be introduced. In all the previous treatment the Fourier transform was always made in both x and y directions at the same time. Since this is not true anymore for the following discussion, the summation index n indicating the different components of the Fourier expansion will be split in two indexes: a normal n indicating Fourier transformation along x and a primed index n' indicating transformation along y. Every summation involving the entire Fourier space will now be expressed by two indexes, for example:

$$\sum_{m} \tilde{f}_{nm}^{x} k_m^x E_m^y \rightarrow \sum_{mm'} \tilde{f}_{nn'mm'}^{x} k_{mm'}^x E_{mm'}^y. \tag{A.15}$$

When only the normal or primed index is present, the Fourier transform is intended only along the specified axis.

With this new notation, the Fourier transform of Eq A.9c, which can be performed with the standard Laurent rule without particular problems, takes the form:

$$\sum_{mm'} i\left(\tilde{f}_{nn'mm'}^{x} k_{mm'}^x E_{mm'}^y - \tilde{f}_{nn'mm'}^{y} k_{mm'}^y E_{mm'}^x\right) = ik_0 H_{nn'}^z. \tag{A.16}$$

To correctly Fourier transform Eq. A.9d and A.9e, it is necessary to use the inverse Laurent rule [268]. Focusing firstly on A.9d it is important to note that the product εE_x is continuous is x, and can thus be transformed in this coordinate as follows:

$$\sum_m i\tilde{f}^x_{nm}k^x_m H^z_m - \partial_z H^y_m = -ik_0 \sum_j \left[\frac{1}{\varepsilon}\right]^{-1}_{nj} E^x_j, \tag{A.17}$$

where everything in this equation is still an explicit function of y. However, since E^x_j is continuous in y for every j, the Fourier transform along this axis can be performed with the conventional Laurent rule, leading to:

$$\sum_{mm'} i\tilde{f}^y_{nn'mm'}k^y_{mm'}H^z_{mm'} - \partial H^y_{nn'} = ik_0 \sum_{jj'} \left[\frac{1}{\varepsilon}\right]^{-1}_{nj,n'j'} E^x_{jj'}, \tag{A.18}$$

which, by multiplying for i/k_0 and substituting H^z form A.9c, can be written as:

$$\begin{aligned} -\frac{i}{k_0}H^y_{nn'} = \sum_{jj'} \left[\frac{1}{\varepsilon}\right]^{-1}_{nj,n'j'} E^x_{jj'} + \\ +\frac{1}{k_0^2}\sum_{mm'll'} \tilde{f}^y_{nn'mm'}k^y_{mm'}\left(\tilde{f}^x_{mm'll'}k^x_{ll'}E^y_{ll'} - \tilde{f}^y_{mm'll'}k^y_{ll'}E^x_{ll'}\right). \end{aligned} \tag{A.19}$$

The same procedure can be followed for Eq. A.9e, with the difference that the Fourier transformation with the inverse rule has to be taken along y:

$$\partial_z H^x_{n'} - \sum_{m'} i\tilde{f}^x_{n'm'}k^x_{m'}H^z_{m'} = -ik_0 \sum_{j'} \left[\frac{1}{\varepsilon}\right]^{-1}_{n'j'} E^y_{j'} \tag{A.20}$$

and then with the conventional rule along x

$$\partial_z H^x_{nn'} - \sum_{mm'} i\tilde{f}^x_{nn'mm'}k^x_{mm'}H^z_{mm'} = -ik_0 \sum_{jj'} \left[\frac{1}{\varepsilon}\right]^{-1}_{n'j',nj} E^y_{jj'}. \tag{A.21}$$

This leads, after multiplication for $-i/k_0$ and substitution of H^z, to:

$$\begin{aligned} -\frac{i}{k_0}H^x_{nn'} = -\sum_{jj'} \left[\frac{1}{\varepsilon}\right]^{-1}_{n'j',nj} E^y_{jj'} + \\ +\frac{1}{k_0^2}\sum_{mm'll'} \tilde{f}^x_{nn'mm'}k^x_{mm'}\left(\tilde{f}^x_{mm'll'}k^x_{ll'}E^y_{ll'} - \tilde{f}^y_{mm'll'}k^y_{ll'}E^x_{ll'}\right). \end{aligned} \tag{A.22}$$

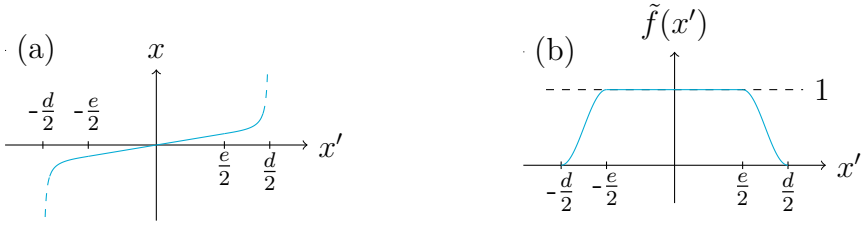

Figure A.1: Representation of (a) the real coordinate transformation and (b) corresponding $\tilde{f}$ function.

A little simplification in the notation at this point is useful. Since Eqs. A.19 and A.22 only involve summation over coupled primed and unprimed indexes, it is possible to go back to the notation with only one subscript ($nn' \to n$), which allows the simple definition of the matrices:

$$\varepsilon_{x,y}(n,m) = \left[\frac{1}{\varepsilon}\right]^{-1}_{nm,n'm'} \qquad \varepsilon_{y,x}(n,m) = \left[\frac{1}{\varepsilon}\right]^{-1}_{n'm',nm}. \tag{A.23}$$

With these simplification Eq.s A.19 and A.22 can be cast in simple matrix form:

$$-\frac{i}{k_0}\partial_z \begin{bmatrix} H_x \\ H_y \end{bmatrix} = \begin{bmatrix} -F_x K_x F_y K_y & (F_x K_x)^2 - \varepsilon_{y,x} \\ \varepsilon_{x,y} - (F_y K_y)^2 & F_x K_x F_y K_y \end{bmatrix} = \begin{bmatrix} E_x \\ E_y \end{bmatrix}, \tag{A.24}$$

which is the same as Eq. 1.16b. Together with Eq. A.14, this equation forms the base of the eigenvalue problem to be solved in each layer.

A.2 Function for coordinate transformation

The first function proposed for the coordinate transformation is a purely real one — see Fig. A.1 — which is defined as follow:

$$f(x') = \begin{cases} x' & \text{for } |x'| < e/2 \\ \frac{x'}{|x'|}\left[\frac{e}{2} + \frac{d-e}{\pi}\tan\left(\pi\frac{|x'|-e/2}{d-e}\right)\right] & \text{for } e/2 < |x'| < d/2 \end{cases} \tag{A.25}$$

where d, e are the widths of the computational cell and of the unmapped region, respectively.

Its role is just to eliminate crosstalk between adjacent replicas of the structure, allowing for the treatment of isolated structures in space. This kind of transformation does not implement the outgoing wave condition at the border of the computational cell, so it is suitable for calculation only when scattering in the xy plane is negligible.

The Fourier coefficient of the function $\tilde{f}$ needed for the implementation can be calculated as:

$$\tilde{f}_n = \delta_{0n} - (-1)^n \frac{q}{2d}\left[\mathrm{sinc}\left(\frac{nq}{d}\right) + \frac{1}{2}\mathrm{sinc}\left(\frac{nq}{d} - 1\right) + \frac{1}{2}\mathrm{sinc}\left(\frac{nq}{d} + 1\right)\right], \tag{A.26}$$

where $q = d - e$ is the width of the mapped portion of the computational cell.

In order to allow the treatment of all the situations in which the scattering is important, a different function has been proposed [269]. The idea behind this new transformation is to map the computational cell to a complex plane. By suitable choice of this complex mapping, it is possible to obtain a behavior similar to a Perfectly Matched Layer (PML) boundary condition at the border of the computational cell. In this way all waves propagating towards infinity are absorbed in the region of PML, the radiation modes can be expanded on Fourier basis inside the computational cell, thus allowing for the correct handling of the out-of-cell scattering.

A particularly simple function which provide adsorbing boundary condition, and that can be though as an extension of Eq. A.25 is the following:

$$f(x') = x' \qquad \text{for } |x'| < e/2 \tag{A.27a}$$

$$f(x) = \frac{x'}{|x'|}\left(\frac{e}{2} + \frac{d-e}{\pi(1-\gamma)}\left\{\tan\left(\pi\frac{|x'| - e/2}{d-e}\right) - \right.\right.$$
$$\left.\left. - \frac{\gamma}{\sqrt{1-\gamma}}\mathrm{atan}\left[\sqrt{1-\gamma}\tan\left(\pi\frac{|x'| - e/2}{d-e}\right)\right]\right\}\right) \qquad \text{for } e/2 < |x'| < d/2 \tag{A.27b}$$

which leads to a $\tilde{f}$ expressed by the fourier coefficients:

$$\tilde{f}_n = \delta_n - \frac{q}{2d}(-1)^n\left[\left(1 + \frac{\gamma}{4}\right)\mathrm{sinc}\left(\frac{nq}{d}\right) + \frac{1}{2}\mathrm{sinc}\left(\frac{nq}{d} - 1\right) + \right.$$
$$\left. + \frac{1}{2}\mathrm{sinc}\left(\frac{nq}{d} + 1\right) - \frac{\gamma}{8}\mathrm{sinc}\left(\frac{nq}{d} - 2\right) - \frac{\gamma}{8}\mathrm{sinc}\left(\frac{nq}{d} + 2\right)\right] \tag{A.28}$$

where e, q and d have the same meaning of the real coordinate transformation and γ is a complex parameter which is assumed equal to $1/(1-i)$.

Appendix B

Poynting vector in A-FMM

A useful feature of A-FMM is the possibility to calculate the z component of the Poyting vector. This is crucial for correct calculation of both reflectance and transmittance, and of the energy flow inside the structure under arbitrary excitation. The starting point for the calculation is the definition of the time-averaged Poyting vector for harmonic fields:

$$\mathbf{P}(\mathbf{x}) = \frac{1}{2}\mathbf{E}(\mathbf{x}) \times \mathbf{H}^*(\mathbf{x}) \tag{B.1}$$

where all the space dependence is indicated in $\mathbf{x} = (x, y, z)$. The flux of the real part of this vector over a surface represents the total energy flux across that surface, averaged over one period of oscillation of the radiation. The imaginary part of the Poyting vector can be related to stored power, and it is present only in certain cases (standing waves, resonators, etc...). It will be ignored in the present discussion, which only deals with the energy flux.

For the purpose of A-FMM, only the z component to the Poynting vector is needed. It can be calculated as:

$$P_z(\mathbf{x}) = \frac{1}{2}\left[E_x(\mathbf{x})H_y^*(\mathbf{x}) - E_y(\mathbf{x})H_x^*(\mathbf{x})\right] \tag{B.2}$$

and can be used to calculate the total energy flux through the computational cell at position z:

$$\Phi(z) = \int_C P_z(x, y, z)d\Omega \tag{B.3}$$

where C indicates the domain of the xy computational cell, and $d\Omega = dxdy$.

This flux can assume two different forms, whether only the flux related to a single mode or the total energy flow is calculated.

B.1 Energy flux of a single mode

The energy related to a single mode is of paramount importance for the correct calculation of the transmittance and reflectance. Although the coupling coefficients between incoming and outgoing modes are given by the square modulus of the elements of the scattering matrix, to get the right fraction of energy coupled from one mode to another it is necessary to take into account, in addition to the coupling coefficient, also the total power carried by each mode — see 1.25.

To calculate this quantity the field in Eq. B.3 will be assumed to come from only one mode (whose coefficient is assumed to be 1). The first term under the integral sign thus becomes:

$$E_x(\mathbf{x})H_y^*(\mathbf{x}) = \sum_{kk'} \tilde{E}_x(n,k)\tilde{H}_y^*(n,k')e^{i[(k_x-k'_x)x+(k_y-k'_y)y]}, \tag{B.4}$$

where n is the mode of which the Poyting vector is calculated. This equation, granted that:

$$\int_C e^{i[(k_x-k'_x)x+(k_y-k'_y)y]}d\Omega = L_xL_y\delta_{kk'} \tag{B.5}$$

since k and k' are reciprocal lattice vectors, can be integrated into:

$$\int_C E_x(\mathbf{x})H_y^*(\mathbf{x})d\Omega = L_xL_y\sum_k \tilde{E}_x(n,k)\tilde{H}_y^*(n,k) \tag{B.6}$$

and an analogous expression for the second term.

Consequently, the total energy flux $\mathcal{P}$ associated with a single mode can be expressed as:

$$\mathcal{P} = \frac{L_xL_y}{2}\sum_k \tilde{E}_x(n,k)\tilde{H}_y^*(n,k) - \tilde{E}_y(n,k)\tilde{H}_x^*(n,k), \tag{B.7}$$

whose real part is, apart from the normalization factor (which is unimportant, since only ratios are considered), equivalent to Eq. 1.26.

B.2 Total energy flux

The calculation of the total energy flux inside the structure as a function of z under arbitrary excitation is a little more complex. It is however a desirable feature, since it can be employed to calculate the total energy balance of the structure and the absorption layer by layer.

In order to calculate the energy flux, the expression of the fields as a function of z is needed. Both electric and magnetic fields are indeed composed by a full superposition of all forward and backward propagating modes:

$$E = \sum_{n,k} (u_n + d_n)\tilde{E}(n,k)e^{i(k_x x + k_y y)} \tag{B.8a}$$

$$H = \sum_{n,k} (u_n - d_n)\tilde{H}(n,k)e^{i(k_x x + k_y y)}. \tag{B.8b}$$

The total z-component of the Poynting vector is still expressed by Eq. B.1. In the following only the term involving E_x and H_y will be expanded, since the other term, containing E_y and H_x is fully analogous. Thus, expanding using Eq. B.8, it is possible to write:

$$E_x(\mathbf{x})H_y^*(\mathbf{x}) = \sum_{nn',kk'} (u_n + d_n)(u_{n'} - d_{n'})^* \tilde{E}_x(n,k)\tilde{H}_y^*(n',k')e^{i[(k_x - k'_x)x + (k_y - k'_y)y]}. \tag{B.9}$$

Then, by remembering Eq. B.5, it is possible to integrate over the cross section, thus obtaining:

$$\int_C E_x(\mathbf{x})H_y^*(\mathbf{x})d\Omega = L_x L_y \sum_{nn',k} (u_n + d_n)(u_{n'} - d_{n'})^* \tilde{E}_x(n,k)\tilde{H}_y^*(n',k). \tag{B.10}$$

At this point, once written the analogous of Eq. B.10 for the second term in Eq. B.1, it is possible to write a general expression for z-component of the Poyting vector as:

$$\mathcal{P}_z = \frac{1}{2} Re\left[\sum_{nn'} (u_n + d_n)(u_{n'} - d_{n'})^* \tilde{\mathcal{P}}_{nn'}\right], \tag{B.11}$$

which is the same expression as Eq. 1.28, provided that:

$$\tilde{\mathcal{P}}_{nn'} = \sum_k \left[\tilde{E}_x(k,n)\tilde{H}_y^*(k,n') - \tilde{E}_y(k,n)\tilde{H}_x^*(k,n')\right] \tag{B.12}$$

Appendix C

Particle Swarm Optimization

Optimization algorithms are employed almost everywhere in current design problems. Normally, such problems have to be formulated in terms of a fitness function, namely a function, dependent on some optimization parameters, which is able to assign a number to the validity of a particular solution, identified by a specific combination of parameters. Thus, finding the optimal solution is usually equivalent to find the maximum or minimum of the corresponding fitness function.

Particle Swarm Optimization (PSO) is one exponent of the class of heuristic optimization algorithms [270, 271]. The denomination "heuristic" is assigned to those optimization algorithms which, although no guarantee of convergence to the optimal solution is provided, are usually able to find an approximate optimal solution in less time than classical optimization algorithms.

Usually this kind of algorithms takes inspiration from the natural world. Major exponents of this class are Genetic Algorithms (GA) [272], Tabu Search (TS) [273], Simulated Annealing (SA) [274], Ant Colony Optimization (ACO) [275] and the PSO itself.

The PSO algorithm had been first proposed in 1995 by R. Eberhart and J. Kennedy [218], taking inspiration from the behavior of a swarm of bees in search of the point of highest flower-density in a field. Since then, PSO has stimulated a great deal of research, either applying the standard method to different optimizations, focusing on a better understanding of the method, or generalizing the method to extend its domain of application.

PSO algorithms have been successfully applied to many problems. Particularly relevant for this thesis are electromagnetic problems, such as grating couplers [208], horn antennas [276], antennas arrays [277] and absorbers [278].

Standard particle swarm optimization is only able to deal with real val-

ued parameters and one single fitness function. Many extensions have been proposed over the years, such as binary valued PSO [279, 280] and multi-objective PSO [281, 282].

In this appendix the standard PSO algorithm will be recalled, together with its Pareto-front based Multi-Objective implementation used in Chapter 2.

C.1 Standard Single-Objective PSO

Standard single objective Particle Swarm Optimization deals with the maximization (or minimization) of a single multi parameter function $f : A \to \mathbb{R}$ where A is usually a certain closed subspace of $\mathbb{R}^n$. In real life problems the subspace A is the space of parameters available for the optimization and the function f is the "fitness function", a real valued function expressing the goodness of a solution.

At the core of the PSO is the concept of swarm, which is simply a collection of agents with some shared information between them. Each agent has a position $\mathbf{x}$ (representing a single trial solution) in the space A and it is able to move in it with velocity $\mathbf{v}$. The optimization is then carried out by an iterative procedure which at each iteration evaluates the fitness function in the position of each agent, then moves the agents taking into account the accumulated knowledge of the parameter space.

This knowledge consists basically in two positions for each agent: the personal best $\mathbf{p}_b$ and the global best $\mathbf{g}_b$. The personal best is different for each agent and stores the position with the maximum fitness function ever found by that particular agent. The global best stores the position of maximum fitness function ever found by the entire swarm, and it is basically the only mean of communication between the agents.

The algorithm for updating the positions of the agents is a sort of fictitious dynamics in which each agent is dragged towards his $\mathbf{p}_b$ and $\mathbf{g}_b$ using a kind of harmonic potential with random strength:

$$\mathbf{v}^i_{(t+1)} = w\mathbf{v}^i_{(t)} + c_c\alpha_c(\mathbf{p}^i_b - \mathbf{x}^i_{(t)}) + c_s\alpha_s(\mathbf{g}^i_b - \mathbf{x}^i_{(t)}) \tag{C.1a}$$

$$\mathbf{x}^i_{(t+1)} = \mathbf{x}^i_{(t)} + \mathbf{v}^i_{(t+1)}. \tag{C.1b}$$

In these equations, w, c_c and c_c are coefficients which can be tweaked to balance the optimization, while α_c and α_s are random numbers extracted, at each iteration step, from a uniform distribution between 0 and 1. The coefficients c_c and c_s are usually numbers between 1.0 and 2.0 called cognitive and social rates, respectively, and regulate the relative strengths of the $\mathbf{p}_b$

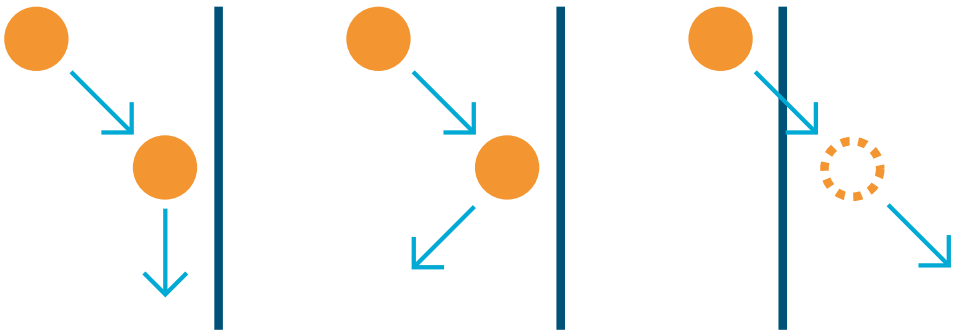

(a) Adsorbing. (b) Reflecting. (c) Invisible.

Figure C.1: Different type of boundary conditions for PSO.

and $\mathbf{g}_b$ pulls. The other coefficient, w, is called inertial weight, it is usually between 0.1 and 0.9 and regulates how resilient the agents are to the $\mathbf{p}_b$ and $\mathbf{g}_b$ pulls. It is furthermore usual practice to set a maximum speed of the agents in each direction, in order to prevent the agents from traveling the full length of the allowed space in one single iteration.

The tweaking of these coefficients can greatly impact the performance of the algorithm, in particular by changing the balance between exploration, the tendency to explore unknown territories of the parameter space, and exploitation, the tendency to focus on local optima to better identify the best local position. The balance is delicate: too much exploration could lead to the missing of the fine features of the fitness function landscape, while too much exploitation could cause the algorithm to remain stuck in a local optimum, missing the more interesting global one. In general, high w and c_s tends to favor exploration, while high c_c favors exploitation.

Studies exists in literature which address this problem [283], and different strategies to improve convergence have been proposed. One simple and effective strategy is to adjust the value of the inertial weight during the optimization: a high w is chosen at the beginning of the algorithm, thus favoring exploration, then the inertial wight is gradually reduced, moving the balance in favor of exploitation.

Typical PSO algorithms are usually run with a few agents (up to a few tens) for a fixed number of iteration, then the value of $\mathbf{g}_b$ is taken as the result of the optimization. The optimization can however be stopped before if all the agents have converged in the same position, a situation in which no further improvement can be expected.

Beyond the fundamental core of the algorithm, in the PSO a way has

to be found to keep the agents in the region of parameters relevant to the problem, so boundary conditions have to be implemented. Three main kinds of boundary conditions — see Fig. C.1 — exist: absorbing, reflecting and invisible. In the absorbing and reflecting boundary condition the agent is not allowed to leave the investigation domain. When an agent hits a boundary in one direction, it is immediately retaken inside, while his velocity component perpendicular to the boundary is either set to 0 (absorbing) or flip in sign (reflecting). On the contrary, in the invisible boundary conditions, the agent is free to move outside the investigation domain, but the fitness function is not evaluated, and consequently $\mathbf{p}_b$ not updated, until the agent returns to the domain.

C.2 Pareto Front Multi-Objective PSO

Extending standard optimization, Multi-Objective (MO) optimization can handle problems in which more than one fitness function, often negatively correlated, are considered. The extension of optimization procedures to multi-objective problems is not a straightforward one, since key concepts of optimization, such as the existence of a unique best solution, are lost and the very notion of "better" has to be redefined.

A way to solve these problems is to recur to the concept of *Pareto dominance* and *Pareto Front*. The concept of Pareto dominance substitutes the concept of "better." By definition, when dealing with a set of fitness functions f_j, a solution $\mathbf{x}$ is said to dominate over a solution $\mathbf{y}$ if:

$$f_j(\mathbf{x}) \geq f_j(\mathbf{y}) \forall j \text{ and } \exists i : f_i(\mathbf{x}) > f_i(\mathbf{y}) \tag{C.2}$$

If, chosen two solution $\mathbf{x}$ and $\mathbf{y}$, neither of them dominates the other, it is impossible to identify a better one between the two. In fact, they simply express different trade-offs between the fitness functions. In this framework, the single optimal solution of standard optimization is substituted with the ensemble of solutions that are no worse than any other, or more precisely that are non-dominated. This collection is called a *Pareto front*. It is important to notice that the knowledge of the complete Pareto front of an optimization problem defines the boundary of the problem and gives complete information about every possible trade-off.

Multi-Objective optimizations algorithms that derive from iterative single-objective procedures, such as MO-PSO, usually keep an archive of some of the un-dominated solution found and update them at every iteration. In this thesis the MO-PSO devised by Tripathi *et al.* [281] is used, and it will be briefly illustrated here.

Indeed, three main changes to the standard PSO algorithm are made: the choice of the coefficients, the updating of $\mathbf{p}_b$, and the archive in place of $\mathbf{g}_b$. The updating of $\mathbf{p}_b$ is the most straightforward: at the beginning of the algorithm $\mathbf{p}_b$ is set as the starting position for each agent, then it is updated only if the new position dominates over the old $\mathbf{p}_b$. The choice of the coefficient of eq. C.1a is peculiar. Instead of selecting fixed coefficients or even a fixed strategy, each agent has his own set of coefficients which is updated with the PSO algorithm itself. The idea is that in this way the coefficients should converge to the most effective ones for the particular problem under examination. The most profound change, however, is the introduction of an external archive in place of the $\mathbf{g}_b$. At each iteration, in fact, a temporary archive of the non dominated solutions is generated. To prevent the archive to become excessively long the solutions in the archive are ranked in decreasing order with respect to the d function:

$$d(\mathbf{x}_i) = \min_{j \neq i} \left[\sum_m |f_m(\mathbf{x}_f) - f_m(\mathbf{x}_i)| \right] \tag{C.3}$$

where i, j run over the solutions in the temporary archive and m over the fitness functions. This d function measure the distance of each solution from his nearest neighbour. Then at each iteration only a maximum number of solutions is retained. Keeping the solutions with highest d value ensures the maximum variety possible in the temporary archive. The value of $\mathbf{g}_b$ for the evolution in eq. C.1a is then randomized at each iteration from the archive using roulette wheel selection over the function d. Given enough iterations the temporary archive should converge to the true Pareto front, thus providing the complete solution to the optimization problem.

Appendix D

Details on grating-couplers CE and BW optimization

In this appendix, details on the procedure for the simultaneous optimization of coupling efficiency and bandwidth of grating-couplers are reported. However, a little disclaimer is needed: due to a series of unfortunate events (a mixture of failing hard drives and hacker attacks) all intermediate data regarding the optimizations in chapter 2, which led to the publication of the APL paper [219], have been lost. Thus, to better clarify the procedure and illustrate also the intermediate steps, the calculations have been redone for the MFD=8 µm case, and the results are now reported here.

The optimization procedure is divided in three parts, each containing a single PSO run with different aims:

1. A single-objective optimization aimed at finding the linearly chirped design showing maximum CE.
2. Starting from the results of the previous point, a single objective optimization aimed at finding the apodized grating showing maximum CE.
3. Including the knowledge obtained at the previous step, the multi-objective optimization treating simultaneously CE and bandwidth.

In the following, all three steps will be discussed.

D.1 Linear chirp Max CE

The first step in the procedure is to find the linearly chirped grating providing the maximum coupling efficiency possible. To do this, a standard

Parameter	Unit	Min.	Max	Max Speed	Optimal Value
Etch	nm	0	220	50	110
DC_0	%	10	70	30	10
DC_{Max}	%	40	80	20	50
L_{chirp}	µm	0.5	10	3	9.2
Tbox	µm	1.5	2.5	0.5	2.01
FIB	µm	2.0	10.0	4.0	4.71

Table D.1: Parameters of the SO-PSO for the linearly chirped grating. Both definition of the search space and results of the optimization are reported.

single-objective PSO is employed. Taking Fig. 2.2 as reference, the only fixed parameter of the structure is the thickness of the waveguide **Twave**, chosen to be the standard of 220 nm. The indexes of the materials are assumed constant, namely 3.44 and 1.44 for Si and SiO_2, respectively. The fiber mode is modeled as a Gaussian source with a MFD of 8 µm placed 2 µm above the waveguide, inside the top cladding. This assumes that the fiber is joined to the chip using an epoxy featuring the same refractive index of the oxide, thus eliminating the problem of reflection at the chip interface. The angle of incidence θ is fixed at 10°.

The variable parameters, which are subjected to the optimization, are a total of six. Still taking Fig. 2.2 as reference, they are: the etching depth **Etch**, the starting duty cycle $\mathbf{DC}_0$, the maximum duty cycle $\mathbf{DC}_{max}$, the chirp length $\mathbf{L}_{chirp}$, the thickness of the bottom oxide **Tbox**, and the distance of the center of the fiber from the starting of the grating **FIB**. The exact values defining the boundary of the search space for each parameter are reported in Tab. D.1.

The period **P** is kept constant along the grating, and it is tuned for each structure in such a way to keep the wavelength of maximum coupling inside a 10 nm window centered around λ=1.55 µm. The duty cycle is instead varied along the grating, following:

$$DC(x) = \begin{cases} DC_0 + x(DC_{max} - DC_0)/L_{chirp} & \text{for } x < L_{chirp} \\ DC_{max} & \text{for } x > L_{chirp} \end{cases} \tag{D.1}$$

The standard single-objective PSO algorithm is run for 150 iterations using 10 agents. The full procedure takes a few hours on a standard quad-core desktop workstation. Some of the data regarding the evolution of the swarm throughout the algorithm are presented in Fig. D.1. At the end of the optimization it is found that 8 out of 10 agents have converged to the same solution (behaving as agent 1 in Fig. D.1b), while 2 have not (they behave

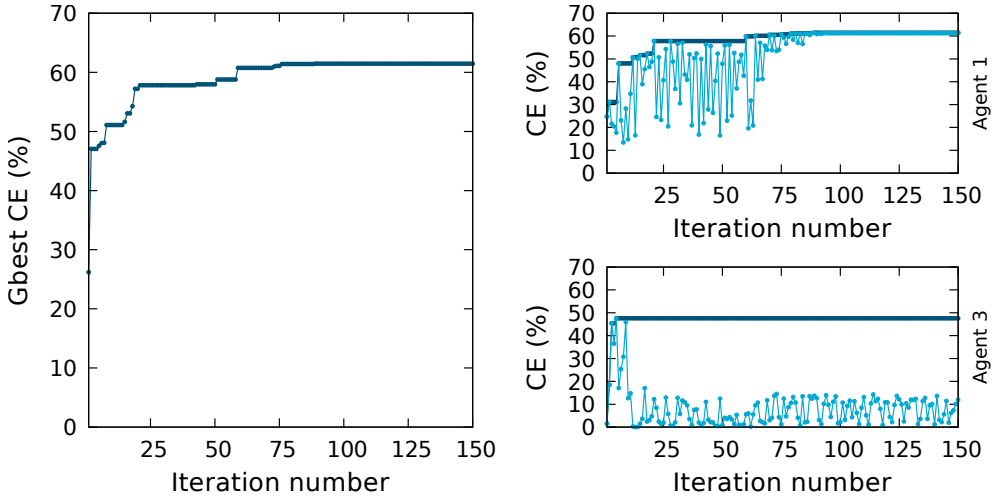

(a) Gbest fitness. (b) Pbest fitness and fitness.

Figure D.1: Evolution of some of the data during the swarm. (a) CE of the temporary global maximum. (b) CE of the Pbest solution (dark blue) and of actual position (light blue) of some of the agent in the swarm.

as agent 3). However, in such convergence state it is unlikable that a second run could result in better performance, thus the parameters stored as the global best — see Tab. D.1 — are taken as the result of the optimization, and the procedure is carried on to the next step.

D.2 Apodized Max CE

The aim of the second PSO is to maximize the coupling efficiency even further, by applying a full apodization. Indeed, the positions and the widths of each groove in the grating are now optimized as independent variables. All the others parameters (Etch, Tbox,FIB) are kept fixed to the values obtained at the previous step. By indicating with P the period of the optimized linearly chirped design (623 nm in this case), the parameters' search space is such defined: the position of each groove can vary in a P/2 wide window centered at the position of the groove of a uniform grating of period P, with a maximum speed of P/4; the width of each groove can vary between 50 nm (set as the minimum feature size) and P/2, with a maximum speed of P/5. One of the agents is set to start in the position which correspond to the linearly chirped configuration found in the previous step, while the positions of the others are randomly generated.

In contrast to the previous section, no active tuning is applied to the

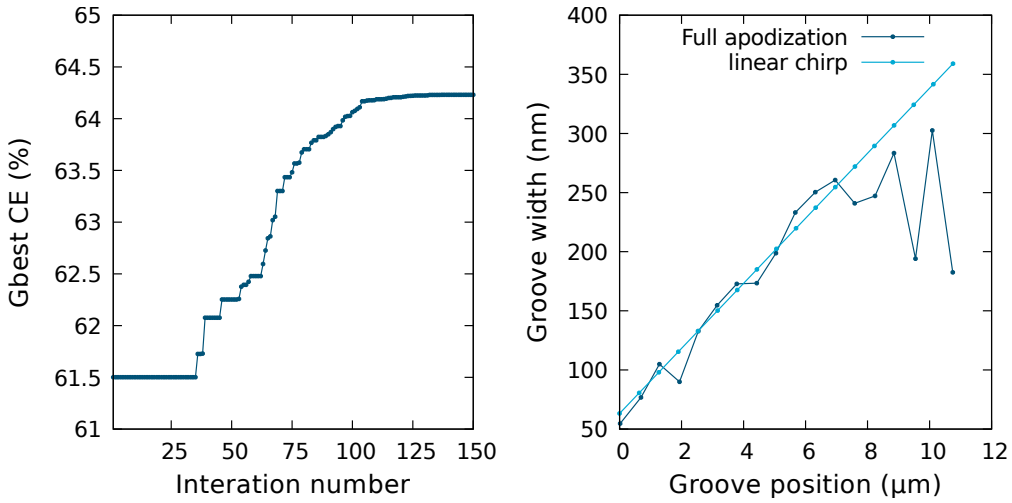

(a) Evolution of Gbest fitness.

(b) Parameter of optimal structure.

Figure D.2: Data regarding the PSO run for the apodized grating for best coupling efficiency.

grating in order to keep the maximum transmission locked at λ=1.55 µm. It is assumed that the search space is small enough to prevent significant deviations of the coupling wavelength.

The aim of this part is only to refine the optimization done at the previous step, and only a marginal improvement can be expected. In fact, as can be seen from Fig. D.2a, an improvement in Coupling Efficiency of about 3% from the linearly chirped design can be obtained by a full numerical apodization.

To be fair, this step of the optimization would not be needed in theory, since it would be covered by the multi-objective optimization of the next step. However, it is reasonable to expect the convergence of the multi-objective optimization to be quite critical for the very edge of the Pareto front, where the solution with maximum CE is located. Thus, it has been chosen to optimize for maximum CE using a dedicated optimization and then include such knowledge as a starting point in the Multi-Objective PSO, in order to improve convergence in the high-CE region.

D.3 Apodized CE and BW

In this section the true multi-objective optimization is presented. The definition of the search space is absolutely the same as the previous step. To ensure a good convergence at the high-CE edge of the Pareto front, knowledge of the maximum-CE apodized solution in included as a starting point of one

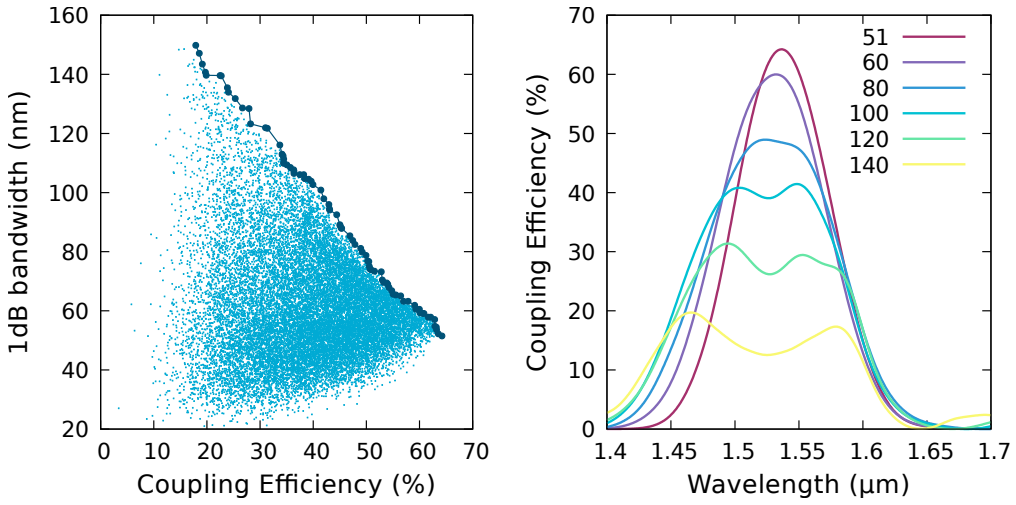

(a) Pareto front. In light blue, performance of all the structure analyzed.

(b) Spectra of some of the structured on the Pareto front. Bandwidth in label.

Figure D.3: Some data about the MO-PSO for simultaneous optimization of Coupling Efficiency and Bandwidth.

of the agents. The starting positions of all the other agents are randomly chosen.

Due to its greater complexity, the MO-PSO algorithm is run for a much longer time, namely for 1000 iterations and using 20 agents, thus exploring a total of 20K configurations. In physical time, this translate into a couple of days on a standard quad-core desktop workstation.

The result of the optimization is reported in Fig. D.3a, where the new Pareto front for the MFD=8 µm is plotted. Bandwidth and coupling efficiency of every structure analyzed during the optimization are also reported, to help the reader visualize the Pareto front as a true boundary to the reachable performances, and thus the expression of the ultimate trade-off. Some examples of this trade-off are reported in Fig. D.3b, where the spectra of selected structures along the front, corresponding to target bandwidths, are shown. It is evident the capability of this design process to find solutions showing enhanced bandwidth and an almost flat spectrum across the bandwidth of interest.

It is worth remarking that the new Pareto front is a little different from the one presented in the main text. This is indeed expected, since the very nature of the PSO is not fully deterministic and could lead to slightly different results. Overall, the new Pareto front is broader, featuring solutions up to a bandwidth of 150 nm, and it is in general a little better, showing an average

of 1-2% higher coupling efficiency for the same bandwidth. However, the trend and also the values are quite close, so the two results can be considered quite in agreement with each other.

Bibliography

[1] S. E. Miller, "Integrated optics: An introduction," *Bell System Technical Journal*, vol. 48, no. 7, pp. 2059–2069, 1969.

[2] R. Soref and J. Larenzo, "All-silicon active and passive guided-wave components for λ= 1.3 and 1.6 μm," *IEEE Journal of Quantum Electronics*, vol. 22, no. 6, pp. 873–879, 1986.

[3] R. Soref and J. Lorenzo, "Single-crystal silicon: a new material for 1.3 and 1.6 μm integrated-optical components," *Electronics Letters*, vol. 21, no. 21, pp. 953–954, 1985.

[4] F. Namavar, E. Cortesi, R. Soref, and P. Sioshansi, "On the formation of thick and multiple layer simox structures and their applications," *MRS Online Proceedings Library Archive*, vol. 147, 1989.

[5] B. Weiss, G. Reed, S. Toh, R. Soref, and F. Namavar, "Optical waveguides in simox structures," *IEEE Photonics Technology Letters*, vol. 3, no. 1, pp. 19–21, 1991.

[6] A. Rickman, G. Reed, B. Weiss, and F. Namavar, "Low-loss planar optical waveguides fabricated in simox material," *IEEE Photonics Technology Letters*, vol. 4, no. 6, pp. 633–635, 1992.

[7] J. Schmidtchen, A. Splett, B. Schuppert, and K. Petermann, "Low loss integrated-optical rib-waveguides in soi," in *SOI Conference, 1991. Proceedings, 1991., IEEE International*, pp. 142–143, IEEE, 1991.

[8] K. Petermann, "Properties of optical rib-guides with large cross-section," *AEU-International Journal ot Electronics and Communications*, vol. 30, no. 3, pp. 139–140, 1976.

[9] R. A. Soref, J. Schmidtchen, and K. Petermann, "Large single-mode rib waveguides in gesi-si and si-on-sio/sub 2," *IEEE Journal of Quantum Electronics*, vol. 27, no. 8, pp. 1971–1974, 1991.

[10] A. Rickman and G. Reed, "Silicon-on-insulator optical rib waveguides: loss, mode characteristics, bends and y-junctions," *IEE Proceedings-Optoelectronics*, vol. 141, no. 6, pp. 391–393, 1994.

[11] R. Soref and B. Bennett, "Electrooptical effects in silicon," *IEEE Journal of Quantum Electronics*, vol. 23, no. 1, pp. 123–129, 1987.

[12] R. A. Soref and B. R. Bennett, "Kramers-kronig analysis of electro-optical switching in silicon," in *Integrated Optical Circuit Engineering IV*, vol. 704, pp. 32–38, International Society for Optics and Photonics, 1987.

[13] G. Treyz, P. May, and J.-M. Halbout, "Silicon mach–zehnder waveguide interferometers based on the plasma dispersion effect," *Applied Physics Letters*, vol. 59, no. 7, pp. 771–773, 1991.

[14] G. Treyz, "Silicon mach-zehnder waveguide interferometers operating at 1.3 mu m," *Electronics Letters*, vol. 27, no. 2, pp. 118–120, 1991.

[15] A. Liu, R. Jones, L. Liao, D. Samara-Rubio, D. Rubin, O. Cohen, R. Nicolaescu, and M. Paniccia, "A high-speed silicon optical modulator based on a metal–oxide–semiconductor capacitor," *Nature*, vol. 427, no. 6975, p. 615, 2004.

[16] S. Luryi, A. Kastalsky, and J. C. Bean, "New infrared detector on a silicon chip," *IEEE Transactions on Electron Devices*, vol. 31, no. 9, pp. 1135–1139, 1984.

[17] A. Kastalsky, S. Luryi, J. Bean, and T. Sheng, "Single-crystal ge/si infrared photodetector for fiber-optics communications," in *Proc. 1st Int. Symp. Silicon MBE*, p. 406, 1985.

[18] S. Luryi, T. Pearsall, H. Temkin, and J. Bean, "Waveguide infrared photodetectors on a silicon chip," *IEEE Electron Device Letters*, vol. 7, no. 2, pp. 104–107, 1986.

[19] H. Temkin, T. Pearsall, J. Bean, R. Logan, and S. Luryi, "Ge x si1-x strained-layer superlattice waveguide photodetectors operating near 1.3 μm," *Applied Physics Letters*, vol. 48, no. 15, pp. 963–965, 1986.

[20] V. Kesan, P. May, E. Bassous, and S. Iyer, "Integrated waveguide-photodetector using si/sige multiple quantum wells for long wavelength applications," in *Electron Devices Meeting*, pp. 637–40, 1990.

[21] B. Jalali, L. Naval, A. F. Levi, and P. G. Watson, "Gesi infrared photodetectors grown by rapid thermal cvd," in *Rapid Thermal and Laser Processing*, vol. 1804, pp. 94–107, International Society for Optics and Photonics, 1993.

[22] A. Splett, T. Zinke, K. Petermann, E. Kasper, H. Kibbel, H.-J. Herzog, and H. Presting, "Integration of waveguides and photodetectors in sige for 1.3/spl mu/m operation," *IEEE Photonics Technology Letters*, vol. 6, no. 1, pp. 59–61, 1994.

[23] A. Splett, "Ultimate performance of sige/si multiquantum well waveguide-photodetector combinations," in *ECOC'94. 20th European Conf. Optic. Commun.*, vol. 2, pp. 861–864, 1994.

[24] G. T. Reed, W. R. Headley, and C. J. Png, "Silicon photonics: The early years," in *Optoelectronic Integration on Silicon II*, vol. 5730, pp. 1–19, International Society for Optics and Photonics, 2005.

[25] R. Soref, "The past, present, and future of silicon photonics," *IEEE Journal of Selected Topics in Quantum Electronics*, vol. 12, no. 6, pp. 1678–1687, 2006.

[26] "Epixfab home page." `http://www.epixfab.eu`. Accessed: 2018-07-31.

[27] "Pixapp home page." `https://pixapp.eu`. Accessed: 2018-07-31.

[28] D. Thomson, A. Zilkie, J. E. Bowers, T. Komljenovic, G. T. Reed, L. Vivien, D. Marris-Morini, E. Cassan, L. Virot, J.-M. Fédéli, *et al.*, "Roadmap on silicon photonics," *Journal of Optics*, vol. 18, no. 7, p. 073003, 2016.

[29] "Forecast and methodology, 2016-2021 white paper," *Index, Cisco Global Cloud*, 2016.

[30] D. A. B. Miller, H. Ozaktas, *et al.*, "Limit to the bit-rate capacity of electrical interconnects from the aspect ratio of the system architecture," *Journal of Parallel and Distributed Computing*, vol. 41, no. 1, pp. 42–52, 1997.

[31] K. Kim, P. Dong, and A. Melikyan, "Silicon photonic devices for telecommunication and data center applications (conference presentation)," in *Next-Generation Optical Communication: Components, Sub-Systems, and Systems VII*, vol. 10561, p. 1056106, International Society for Optics and Photonics, 2018.

[32] M. Herrero-Collantes and J. C. Garcia-Escartin, "Quantum random number generators," *Reviews of Modern Physics*, vol. 89, no. 1, p. 015004, 2017.

[33] J. L. O'brien, A. Furusawa, and J. Vučković, "Photonic quantum technologies," *Nature Photonics*, vol. 3, no. 12, p. 687, 2009.

[34] "Europractise home page." `http://www.europractice-ic.com/index.php`. Accessed: 2018-07-19.

[35] V. Stojanović, R. J. Ram, M. Popović, S. Lin, S. Moazeni, M. Wade, C. Sun, L. Alloatti, A. Atabaki, F. Pavanello, *et al.*, "Monolithic silicon-photonic platforms in state-of-the-art cmos soi processes," *Optics Express*, vol. 26, no. 10, pp. 13106–13121, 2018.

[36] G. Li, J. Yao, H. Thacker, A. , X. Zheng, I. Shubin, Y. Luo, J.-H. Lee, K. Raj, J. E. Cunningham, *et al.*, "Ultralow-loss, high-density soi optical waveguide routing for macrochip interconnects," *Optics Express*, vol. 20, no. 11, pp. 12035–12039, 2012.

[37] J. Li, T. P. White, L. O'Faolain, A. Gomez-Iglesias, and T. F. Krauss, "Systematic design of flat band slow light in photonic crystal waveguides," *Optics Express*, vol. 16, no. 9, pp. 6227–6232, 2008.

[38] D. Gerace and L. C. Andreani, "Disorder-induced losses in photonic crystal waveguides with line defects," *Optics Letters*, vol. 29, no. 16, pp. 1897–1899, 2004.

[39] L. O'Faolain, T. P. White, D. O'Brien, X. Yuan, M. D. Settle, and T. F. Krauss, "Dependence of extrinsic loss on group velocity in photonic crystal waveguides," *Optics Express*, vol. 15, no. 20, pp. 13129–13138, 2007.

[40] M. Settle, M. Salib, A. Michaeli, and T. F. Krauss, "Low loss silicon on insulator photonic crystal waveguides made by 193nm optical lithography," *Optics Express*, vol. 14, no. 6, pp. 2440–2445, 2006.

[41] R. Halir, P. J. Bock, P. Cheben, A. Ortega-Moñux, C. Alonso-Ramos, J. H. Schmid, J. Lapointe, D.-X. Xu, J. G. Wangüemert-Pérez, Í. Molina-Fernández, *et al.*, "Waveguide sub-wavelength structures: a review of principles and applications," *Laser & Photonics Reviews*, vol. 9, no. 1, pp. 25–49, 2015.

[42] D. C. Flanders, "Submicrometer periodicity gratings as artificial anisotropic dielectrics," *Applied Physics Letters*, vol. 42, no. 6, pp. 492–494, 1983.

[43] P. Cheben, R. Halir, J. H. Schmid, H. A. Atwater, and D. R. Smith, "Subwavelength integrated photonics," *Nature*, vol. 560, no. 7720, p. 565, 2018.

[44] P. Cheben, D.-X. Xu, S. Janz, and A. Densmore, "Subwavelength waveguide grating for mode conversion and light coupling in integrated optics," *Optics Express*, vol. 14, no. 11, pp. 4695–4702, 2006.

[45] P. J. Bock, P. Cheben, J. H. Schmid, J. Lapointe, A. Delâge, S. Janz, G. C. Aers, D.-X. Xu, A. Densmore, and T. J. Hall, "Subwavelength grating periodic structures in silicon-on-insulator: a new type of microphotonic waveguide," *Optics Express*, vol. 18, no. 19, pp. 20251–20262, 2010.

[46] P. J. Bock, P. Cheben, J. H. Schmid, J. Lapointe, A. Delâge, D.-X. Xu, S. Janz, A. Densmore, and T. J. Hall, "Subwavelength grating crossings for silicon wire waveguides," *Optics Express*, vol. 18, no. 15, pp. 16146–16155, 2010.

[47] R. Halir, P. Cheben, J. Schmid, R. Ma, D. Bedard, S. Janz, D.-X. Xu, A. Densmore, J. Lapointe, and I. Molina-Fernández, "Continuously apodized fiber-to-chip surface grating coupler with refractive index engineered subwavelength structure," *Optics Letters*, vol. 35, no. 19, pp. 3243–3245, 2010.

[48] A. Sánchez-Postigo, J. G. Wangüemert-Pérez, J. M. Luque-González, Í. Molina-Fernández, P. Cheben, C. A. Alonso-Ramos, R. Halir, J. H. Schmid, and A. Ortega-Moñux, "Broadband fiber-chip zero-order surface grating coupler with 0.4 db efficiency," *Optics Letters*, vol. 41, no. 13, pp. 3013–3016, 2016.

[49] D. Benedikovic, C. Alonso-Ramos, P. Cheben, J. H. Schmid, S. Wang, D.-X. Xu, J. Lapointe, S. Janz, R. Halir, A. Ortega-Moñux,

et al., "High-directionality fiber-chip grating coupler with interleaved trenches and subwavelength index-matching structure," *Optics Letters*, vol. 40, no. 18, pp. 4190–4193, 2015.

[50] U. Levy, M. Abashin, K. Ikeda, A. Krishnamoorthy, J. Cunningham, and Y. Fainman, "Inhomogenous dielectric metamaterials with space-variant polarizability," *Physical Review Letters*, vol. 98, no. 24, p. 243901, 2007.

[51] H. Gao, B. Zhang, S. G. Johnson, and G. Barbastathis, "Design of thin–film photonic metamaterial lüneburg lens using analytical approach," *Optics Express*, vol. 20, no. 2, pp. 1617–1628, 2012.

[52] E. Cassan and K.-V. Do, "Analytic design of graded photonic crystals in the metamaterial regime," *Journal of the Optical Society of America B*, vol. 28, no. 8, pp. 1905–1910, 2011.

[53] P. J. Bock, P. Cheben, A. Delâge, J. H. Schmid, D.-X. Xu, S. Janz, and T. J. Hall, "Demultiplexer with blazed waveguide sidewall grating and sub-wavelength grating structure," *Optics Express*, vol. 16, no. 22, pp. 17616–17625, 2008.

[54] P. J. Bock, P. Cheben, J. H. Schmid, A. Delâge, D.-X. Xu, S. Janz, and T. J. Hall, "Sub-wavelength grating mode transformers in silicon slab waveguides," *Optics Express*, vol. 17, no. 21, pp. 19120–19133, 2009.

[55] I. Glesk, P. J. Bock, P. Cheben, J. H. Schmid, J. Lapointe, and S. Janz, "All-optical switching using nonlinear subwavelength mach-zehnder on silicon," *Optics Express*, vol. 19, no. 15, pp. 14031–14039, 2011.

[56] S. Akiyama, M. Imai, T. Baba, T. Akagawa, N. Hirayama, Y. Noguchi, M. Seki, K. Koshino, M. Toyama, T. Horikawa, *et al.*, "Compact pin-diode-based silicon modulator using side-wall-grating waveguide," *IEEE Journal of Selected Topics in Quantum Electronics*, vol. 19, no. 6, pp. 74–84, 2013.

[57] A. Ortega-Monux, L. Zavargo-Peche, A. Maese-Novo, I. Molina-Fernández, R. Halir, J. Wangüemert-Pérez, P. Cheben, and J. Schmid, "High-performance multimode interference coupler in silicon waveguides with subwavelength structures," *IEEE Photonics Technology Letters*, vol. 23, no. 19, pp. 1406–1408, 2011.

[58] R. Halir, P. Cheben, J. M. Luque-González, J. D. Sarmiento-Merenguel, J. H. Schmid, G. Wangüemert-Pérez, D.-X. Xu, S. Wang,

A. Ortega-Moñux, and Í. Molina-Fernández, "Ultra-broadband nanophotonic beamsplitter using an anisotropic sub-wavelength metamaterial," *Laser & Photonics Reviews*, vol. 10, no. 6, pp. 1039–1046, 2016.

[59] L. Xu, Y. Wang, A. Kumar, D. Patel, E. El-Fiky, Z. Xing, R. Li, and D. V. Plant, "Polarization beam splitter based on mmi coupler with swg birefringence engineering on soi," *IEEE Photon. Technol. Lett.*, vol. 30, no. 4, pp. 403–406, 2018.

[60] R. Halir, A. Ortega-Moñux, D. Benedikovic, G. Z. Mashanovich, J. G. Wanguemert-Perez, J. H. Schmid, I. Molina-Fernandez, and P. Cheben, "Subwavelength-grating metamaterial structures for silicon photonic devices," *Proceedings of the IEEE*, pp. 1–14, 2018.

[61] L. C. Andreani, D. Gerace, and M. Agio, "Gap maps, diffraction losses, and exciton–polaritons in photonic crystal slabs," *Photonics and Nanostructures-Fundamentals and Applications*, vol. 2, no. 2, pp. 103–110, 2004.

[62] A. W. Fang, E. Lively, Y.-H. Kuo, D. Liang, and J. E. Bowers, "A distributed feedback silicon evanescent laser," *Optics Express*, vol. 16, no. 7, pp. 4413–4419, 2008.

[63] A. Descos, C. Jany, D. Bordel, H. Duprez, G. B. de Farias, P. Brianceau, S. Menezo, and B. B. Bakir, "Heterogeneously integrated iii-v/si distributed bragg reflector laser with adiabatic coupling," in *Optical Communication (ECOC 2013), 39th European Conference and Exhibition on*, pp. 1–3, IET, 2013.

[64] N. N. Klimov, S. Mittal, M. Berger, and Z. Ahmed, "On-chip silicon waveguide bragg grating photonic temperature sensor," *Optics Letters*, vol. 40, no. 17, pp. 3934–3936, 2015.

[65] V. Passaro, F. Dell'Olio, B. Casamassima, and F. De Leonardis, "Guided-wave optical biosensors," *Sensors*, vol. 7, no. 4, pp. 508–536, 2007.

[66] D. Taillaert, P. Bienstman, and R. Baets, "Compact efficient broadband grating coupler for silicon-on-insulator waveguides," *Optics Letters*, vol. 29, no. 23, pp. 2749–2751, 2004.

[67] L. Carroll, D. Gerace, I. Cristiani, and L. C. Andreani, "Optimizing polarization-diversity couplers for si-photonics: reaching the- 1db coupling efficiency threshold," *Optics Express*, vol. 22, no. 12, pp. 14769–14781, 2014.

[68] X. Chen and H. K. Tsang, "Polarization-independent grating couplers for silicon-on-insulator nanophotonic waveguides," *Optics Letters*, vol. 36, no. 6, pp. 796–798, 2011.

[69] D. Vermeulen, S. Selvaraja, P. Verheyen, G. Lepage, W. Bogaerts, P. Absil, D. Van Thourhout, and G. Roelkens, "High-efficiency fiber-to-chip grating couplers realized using an advanced cmos-compatible silicon-on-insulator platform," *Optics Express*, vol. 18, no. 17, pp. 18278–18283, 2010.

[70] A. Bozzola, L. Carroll, D. Gerace, I. Cristiani, and L. C. Andreani, "Optimising apodized grating couplers in a pure soi platform to- 0.5 db coupling efficiency," *Optics Express*, vol. 23, no. 12, pp. 16289–16304, 2015.

[71] R. Marchetti, C. Lacava, A. Khokhar, X. Chen, I. Cristiani, D. J. Richardson, G. T. Reed, P. Petropoulos, and P. Minzioni, "High-efficiency grating-couplers: demonstration of a new design strategy," *Scientific Reports*, vol. 7, no. 1, p. 16670, 2017.

[72] X. Chen, C. Li, and H. K. Tsang, "Two dimensional silicon waveguide chirped grating couplers for vertical optical fibers," *Optics Communications*, vol. 283, no. 10, pp. 2146–2149, 2010.

[73] F. Van Laere, T. Claes, J. Schrauwen, S. Scheerlinck, W. Bogaerts, D. Taillaert, L. O'FAOLAIN, D. Van Thourhout, and R. Baets, "Compact focusing grating couplers for silicon-on-insulator integrated circuits," *IEEE Photonics Technology Letters*, vol. 19, no. 21-24, pp. 1919–1921, 2007.

[74] F. Van Laere, W. Bogaerts, P. Dumon, G. Roelkens, D. Van Thourhout, and R. Baets, "Focusing polarization diversity grating couplers in silicon-on-insulator," *Journal of Lightwave Technology*, vol. 27, no. 5, pp. 612–618, 2009.

[75] P. Kumar, B. Bergner, D. Cook, and I. Avrutsky, "Light focusing by chirped waveguide grating coupler," in *Next-Generation Spectroscopic Technologies IV*, vol. 8032, p. 803203, International Society for Optics and Photonics, 2011.

[76] Y. Wang, X. Wang, J. Flueckiger, H. Yun, W. Shi, R. Bojko, N. A. Jaeger, and L. Chrostowski, "Focusing sub-wavelength grating couplers with low back reflections for rapid prototyping of silicon photonic circuits," *Optics Express*, vol. 22, no. 17, pp. 20652–20662, 2014.

[77] C. Sauvan, J.-P. Hugonin, I. Maksymov, and P. Lalanne, "Theory of the spontaneous optical emission of nanosize photonic and plasmon resonators," *Physical Review Letters*, vol. 110, no. 23, p. 237401, 2013.

[78] W. Bogaerts, P. De Heyn, T. Van Vaerenbergh, K. De Vos, S. Kumar Selvaraja, T. Claes, P. Dumon, P. Bienstman, D. Van Thourhout, and R. Baets, "Silicon microring resonators," *Laser & Photonics Reviews*, vol. 6, no. 1, pp. 47–73, 2012.

[79] A. B. Matsko and V. S. Ilchenko, "Optical resonators with whispering gallery modes i: basics," *IEEE J. Sel. Top. Quantum Electron*, vol. 12, no. 3, p. 3, 2006.

[80] V. S. Ilchenko and A. B. Matsko, "Optical resonators with whispering-gallery modes-part ii: applications," *IEEE Journal of Selected Topics in Quantum Electronics*, vol. 12, no. 1, pp. 15–32, 2006.

[81] M. Soltani, S. Yegnanarayanan, and A. Adibi, "Ultra-high q planar silicon microdisk resonators for chip-scale silicon photonics," *Optics Express*, vol. 15, no. 8, pp. 4694–4704, 2007.

[82] B. Liu, A. Shakouri, and J. E. Bowers, "Wide tunable double ring resonator coupled lasers," *IEEE Photonics Technology Letters*, vol. 14, no. 5, pp. 600–602, 2002.

[83] M. Iqbal, M. A. Gleeson, B. Spaugh, F. Tybor, W. G. Gunn, M. Hochberg, T. Baehr-Jones, R. C. Bailey, and L. C. Gunn, "Label-free biosensor arrays based on silicon ring resonators and high-speed optical scanning instrumentation," *IEEE Journal of Selected Topics in Quantum Electronics*, vol. 16, no. 3, pp. 654–661, 2010.

[84] S. M. Grist, S. A. Schmidt, J. Flueckiger, V. Donzella, W. Shi, S. T. Fard, J. T. Kirk, D. M. Ratner, K. C. Cheung, and L. Chrostowski, "Silicon photonic micro-disk resonators for label-free biosensing," *Optics Express*, vol. 21, no. 7, pp. 7994–8006, 2013.

[85] Q. Xu, B. Schmidt, S. Pradhan, and M. Lipson, "Micrometre-scale silicon electro-optic modulator," *Nature*, vol. 435, no. 7040, p. 325, 2005.

[86] G. N. Nielson, D. Seneviratne, F. Lopez-Royo, P. T. Rakich, Y. Avrahami, M. R. Watts, H. A. Haus, H. L. Tuller, and G. Barbastathis, "Integrated wavelength-selective optical mems switching using ring resonator filters," *IEEE Photonics Technology Letters*, vol. 17, no. 6, pp. 1190–1192, 2005.

[87] Y. Vlasov, W. M. Green, and F. Xia, "High-throughput silicon nanophotonic wavelength-insensitive switch for on-chip optical networks," *Nature Photonics*, vol. 2, no. 4, p. 242, 2008.

[88] N. Sherwood-Droz, H. Wang, L. Chen, B. G. Lee, A. Biberman, K. Bergman, and M. Lipson, "Optical 4× 4 hitless silicon router for optical networks-on-chip (noc)," *Optics Express*, vol. 16, no. 20, pp. 15915–15922, 2008.

[89] J. Rosenberg, Q. Lin, and O. Painter, "Static and dynamic wavelength routing via the gradient optical force," *Nature Photonics*, vol. 3, no. 8, p. 478, 2009.

[90] G. Priem, P. Dumon, W. Bogaerts, D. Van Thourhout, G. Morthier, and R. Baets, "Optical bistability and pulsating behaviour in silicon-on-insulator ring resonator structures.," *Optics Express*, vol. 13, no. 23, pp. 9623–9628, 2005.

[91] P. Absil, J. Hryniewicz, B. Little, P. Cho, R. Wilson, L. Joneckis, and P.-T. Ho, "Wavelength conversion in gaas micro-ring resonators," *Optics Letters*, vol. 25, no. 8, pp. 554–556, 2000.

[92] P. Lalanne, C. Sauvan, and J. P. Hugonin, "Photon confinement in photonic crystal nanocavities," *Laser & Photonics Reviews*, vol. 2, no. 6, pp. 514–526, 2008.

[93] D. Gerace and L. C. Andreani, "Effects of disorder on propagation losses and cavity q-factors in photonic crystal slabs," *Photonics and Nanostructures-Fundamentals and Applications*, vol. 3, no. 2-3, pp. 120–128, 2005.

[94] J. Foresi, P. R. Villeneuve, J. Ferrera, E. Thoen, G. Steinmeyer, S. Fan, J. Joannopoulos, L. Kimerling, H. I. Smith, and E. Ippen, "Photonic-bandgap microcavities in optical waveguides," *Nature*, vol. 390, no. 6656, p. 143, 1997.

[95] E. Kuramochi, H. Taniyama, T. Tanabe, K. Kawasaki, Y.-G. Roh, and M. Notomi, "Ultrahigh-q one-dimensional photonic crystal nanocavities with modulated mode-gap barriers on sio 2 claddings and on air claddings," *Optics Express*, vol. 18, no. 15, pp. 15859–15869, 2010.

[96] U. P. Dharanipathy, M. Minkov, M. Tonin, V. Savona, and R. Houdré, "High-q silicon photonic crystal cavity for enhanced optical nonlinearities," *Applied Physics Letters*, vol. 105, no. 10, p. 101101, 2014.

[97] J. Hagemeier, C. Bonato, T.-A. Truong, H. Kim, G. J. Beirne, M. Bakker, M. P. van Exter, Y. Luo, P. Petroff, and D. Bouwmeester, "H1 photonic crystal cavities for hybrid quantum information protocols," *Optics Express*, vol. 20, no. 22, pp. 24714–24726, 2012.

[98] Y. Akahane, T. Asano, B.-S. Song, and S. Noda, "High-q photonic nanocavity in a two-dimensional photonic crystal," *Nature*, vol. 425, no. 6961, p. 944, 2003.

[99] S. Combrié, A. De Rossi, *et al.*, "Directive emission from high-q photonic crystal cavities through band folding," *Physical Review B*, vol. 79, no. 4, p. 041101, 2009.

[100] B.-S. Song, S. Noda, T. Asano, and Y. Akahane, "Ultra-high-q photonic double-heterostructure nanocavity," *Nature Materials*, vol. 4, no. 3, p. 207, 2005.

[101] E. Kuramochi, M. Notomi, S. Mitsugi, A. Shinya, T. Tanabe, and T. Watanabe, "Ultrahigh-q photonic crystal nanocavities realized by the local width modulation of a line defect," *Applied Physics Letters*, vol. 88, no. 4, p. 041112, 2006.

[102] F. Alpeggiani, L. C. Andreani, and D. Gerace, "Effective bichromatic potential for ultra-high q-factor photonic crystal slab cavities," *Applied Physics Letters*, vol. 107, no. 26, p. 261110, 2015.

[103] P. Cheben, "Wavelength dispersive planar waveguide devices: echelle and arrayed waveguide gratings," in *Optical Waveguides*, pp. 193–250, CRC Press, 2007.

[104] W. Wang, Y. Tang, Y. Wang, H. Qu, Y. Wu, T. Li, J. Yang, Y. Wang, and M. Liu, "Etched-diffraction-grating-based planar waveguide demultiplexer on silicon-on-insulator," *optical and Quantum Electronics*, vol. 36, no. 6, pp. 559–566, 2004.

[105] X. J. Leijtens, B. Kuhlow, and M. K. Smit, "Arrayed waveguide gratings," in *Wavelength Filters in Fibre Optics*, pp. 125–187, Springer, 2006.

[106] P. Cheben, D.-X. Xu, S. Janz, and A. Delâge, "Scaling down photonic waveguide devices on the soi platform," in *VLSI Circuits and Systems*, vol. 5117, pp. 147–157, International Society for Optics and Photonics, 2003.

[107] S. Pathak, D. Van Thourhout, and W. Bogaerts, "Design trade-offs for silicon-on-insulator-based awgs for (de) multiplexer applications," *Optics Letters*, vol. 38, no. 16, pp. 2961–2964, 2013.

[108] K. Sasaki, F. Ohno, A. Motegi, and T. Baba, "Arrayed waveguide grating of 70/spl times/60/spl mu/m/sup 2/size based on si photonic wire waveguides," *Electronics Letters*, vol. 41, no. 14, pp. 801–802, 2005.

[109] W. Bogaerts, P. Dumon, D. Van Thourhout, D. Taillaert, P. Jaenen, J. Wouters, S. Beckx, V. Wiaux, and R. G. Baets, "Compact wavelength-selective functions in silicon-on-insulator photonic wires," *IEEE Journal of Selected Topics in Quantum Electronics*, vol. 12, no. 6, pp. 1394–1401, 2006.

[110] P. Cheben, J. Schmid, A. Delâge, A. Densmore, S. Janz, B. Lamontagne, J. Lapointe, E. Post, P. Waldron, and D.-X. Xu, "A high-resolution silicon-on-insulator arrayed waveguide grating microspectrometer with sub-micrometer aperture waveguides," *Optics Express*, vol. 15, no. 5, pp. 2299–2306, 2007.

[111] S. Kamei, Y. Inoue, A. Kaneko, T. Shibata, and H. Takahashi, "Recent progress on athermal awg wavelength multiplexer," in *Active and Passive Optical Components for WDM Communications V*, vol. 6014, p. 60140H, International Society for Optics and Photonics, 2005.

[112] D. Dai, J. Wang, S. Chen, S. Wang, and S. He, "Monolithically integrated 64-channel silicon hybrid demultiplexer enabling simultaneous wavelength-and mode-division-multiplexing," *Laser & Photonics Reviews*, vol. 9, no. 3, pp. 339–344, 2015.

[113] S. Chen, Y. Shi, S. He, and D. Dai, "Compact eight-channel thermally reconfigurable optical add/drop multiplexers on silicon," *IEEE Photonics Technology Letters*, vol. 28, no. 17, pp. 1874–1877, 2016.

[114] P. Cheben, P. J. Bock, J. H. Schmid, J. Lapointe, S. Janz, D.-X. Xu, A. Densmore, A. Delâge, B. Lamontagne, and T. J. Hall, "Refractive index engineering with subwavelength gratings for efficient microphotonic couplers and planar waveguide multiplexers," *Optics Letters*, vol. 35, no. 15, pp. 2526–2528, 2010.

[115] D. Pavesi, "Silicon fundamentals for photonics applications," *Silicon Photonics*, pp. 2000–2000, 2004.

[116] U. Gösele and V. Lehmann, "Light-emitting porous silicon," *Materials Chemestry and Physics*, vol. 40, no. 4, pp. 253–259, 1995.

[117] O. Bisi, S. Ossicini, and L. Pavesi, "Porous silicon: a quantum sponge structure for silicon based optoelectronics," *Surface Science Reports*, vol. 38, no. 1-3, pp. 1–126, 2000.

[118] L. Pavesi, L. Dal Negro, C. Mazzoleni, G. Franzo, and d. F. Priolo, "Optical gain in silicon nanocrystals," *Nature*, vol. 408, no. 6811, p. 440, 2000.

[119] Z. Lu, D. Lockwood, and J.-M. Baribeau, "Quantum confinement and light emission in sio2/si superlattices," *Nature*, vol. 378, no. 6554, p. 258, 1995.

[120] S. G. Cloutier, P. A. Kossyrev, and J. Xu, "Optical gain and stimulated emission in periodic nanopatterned crystalline silicon," *Nature Materials*, vol. 4, no. 12, p. 887, 2005.

[121] O. Boyraz and B. Jalali, "Demonstration of a silicon raman laser," *Optics Express*, vol. 12, no. 21, pp. 5269–5273, 2004.

[122] H. Rong, R. Jones, A. Liu, O. Cohen, D. Hak, A. Fang, and M. Paniccia, "A continuous-wave raman silicon laser," *Nature*, vol. 433, no. 7027, p. 725, 2005.

[123] H. Kawanami, "Heteroepitaxial technologies of iii–v on si," *Solar Energy Materials and Solar Cells*, vol. 66, no. 1-4, pp. 479–486, 2001.

[124] M. E. Groenert, C. W. Leitz, A. J. Pitera, V. Yang, H. Lee, R. J. Ram, and E. A. Fitzgerald, "Monolithic integration of room-temperature cw gaas/algaas lasers on si substrates via relaxed graded gesi buffer layers," *Journal of Applied Physics*, vol. 93, no. 1, pp. 362–367, 2003.

[125] L. Cerutti, J.-B. Rodriguez, and E. Tournié, "Gasb-based laser, monolithically grown on silicon substrate, emitting at 1.55 μm at room temperature," *IEEE Photonics Technology Letters*, vol. 22, no. 8, pp. 553–555, 2010.

[126] G. Roelkens, L. Liu, D. Liang, R. Jones, A. Fang, B. Koch, and J. Bowers, "Iii-v/silicon photonics for on-chip and intra-chip optical interconnects," *Laser & Photonics Reviews*, vol. 4, no. 6, pp. 751–779, 2010.

[127] B. Corbett, R. Loi, W. Zhou, D. Liu, and Z. Ma, "Transfer print techniques for heterogeneous integration of photonic components," *Progress in Quantum Electronics*, vol. 52, pp. 1–17, 2017.

[128] J. Van Campenhout, P. Rojo-Romeo, P. Regreny, C. Seassal, D. Van Thourhout, S. Verstuyft, L. Di Cioccio, J.-M. Fedeli, C. Lagahe, and R. Baets, "Electrically pumped inp-based microdisk lasers integrated with a nanophotonic silicon-on-insulator waveguide circuit," *Optics Express*, vol. 15, no. 11, pp. 6744–6749, 2007.

[129] J. Van Campenhout, L. Liu, P. R. Romeo, D. Van Thourhout, C. Seassal, P. Regreny, L. Di Cioccio, J.-M. Fedeli, and R. Baets, "A compact soi-integrated multiwavelength laser source based on cascaded inp microdisks," *IEEE Photonics Technology Letters*, vol. 20, no. 16, pp. 1345–1347, 2008.

[130] A. W. Fang, B. R. Koch, K.-G. Gan, H. Park, R. Jones, O. Cohen, M. J. Paniccia, D. J. Blumenthal, and J. E. Bowers, "A racetrack mode-locked silicon evanescent laser," *Optics Express*, vol. 16, no. 2, pp. 1393–1398, 2008.

[131] G. Roelkens, D. Van Thourhout, R. Baets, R. Nötzel, and M. Smit, "Laser emission and photodetection in an inp/ingaasp layer integrated on and coupled to a silicon-on-insulator waveguide circuit," *Optics Express*, vol. 14, no. 18, pp. 8154–8159, 2006.

[132] A. W. Fang, H. Park, O. Cohen, R. Jones, M. J. Paniccia, and J. E. Bowers, "Electrically pumped hybrid algainas-silicon evanescent laser," *Optics Express*, vol. 14, no. 20, pp. 9203–9210, 2006.

[133] J. Justice, C. Bower, M. Meitl, M. B. Mooney, M. A. Gubbins, and B. Corbett, "Wafer-scale integration of group iii–v lasers on silicon using transfer printing of epitaxial layers," *Nature Photonics*, vol. 6, no. 9, p. 610, 2012.

[134] X. Sheng, C. Robert, S. Wang, G. Pakeltis, B. Corbett, and J. A. Rogers, "Transfer printing of fully formed thin-film microscale gaas lasers on silicon with a thermally conductive interface material," *Laser & Photonics Reviews*, vol. 9, no. 4, pp. L17–L22, 2015.

[135] A. De Groote, P. Cardile, A. Z. Subramanian, A. M. Fecioru, C. Bower, D. Delbeke, R. Baets, and G. Roelkens, "Transfer-printing-based integration of single-mode waveguide-coupled iii-v-on-silicon broadband light emitters," *Optics Express*, vol. 24, no. 13, pp. 13754–13762, 2016.

[136] R. Loi, J. O'Callaghan, B. Roycroft, C. Robert, A. Fecioru, A. J. Trindade, A. Gocalinska, E. Pelucchi, C. A. Bower, and B. Corbett, "Transfer printing of algainas/inp etched facet lasers to si substrates," *IEEE Photonics Journal*, vol. 8, no. 6, pp. 1–10, 2016.

[137] D. Liang and J. E. Bowers, "Recent progress in lasers on silicon," *Nature Photonics*, vol. 4, no. 8, p. 511, 2010.

[138] P. Damas, X. Le Roux, D. Le Bourdais, E. Cassan, D. Marris-Morini, N. Izard, T. Maroutian, P. Lecoeur, and L. Vivien, "Wavelength dependence of pockels effect in strained silicon waveguides," *Optics Express*, vol. 22, no. 18, pp. 22095–22100, 2014.

[139] C. L. Manganelli, P. Pintus, and C. Bonati, "Modeling of strain-induced pockels effect in silicon," *Optics Express*, vol. 23, no. 22, pp. 28649–28666, 2015.

[140] B. Chmielak, M. Waldow, C. Matheisen, C. Ripperda, J. Bolten, T. Wahlbrink, M. Nagel, F. Merget, and H. Kurz, "Pockels effect based fully integrated, strained silicon electro-optic modulator," *Optics Express*, vol. 19, no. 18, pp. 17212–17219, 2011.

[141] M. Borghi, M. Mancinelli, F. Merget, J. Witzens, M. Bernard, M. Ghulinyan, G. Pucker, and L. Pavesi, "High-frequency electro-optic measurement of strained silicon racetrack resonators," *Optics Letters*, vol. 40, no. 22, pp. 5287–5290, 2015.

[142] C. Sun, M. T. Wade, Y. Lee, J. S. Orcutt, L. Alloatti, M. S. Georgas, A. S. Waterman, J. M. Shainline, R. R. Avizienis, S. Lin, *et al.*, "Single-chip microprocessor that communicates directly using light," *Nature*, vol. 528, no. 7583, p. 534, 2015.

[143] G. T. Reed, G. Mashanovich, F. Y. Gardes, and D. Thomson, "Silicon optical modulators," *Nature Photonics*, vol. 4, no. 8, p. 518, 2010.

[144] F. Gardes, A. Brimont, P. Sanchis, G. Rasigade, D. Marris-Morini, L. O'Faolain, F. Dong, J. Fedeli, P. Dumon, L. Vivien, *et al.*, "High-speed modulation of a compact silicon ring resonator based on a reverse-biased pn diode," *Optics Express*, vol. 17, no. 24, pp. 21986–21991, 2009.

[145] P. Dong, S. Liao, D. Feng, H. Liang, D. Zheng, R. Shafiiha, C.-C. Kung, W. Qian, G. Li, X. Zheng, *et al.*, "Low v pp, ultralow-energy, compact, high-speed silicon electro-optic modulator," *Optics Express*, vol. 17, no. 25, pp. 22484–22490, 2009.

[146] J.-B. You, M. Park, J.-W. Park, and G. Kim, "12.5 gbps optical modulation of silicon racetrack resonator based on carrier-depletion in asymmetric pn diode," *Optics Express*, vol. 16, no. 22, pp. 18340–18344, 2008.

[147] M. Y. Liu and S. Y. Chou, "High-modulation-depth and short-cavity-length silicon fabry–perot modulator with two grating bragg reflectors," *Applied Physics Letters*, vol. 68, no. 2, pp. 170–172, 1996.

[148] B. Schmidt, Q. Xu, J. Shakya, S. Manipatruni, and M. Lipson, "Compact electro-optic modulator on silicon-on-insulator substrates using cavities with ultra-small modal volumes," *Optics Express*, vol. 15, no. 6, pp. 3140–3148, 2007.

[149] T. Tanabe, K. Nishiguchi, E. Kuramochi, and M. Notomi, "Low power and fast electro-optic silicon modulator with lateral pin embedded photonic crystal nanocavity," *Optics Express*, vol. 17, no. 25, pp. 22505–22513, 2009.

[150] A. Liu, L. Liao, D. Rubin, H. Nguyen, B. Ciftcioglu, Y. Chetrit, N. Izhaky, and M. Paniccia, "High-speed optical modulation based on carrier depletion in a silicon waveguide," *Optics Express*, vol. 15, no. 2, pp. 660–668, 2007.

[151] L. Liao, A. Liu, D. Rubin, J. Basak, Y. Chetrit, H. Nguyen, R. Cohen, N. Izhaky, and M. Paniccia, "40 gbit/s silicon optical modulator for high-speed applications," *Electronics Letters*, vol. 43, no. 22, pp. 1196–1197, 2007.

[152] D. Marris-Morini, L. Vivien, J. M. Fédéli, E. Cassan, P. Lyan, and S. Laval, "Low loss and high speed silicon optical modulator based on a lateral carrier depletion structure," *Optics Express*, vol. 16, no. 1, pp. 334–339, 2008.

[153] J. W. Park, J.-B. You, I. G. Kim, and G. Kim, "High-modulation efficiency silicon mach-zehnder optical modulator based on carrier depletion in a pn diode," *Optics Express*, vol. 17, no. 18, pp. 15520–15524, 2009.

[154] L. Gu, W. Jiang, X. Chen, L. Wang, and R. T. Chen, "High speed silicon photonic crystal waveguide modulator for low voltage operation," *Applied Physics Letters*, vol. 90, no. 7, p. 071105, 2007.

[155] J.-M. Brosi, C. Koos, L. C. Andreani, M. Waldow, J. Leuthold, and W. Freude, "High-speed low-voltage electro-optic modulator with a polymer-infiltrated silicon photonic crystal waveguide," *Optics Express*, vol. 16, no. 6, pp. 4177–4191, 2008.

[156] D. M. Beggs, T. P. White, L. O'Faolain, and T. F. Krauss, "Ultracompact and low-power optical switch based on silicon photonic crystals," *Optics Letters*, vol. 33, no. 2, pp. 147–149, 2008.

[157] A. Brimont, P. Sanchis, and J. Martí, "Strong electro-optical modulation enhancement in a slow wave corrugated waveguide," *Optics Express*, vol. 17, no. 11, pp. 9204–9211, 2009.

[158] A. Brimont, D. Thomson, F. Gardes, J. Fedeli, G. Reed, J. Martí, and P. Sanchis, "High-contrast 40 gb/s operation of a 500 μm long silicon carrier-depletion slow wave modulator," *Optics Letters*, vol. 37, no. 17, pp. 3504–3506, 2012.

[159] J. Doylend, P. Jessop, and A. Knights, "Silicon photonic resonator-enhanced defect-mediated photodiode for sub-bandgap detection," *Optics Express*, vol. 18, no. 14, pp. 14671–14678, 2010.

[160] J. Brouckaert, G. Roelkens, D. Van Thourhout, and R. Baets, "Thin-film iii–v photodetectors integrated on silicon-on-insulator photonic ics," *Journal of Lightwave Technology*, vol. 25, no. 4, pp. 1053–1060, 2007.

[161] H. Park, A. W. Fang, R. Jones, O. Cohen, O. Raday, M. N. Sysak, M. J. Paniccia, and J. E. Bowers, "A hybrid algainas-silicon evanescent waveguide photodetector," *Optics Express*, vol. 15, no. 10, pp. 6044–6052, 2007.

[162] A. D. Stiff, S. Krishna, P. Bhattacharya, and S. W. Kennerly, "Normal-incidence, high-temperature, mid-infrared, inas-gaas vertical quantum-dot infrared photodetector," *IEEE Journal of Quantum Electronics*, vol. 37, no. 11, pp. 1412–1419, 2001.

[163] J. Michel, J. Liu, and L. C. Kimerling, "High-performance ge-on-si photodetectors," *Nature Photonics*, vol. 4, no. 8, p. 527, 2010.

[164] C. T. DeRose, D. C. Trotter, W. A. Zortman, A. L. Starbuck, M. Fisher, M. R. Watts, and P. S. Davids, "Ultra compact 45 ghz cmos compatible germanium waveguide photodiode with low dark current," *Optics Express*, vol. 19, no. 25, pp. 24897–24904, 2011.

[165] S. Assefa, F. Xia, and Y. A. Vlasov, "Reinventing germanium avalanche photodetector for nanophotonic on-chip optical interconnects," *Nature*, vol. 464, no. 7285, p. 80, 2010.

[166] L. Vivien, J. Osmond, J.-M. Fédéli, D. Marris-Morini, P. Crozat, J.-F. Damlencourt, E. Cassan, Y. Lecunff, and S. Laval, "42 ghz pin germanium photodetector integrated in a silicon-on-insulator waveguide," *Optics Express*, vol. 17, no. 8, pp. 6252–6257, 2009.

[167] F. Morichetti, S. Grillanda, M. Carminati, G. Ferrari, M. Sampietro, M. J. Strain, M. Sorel, and A. Melloni, "Non-invasive on-chip light observation by contactless waveguide conductivity monitoring," *IEEE Journal of Selected Topics in Quantum Electronics*, vol. 20, no. 4, pp. 292–301, 2014.

[168] F. Morichetti, S. Grillanda, and A. Melloni, "Breakthroughs in photonics 2013: toward feedback-controlled integrated photonics," *IEEE Photonics Journal*, vol. 6, no. 2, pp. 1–6, 2014.

[169] L. Qiao, W. Tang, and T. Chu, "32× 32 silicon electro-optic switch with built-in monitors and balanced-status units," *Scientific Reports*, vol. 7, p. 42306, 2017.

[170] J. D. Joannopoulos, S. G. Johnson, J. N. Winn, and R. D. Meade, *Photonic crystals: molding the flow of light*. Princeton university press, 2011.

[171] J. D. Jackson, *Classical electrodynamics*. Wiley, 1999.

[172] E. Chow, S. Lin, S. Johnson, P. Villeneuve, J. Joannopoulos, J. R. Wendt, G. A. Vawter, W. Zubrzycki, H. Hou, and A. Alleman, "Three-dimensional control of light in a two-dimensional photonic crystal slab," *Nature*, vol. 407, no. 6807, p. 983, 2000.

[173] T. Ochiai and K. Sakoda, "Dispersion relation and optical transmittance of a hexagonal photonic crystal slab," *Physical Review B*, vol. 63, no. 12, p. 125107, 2001.

[174] S. Fan and J. Joannopoulos, "Analysis of guided resonances in photonic crystal slabs," *Physical Review B*, vol. 65, no. 23, p. 235112, 2002.

[175] L. C. Andreani and D. Gerace, "Photonic-crystal slabs with a triangular lattice of triangular holes investigated using a guided-mode expansion method," *Physical Review B*, vol. 73, no. 23, p. 235114, 2006.

[176] D. Gerace and L. C. Andreani, "Low-loss guided modes in photonic crystal waveguides," *Optics Express*, vol. 13, no. 13, pp. 4939–4951, 2005.

[177] K. Yee, "Numerical solution of initial boundary value problems involving maxwell's equations in isotropic media," *IEEE Transactions on Antennas and Propagation*, vol. 14, no. 3, pp. 302–307, 1966.

[178] A. Taflove and S. C. Hagness, *Computational electrodynamics: the finite-difference time-domain method*. Artech house, 2005.

[179] D. Whittaker and I. Culshaw, "Scattering-matrix treatment of patterned multilayer photonic structures," *Physical Review B*, vol. 60, no. 4, p. 2610, 1999.

[180] M. Liscidini, D. Gerace, L. C. Andreani, and J. Sipe, "Scattering-matrix analysis of periodically patterned multilayers with asymmetric unit cells and birefringent media," *Physical Review B*, vol. 77, no. 3, p. 035324, 2008.

[181] Y. Wang, D. Aurelio, W. Li, P. Tseng, Z. Zheng, M. Li, D. L. Kaplan, M. Liscidini, and F. G. Omenetto, "Modulation of multiscale 3d lattices through conformational control: Painting silk inverse opals with water and light," *Advanced Materials*, vol. 29, no. 38, 2017.

[182] L. Li, "New formulation of the fourier modal method for crossed surface-relief gratings," *Journal of the Optical Seciety of America A*, vol. 14, no. 10, pp. 2758–2767, 1997.

[183] J. Hugonin, P. Lalanne, I. D. Villar, and I. Matias, "Fourier modal methods for modeling optical dielectric waveguides," *optical and Quantum Electronics*, vol. 37, no. 1-3, pp. 107–119, 2005.

[184] L. Carroll, J.-S. Lee, C. Scarcella, K. Gradkowski, M. Duperron, H. Lu, Y. Zhao, C. Eason, P. Morrissey, M. Rensing, *et al.*, "Photonic packaging: transforming silicon photonic integrated circuits into photonic devices," *Applied Sciences*, vol. 6, no. 12, p. 426, 2016.

[185] T. Shoji, T. Tsuchizawa, T. Watanabe, K. Yamada, and H. Morita, "Low loss mode size converter from 0.3 μm square si wire waveguides to singlemode fibres," *Electronics Letters*, vol. 38, no. 25, pp. 1669–1670, 2002.

[186] J. H. Song, H. N. Fernando, B. Roycroft, B. Corbett, and F. H. Peters, "Practical design of lensed fibers for semiconductor laser packaging using laser welding technique," *Journal of Lightwave Technology*, vol. 27, no. 11, pp. 1533–1539, 2009.

[187] S. J. McNab, N. Moll, and Y. A. Vlasov, "Ultra-low loss photonic integrated circuit with membrane-type photonic crystal waveguides," *Optics Express*, vol. 11, no. 22, pp. 2927–2939, 2003.

[188] M. Pu, L. Liu, H. Ou, K. Yvind, and J. M. Hvam, "Ultra-low-loss inverted taper coupler for silicon-on-insulator ridge waveguide," *Optics Communications*, vol. 283, no. 19, pp. 3678–3682, 2010.

[189] B. B. Bakir, A. V. De Gyves, R. Orobtchouk, P. Lyan, C. Porzier, A. Roman, and J.-M. Fedeli, "Low-loss (<1 db) and polarization-insensitive edge fiber couplers fabricated on 200-mm silicon-on-insulator wafers," *IEEE Photonics Technology Letters*, vol. 22, no. 11, pp. 739–741, 2010.

[190] S. Romero-García, B. Marzban, F. Merget, B. Shen, and J. Witzens, "Edge couplers with relaxed alignment tolerance for pick-and-place hybrid integration of iii–v lasers with soi waveguides," *IEEE Journal of Selected Topics in Quantum Electronics*, vol. 20, no. 4, pp. 369–379, 2014.

[191] P. Cheben, J. H. Schmid, S. Wang, D.-X. Xu, M. Vachon, S. Janz, J. Lapointe, Y. Painchaud, and M.-J. Picard, "Broadband polarization independent nanophotonic coupler for silicon waveguides with ultra-high efficiency," *Optics Express*, vol. 23, no. 17, pp. 22553–22563, 2015.

[192] R. Takei, E. Omoda, M. Suzuki, S. Manako, T. Kamei, M. Mori, and Y. Sakakibara, "Ultranarrow silicon inverse taper waveguide fabricated with double-patterning photolithography for low-loss spot-size converter," *Applied Physics Express*, vol. 5, no. 5, p. 052202, 2012.

[193] T. Barwicz, Y. Taira, T. W. Lichoulas, N. Boyer, Y. Martin, H. Numata, J.-W. Nah, S. Takenobu, A. Janta-Polczynski, E. L. Kimbrell, *et al.*, "A novel approach to photonic packaging leveraging existing

high-throughput microelectronic facilities," *IEEE Journal of Selected Topics in Quantum Electronics*, vol. 22, no. 6, pp. 455–466, 2016.

[194] A. Mekis, S. Gloeckner, G. Masini, A. Narasimha, T. Pinguet, S. Sahni, and P. De Dobbelaere, "A grating-coupler-enabled cmos photonics platform," *IEEE Journal of Selected Topics in Quantum Electronics*, vol. 17, no. 3, pp. 597–608, 2011.

[195] Z. Xiao, T.-Y. Liow, J. Zhang, P. Shum, and F. Luan, "Bandwidth analysis of waveguide grating coupler," *Optics Express*, vol. 21, no. 5, pp. 5688–5700, 2013.

[196] G. Roelkens, D. Van Thourhout, and R. Baets, "High efficiency silicon-on-insulator grating coupler based on a poly-silicon overlay," *Optics Express*, vol. 14, no. 24, pp. 11622–11630, 2006.

[197] Vivien, Pascal, Lardenois, Marris-Morini, Cassan, Grillot, Laval, Fedeli, and L. E. Melhaoui, "Light injection in soi microwaveguides using high-efficiency grating couplers," *Journal of Lightwave Technology*, vol. 24, pp. 3810–3815, Oct 2006.

[198] L. Carroll, D. Gerace, I. Cristiani, S. Menezo, and L. C. Andreani, "Broad parameter optimization of polarization-diversity 2d grating couplers for silicon photonics," *Optics Express*, vol. 21, no. 18, pp. 21556–21568, 2013.

[199] W. S. Zaoui, M. F. Rosa, W. Vogel, M. Berroth, J. Butschke, and F. Letzkus, "Cost-effective cmos-compatible grating couplers with backside metal mirror and 69% coupling efficiency," *Optics Express*, vol. 20, no. 26, pp. B238–B243, 2012.

[200] S. K. Selvaraja, D. Vermeulen, M. Schaekers, E. Sleeckx, W. Bogaerts, G. Roelkens, P. Dumon, D. Van Thourhout, and R. Baets, "Highly efficient grating coupler between optical fiber and silicon photonic circuit," in *Conference on Lasers and Electro-Optics*, p. CTuC6, Optical Society of America, 2009.

[201] M. T. Wade, F. Pavanello, R. Kumar, C. M. Gentry, A. Atabaki, R. Ram, V. Stojanović, and M. A. Popović, "75% efficient wide bandwidth grating couplers in a 45 nm microelectronics cmos process," in *Optical Interconnects Conference (OI), 2015 IEEE*, pp. 46–47, IEEE, 2015.

[202] M. Dai, L. Ma, Y. Xu, M. Lu, X. Liu, and Y. Chen, "Highly efficient and perfectly vertical chip-to-fiber dual-layer grating coupler," *Optics Express*, vol. 23, no. 2, pp. 1691–1698, 2015.

[203] J. Notaros and M. A. Popović, "Finite-difference complex-wavevector band structure solver for analysis and design of periodic radiative microphotonic structures," *Optics Letters*, vol. 40, no. 6, pp. 1053–1056, 2015.

[204] X. Chen, C. Li, C. K. Fung, S. M. Lo, and H. K. Tsang, "Apodized waveguide grating couplers for efficient coupling to optical fibers," *IEEE Photonics Technology Letters*, vol. 22, no. 15, pp. 1156–1158, 2010.

[205] Y. Ding, H. Ou, and C. Peucheret, "Ultrahigh-efficiency apodized grating coupler using fully etched photonic crystals," *Optics Letters*, vol. 38, no. 15, pp. 2732–2734, 2013.

[206] W. S. Zaoui, A. Kunze, W. Vogel, M. Berroth, J. Butschke, F. Letzkus, and J. Burghartz, "Bridging the gap between optical fibers and silicon photonic integrated circuits," *Optics Express*, vol. 22, no. 2, pp. 1277–1286, 2014.

[207] M. Antelius, K. B. Gylfason, and H. Sohlström, "An apodized soi waveguide-to-fiber surface grating coupler for single lithography silicon photonics," *Optics Express*, vol. 19, no. 4, pp. 3592–3598, 2011.

[208] B. Wohlfeil, L. Zimmermann, and K. Petermann, "Optimization of fiber grating couplers on soi using advanced search algorithms," *Optics Letters*, vol. 39, no. 11, pp. 3201–3203, 2014.

[209] Q. Zhong, V. Veerasubramanian, Y. Wang, W. Shi, D. Patel, S. Ghosh, A. Samani, L. Chrostowski, R. Bojko, and D. V. Plant, "Focusing-curved subwavelength grating couplers for ultra-broadband silicon photonics optical interfaces," *Optics Express*, vol. 22, no. 15, pp. 18224–18231, 2014.

[210] Y. Tang, Z. Wang, L. Wosinski, U. Westergren, and S. He, "Highly efficient nonuniform grating coupler for silicon-on-insulator nanophotonic circuits," *Optics Letters*, vol. 35, no. 8, pp. 1290–1292, 2010.

[211] D. Benedikovic, P. Cheben, J. H. Schmid, D.-X. Xu, J. Lapointe, S. Wang, R. Halir, A. Ortega-Moñux, S. Janz, and M. Dado, "High-efficiency single etch step apodized surface grating coupler using sub-

wavelength structure," *Laser & Photonics Reviews*, vol. 8, no. 6, pp. L93–L97, 2014.

[212] D. Benedikovic, P. Cheben, J. H. Schmid, D.-X. Xu, B. Lamontagne, S. Wang, J. Lapointe, R. Halir, A. Ortega-Moñux, S. Janz, *et al.*, "Subwavelength index engineered surface grating coupler with sub-decibel efficiency for 220-nm silicon-on-insulator waveguides," *Optics Express*, vol. 23, no. 17, pp. 22628–22635, 2015.

[213] S. Thibaut, A. Raley, F. Lazarrino, M. Mao, D. De Simone, D. Piumi, K. Barla, A. Ko, A. Metz, K. Kumar, *et al.*, "Euv patterning using car or mox photoresist at low dose exposure for sub 36nm pitch," in *Advanced Etch Technology for Nanopatterning VII*, vol. 10589, p. 105890M, International Society for Optics and Photonics, 2018.

[214] W. D. Sacher, Y. Huang, L. Ding, B. J. Taylor, H. Jayatilleka, G.-Q. Lo, and J. K. Poon, "Wide bandwidth and high coupling efficiency si 3 n 4-on-soi dual-level grating coupler," *Optics Express*, vol. 22, no. 9, pp. 10938–10947, 2014.

[215] C. R. Doerr, L. Chen, Y.-K. Chen, and L. L. Buhl, "Wide bandwidth silicon nitride grating coupler," *IEEE Photonics Technology Letters*, vol. 22, no. 19, pp. 1461–1463, 2010.

[216] X. Chen, K. Xu, Z. Cheng, C. K. Fung, and H. K. Tsang, "Wideband subwavelength gratings for coupling between silicon-on-insulator waveguides and optical fibers," *Optics Letters*, vol. 37, no. 17, pp. 3483–3485, 2012.

[217] J. Notaros, F. Pavanello, M. T. Wade, C. M. Gentry, A. Atabaki, L. Alloatti, R. J. Ram, and M. A. Popović, "Ultra-efficient cmos fiber-to-chip grating couplers," in *Optical Fiber Communications Conference and Exhibition (OFC), 2016*, pp. 1–3, IEEE, 2016.

[218] R. Eberhart and J. Kennedy, "A new optimizer using particle swarm theory," in *Micro Machine and Human Science, 1995. MHS'95., Proceedings of the Sixth International Symposium on*, pp. 39–43, IEEE, 1995.

[219] M. Passoni, D. Gerace, L. Carroll, and L. Andreani, "Grating couplers in silicon-on-insulator: The role of photonic guided resonances on lineshape and bandwidth," *Applied Physics Letters*, vol. 110, no. 4, p. 041107, 2017.

[220] Y. Zhang, D. Kwong, X. Xu, A. Hosseini, S. Y. Yang, J. A. Rogers, and R. T. Chen, "On-chip intra-and inter-layer grating couplers for three-dimensional integration of silicon photonics," *Applied Physics Letters*, vol. 102, no. 21, p. 211109, 2013.

[221] C. Wan, T. K. Gaylord, and M. S. Bakir, "Grating design for interlayer optical interconnection of in-plane waveguides," *Applied Optics*, vol. 55, no. 10, pp. 2601–2610, 2016.

[222] M. Cabezón, I. Garcés, A. Villafranca, J. Pozo, P. Kumar, and A. Kaźmierczak, "Silicon-on-insulator chip-to-chip coupling via out-of-plane or vertical grating couplers," *Applied Optics*, vol. 51, no. 34, pp. 8090–8094, 2012.

[223] S. Bernabé, C. Kopp, M. Volpert, J. Harduin, J.-M. Fédéli, and H. Ribot, "Chip-to-chip optical interconnections between stacked self-aligned soi photonic chips," *Optics Express*, vol. 20, no. 7, pp. 7886–7894, 2012.

[224] Y. Kuno, J. Kang, Y. Hayashi, J. Suzuki, T. Amemiya, N. Nishiyama, and S. Arai, "Design of apodized hydrogenated amorphous silicon grating couplers with metal mirrors for inter-layer signal coupling: Toward three-dimensional optical interconnection," *Japanese Journal of Applied Physics*, vol. 54, no. 4S, p. 04DG04, 2015.

[225] M. Sodagar, R. Pourabolghasem, A. A. Eftekhar, and A. Adibi, "High-efficiency and wideband interlayer grating couplers in multilayer si/sio 2/sin platform for 3d integration of optical functionalities," *Optics Express*, vol. 22, no. 14, pp. 16767–16777, 2014.

[226] Y. D. Zonou, S. Bernabe, D. Fowler, M. Francou, O. Castany, and P. Arguel, "Self-alignment with copper pillars micro-bumps for positioning optical devices at submicronic accuracy," in *Electronic Components and Technology Conference (ECTC), 2017 IEEE 67th*, pp. 557–562, IEEE, 2017.

[227] H. H. I. Fraunhofer, "Foundry services on our photonic inp integr ation platform," 2016.

[228] M. Smit, X. Leijtens, H. Ambrosius, E. Bente, J. Van der Tol, B. Smalbrugge, T. De Vries, E.-J. Geluk, J. Bolk, R. Van Veldhoven, *et al.*, "An introduction to inp-based generic integration technology," *Semiconductor Science and Technology*, vol. 29, no. 8, p. 083001, 2014.

[229] A. Turukhin, V. Sudarshanam, M. Shahriar, J. Musser, B. Ham, and P. Hemmer, "Observation of ultraslow and stored light pulses in a solid," *Physical Review Letters*, vol. 88, no. 2, p. 023602, 2001.

[230] M. S. Bigelow, N. N. Lepeshkin, and R. W. Boyd, "Superluminal and slow light propagation in a room-temperature solid," *Science*, vol. 301, no. 5630, pp. 200–202, 2003.

[231] L. V. Hau, S. E. Harris, Z. Dutton, and C. H. Behroozi, "Light speed reduction to 17 metres per second in an ultracold atomic gas," *Nature*, vol. 397, no. 6720, p. 594, 1999.

[232] T. F. Krauss, "Slow light in photonic crystal waveguides," *Journal of Physics D: Applied Physics*, vol. 40, no. 9, p. 2666, 2007.

[233] T. F. Krauss, "Why do we need slow light?," *Nature Photonics*, vol. 2, no. 8, p. 448, 2008.

[234] M. Soljačić, S. G. Johnson, S. Fan, M. Ibanescu, E. Ippen, and J. Joannopoulos, "Photonic-crystal slow-light enhancement of nonlinear phase sensitivity," *Journal of the Optical Society of America B*, vol. 19, no. 9, pp. 2052–2059, 2002.

[235] D. A. Braje, V. Balić, G. Yin, and S. Harris, "Low-light-level nonlinear optics with slow light," *Physical Review A*, vol. 68, no. 4, p. 041801, 2003.

[236] Z. Shi, R. W. Boyd, D. J. Gauthier, and C. Dudley, "Enhancing the spectral sensitivity of interferometers using slow-light media," *Optics Letters*, vol. 32, no. 8, pp. 915–917, 2007.

[237] K. Qin, S. Hu, S. T. Retterer, I. I. Kravchenko, and S. M. Weiss, "Slow light mach–zehnder interferometer as label-free biosensor with scalable sensitivity," *Optics Letters*, vol. 41, no. 4, pp. 753–756, 2016.

[238] H. C. Nguyen, S. Hashimoto, M. Shinkawa, and T. Baba, "Compact and fast photonic crystal silicon optical modulators," *Optics Express*, vol. 20, no. 20, pp. 22465–22474, 2012.

[239] R. S. Tucker, P.-C. Ku, and C. J. Chang-Hasnain, "Slow-light optical buffers: capabilities and fundamental limitations," *Journal of Lightwave Technology*, vol. 23, no. 12, pp. 4046–4066, 2005.

[240] M. Scalora, R. Flynn, S. Reinhardt, R. Fork, M. Bloemer, M. Tocci, C. Bowden, H. Ledbetter, J. Bendickson, J. Dowling, *et al.*, "Ultrashort pulse propagation at the photonic band edge: Large tunable group delay with minimal distortion and loss," *Physical Review E*, vol. 54, no. 2, p. R1078, 1996.

[241] M. Povinelli, S. G. Johnson, and J. Joannopoulos, "Slow-light, band-edge waveguides for tunable time delays," *Optics Express*, vol. 13, no. 18, pp. 7145–7159, 2005.

[242] C. Sciancalepore, K. Hassan, T. Ferrotti, J. Harduin, H. Duprez, S. Menezo, and B. B. Bakir, "Low-loss adiabatically-tapered high-contrast gratings for slow-wave modulators on soi," in *High Contrast Metastructures IV*, vol. 9372, p. 93720G, International Society for Optics and Photonics, 2015.

[243] C. Bao, J. Hou, H. Wu, E. Cassan, L. Chen, D. Gao, and X. Zhang, "Flat band slow light with high coupling efficiency in one-dimensional grating waveguides," *IEEE Photonics Technology Letters*, vol. 24, no. 1, pp. 7–9, 2012.

[244] D. Gao, J. Hou, R. Hao, H. Wu, J. Guo, E. Cassan, and X. Zhang, "Wideband slow light in one-dimensional chirped holey grating waveguide," *IEEE Photonics Technology Letters*, vol. 22, no. 15, pp. 1135–1137, 2010.

[245] C. Bao, J. Hou, H. Wu, X. Zhou, E. Cassan, D. Gao, and X. Zhang, "Low dispersion slow light in slot waveguide grating," *IEEE Photonics Technology Letters*, vol. 23, no. 22, pp. 1700–1702, 2011.

[246] L. H. Frandsen, A. V. Lavrinenko, J. Fage-Pedersen, and P. I. Borel, "Photonic crystal waveguides with semi-slow light and tailored dispersion properties," *Optics Express*, vol. 14, no. 20, pp. 9444–9450, 2006.

[247] R. Hao, E. Cassan, H. Kurt, X. Le Roux, D. Marris-Morini, L. Vivien, H. Wu, Z. Zhou, and X. Zhang, "Novel slow light waveguide with controllable delay-bandwidth product and utra-low dispersion," *Optics Express*, vol. 18, no. 6, pp. 5942–5950, 2010.

[248] Y. Xu, L. Xiang, E. Cassan, D. Gao, and X. Zhang, "Slow light in an alternative row of ellipse-hole photonic crystal waveguide," *Applied Optics*, vol. 52, no. 6, pp. 1155–1160, 2013.

[249] A. Yariv, Y. Xu, R. K. Lee, and A. Scherer, "Coupled-resonator optical waveguide: a proposal and analysis," *Optics Letters*, vol. 24, no. 11, pp. 711–713, 1999.

[250] A. Canciamilla, M. Torregiani, C. Ferrari, F. Morichetti, R. De La Rue, A. Samarelli, M. Sorel, and A. Melloni, "Silicon coupled-ring resonator structures for slow light applications: potential, impairments and ultimate limits," *Journal of Optics*, vol. 12, no. 10, p. 104008, 2010.

[251] J. E. Heebner, R. W. Boyd, and Q.-H. Park, "Slow light, induced dispersion, enhanced nonlinearity, and optical solitons in a resonator-array waveguide," *Physical Review E*, vol. 65, no. 3, p. 036619, 2002.

[252] S. Nishikawa, S. Lan, N. Ikeda, Y. Sugimoto, H. Ishikawa, and K. Asakawa, "Optical characterization of photonic crystal delay lines based on one-dimensional coupled defects," *Optics Letters*, vol. 27, no. 23, pp. 2079–2081, 2002.

[253] T. Baba, "Slow light in photonic crystals," *Nature Photonics*, vol. 2, no. 8, p. 465, 2008.

[254] S. Mookherjea and A. Yariv, "Coupled resonator optical waveguides," *IEEE Journal of Selected Topics in Quantum Electronics*, vol. 8, no. 3, pp. 448–456, 2002.

[255] H. Altug and J. Vučković, "Experimental demonstration of the slow group velocity of light in two-dimensional coupled photonic crystal microcavity arrays," *Applied Physics Letters*, vol. 86, no. 11, p. 111102, 2005.

[256] M. Minkov and V. Savona, "Wide-band slow light in compact photonic crystal coupled-cavity waveguides," *Optica*, vol. 2, no. 7, pp. 631–634, 2015.

[257] Y. Lai, M. S. Mohamed, B. Gao, M. Minkov, R. W. Boyd, V. Savona, R. Houdre, and A. Badolato, "Ultra-wide-band slow light in photonic crystal coupled-cavity waveguides," *arXiv preprint arXiv:1706.09625*, 2017.

[258] K. Üstün and H. Kurt, "Ultra slow light achievement in photonic crystals by merging coupled cavities with waveguides," *Optics Express*, vol. 18, no. 20, pp. 21155–21161, 2010.

[259] M. F. Yanik, W. Suh, Z. Wang, and S. Fan, "Stopping light in a waveguide with an all-optical analog of electromagnetically induced transparency," *Physical Review Letters*, vol. 93, no. 23, p. 233903, 2004.

[260] F. Boeuf, S. Crémer, N. Vulliet, T. Pinguet, A. Mekis, G. Masini, L. Verslegers, P. Sun, A. Ayazi, N.-K. Hon, *et al.*, "A multi-wavelength 3d-compatible silicon photonics platform on 300mm soi wafers for 25gb/s applications," in *2013 IEEE International Electron Devices Meeting*, pp. 13–3, IEEE, 2013.

[261] E. Temporiti, G. Minoia, M. Repossi, D. Baldi, A. Ghilioni, and F. Svelto, "23.4 a 56gb/s 300mw silicon-photonics transmitter in 3d-integrated pic25g and 55nm bicmos technologies," in *Solid-State Circuits Conference (ISSCC), 2016 IEEE International*, pp. 404–405, IEEE, 2016.

[262] L. Li, "Formulation and comparison of two recursive matrix algorithms for modeling layered diffraction gratings," *Journal of the Optical Seciety of America A*, vol. 13, no. 5, pp. 1024–1035, 1996.

[263] N. W. Ashcroft and N. D. Mermin, "Solid state physics (holt, rinehart and winston, new york, 1976)," *Google Scholar*, vol. 403, 2005.

[264] M. Passoni, D. Gerace, L. O'Faolain, and L. C. Andreani, "Optimizing band-edge slow light in silicon-on-insulator waveguide gratings," *Optics Express*, vol. 26, no. 7, pp. 8470–8478, 2018.

[265] A. Oskooi, A. Mutapcic, S. Noda, J. Joannopoulos, S. P. Boyd, and S. G. Johnson, "Robust optimization of adiabatic tapers for coupling to slow-light photonic-crystal waveguides," *Optics Express*, vol. 20, no. 19, pp. 21558–21575, 2012.

[266] X. Zhao, H. Dalir, X. Xu, and R. T. Chen, "Efficient coupling into slow-light one-dimensional fishbone waveguide by mode converter method," *Applied Physics Express*, vol. 10, no. 7, p. 072502, 2017.

[267] S. G. Johnson, P. Bienstman, M. Skorobogatiy, M. Ibanescu, E. Lidorikis, and J. Joannopoulos, "Adiabatic theorem and continuous coupled-mode theory for efficient taper transitions in photonic crystals," *Physical Review E*, vol. 66, no. 6, p. 066608, 2002.

[268] L. Li, "Use of fourier series in the analysis of discontinuous periodic structures," *Journal of the Optical Seciety of America A*, vol. 13, no. 9, pp. 1870–1876, 1996.

[269] J. P. Hugonin and P. Lalanne, "Perfectly matched layers as nonlinear coordinate transforms: a generalized formalization," *Journal of the Optical Seciety of America A*, vol. 22, no. 9, pp. 1844–1849, 2005.

[270] S. H. Zanakis and J. R. Evans, "Heuristic "optimization": Why, when, and how to use it," *Interfaces*, vol. 11, no. 5, pp. 84–91, 1981.

[271] R. L. Rardin and R. Uzsoy, "Experimental evaluation of heuristic optimization algorithms: A tutorial," *Journal of Heuristics*, vol. 7, no. 3, pp. 261–304, 2001.

[272] D. Whitley, "A genetic algorithm tutorial," *Statistics and Computing*, vol. 4, no. 2, pp. 65–85, 1994.

[273] F. Glover and M. Laguna, "Tabu search," in *Handbook of combinatorial optimization*, pp. 2093–2229, Springer, 1998.

[274] S. Kirkpatrick, C. D. Gelatt, and M. P. Vecchi, "Optimization by simulated annealing," *Science*, vol. 220, no. 4598, pp. 671–680, 1983.

[275] M. Dorigo and M. Birattari, "Ant colony optimization," in *Encyclopedia of machine learning*, pp. 36–39, Springer, 2011.

[276] J. Robinson and Y. Rahmat-Samii, "Particle swarm optimization in electromagnetics," *IEEE Transactions on Antennas and Propagation*, vol. 52, no. 2, pp. 397–407, 2004.

[277] N. Jin and Y. Rahmat-Samii, "Advances in particle swarm optimization for antenna designs: real-number, binary, single-objective and multiobjective implementations," *IEEE Transactions on Antennas and Propagation*, vol. 55, no. 3, pp. 556–567, 2007.

[278] S. Cui and D. S. Weile, "Application of a parallel particle swarm optimization scheme to the design of electromagnetic absorbers," *IEEE Transactions on Antennas and Propagation*, vol. 53, no. 11, pp. 3616–3624, 2005.

[279] J. Kennedy and R. C. Eberhart, "A discrete binary version of the particle swarm algorithm," in *Systems, Man, and Cybernetics, 1997. Computational Cybernetics and Simulation., 1997 IEEE International Conference on*, vol. 5, pp. 4104–4108, IEEE, 1997.

[280] M. A. Khanesar, M. Teshnehlab, and M. A. Shoorehdeli, "A novel binary particle swarm optimization," in *Control & Automation, 2007. MED'07. Mediterranean Conference on*, pp. 1–6, IEEE, 2007.

[281] P. K. Tripathi, S. Bandyopadhyay, and S. K. Pal, "Multi-objective particle swarm optimization with time variant inertia and acceleration coefficients," *Information Sciences*, vol. 177, no. 22, pp. 5033–5049, 2007.

[282] S. Mostaghim and J. Teich, "Strategies for finding good local guides in multi-objective particle swarm optimization (mopso)," in *Swarm Intelligence Symposium, 2003. SIS'03. Proceedings of the 2003 IEEE*, pp. 26–33, IEEE, 2003.

[283] M. R. Rapaić and Ž. Kanović, "Time-varying pso–convergence analysis, convergence-related parameterization and new parameter adjustment schemes," *Information Processing Letters*, vol. 109, no. 11, pp. 548–552, 2009.

List of Publications

Journal Papers

- Passoni M., Gerace D., Carroll L., Andreani L.C.
  "Grating couplers in silicon-on-insulator: The role of photonic guided resonances on lineshape and bandwidth"
  Applied Physics Letters. 2017 Jan 23; 110(**4**):041107.
  DOI:10.1063/1.4974992

- Passoni M., Gerace D., O'Faolain L., Andreani L.C.
  "Optimizing band-edge slow light in silicon-on-insulator waveguide gratings"
  Optics Express. 2018 Apr 2; 26(**7**):8470-8.
  DOI:10.1364/OE.26.008470

- Passoni M., Floris F., Hwang H.Y.,Zagaglia L., Carroll L., Andreani LC., O'Brien P.
  "Co-optimizing grating couplers for hybrid integration of InP and SOI photonic platforms "
  AIP Advances. 2018 Sep 14; 8:095109.
  DOI:10.1063/1.5046164

- Fieramosca A., De Marco L., Passoni M, Polimeno L., Rizzo A., Rosa B., Cruciani G., Dominici L., De Giorgi M., Gigli G., Andreani L.C., Gerace D., Ballarini D., Sanvitto D.
  "Tunable out-of-plane excitons in 2D single crystal perovskites"
  ACS Photonics. 2018 Sep 11; 5.10:4179-4185.
  DOI:10.1021/acsphotonics.8b00984

Conference Papers

- Andreani L.C., Gerace D., Passoni M., Bozzola A., Carroll L.
  "Optimizing grating couplers for silicon photonics"
  2016 18th International Conference on Transparent Optical Networks (ICTON). IEEE, 2016.
  DOI:10.1109/ICTON.2016.7550565

- Passoni M., Andreani L.C., Gerace D., O'Faolain L., Andreani L.C.
  "Slow Light in Waveguide Gratings on Silicon-on-Insulator Platform"
  2018 20th International Conference on Transparent Optical Networks (ICTON). IEEE, 2018.
  DOI:10.1109/ICTON.2018.8473888

Acknowledgements

First of all, I would like to acknowledge my supervisors, Prof. Lucio Claudio Andreani and Prof. Dario Gerace, for all the support and the precious teaching they offered me in this years.

Afterward, I would like to thanks Dr. Lee Carroll, for giving me the opportunity to spend three month as an intern at Tyndall National Institute in Cork. In addition, my gratitude goes to Dr. Francesco Floris and Luca Zagaglia, for their presence and support during such forming experience.

Heartfelt thanks to Prof. Pavel Cheben and Prof. Eric Cassan for having referred my thesis, providing constructive criticisms and useful advices.

Special thanks to my family, which has always been there for me, even in the most difficult moments.

Moreover, I would like to acknowledge Dr. Angelo Bozzola for teaching me the basis of Lumerical FDTD solutions, Prof. Marco Liscidini, for providing me with his FORTRAN implementation of the RCWA method, and Dr. Francisco Soares, at Faunhofer Heinrich Hertz Institute, for details on the available InP platform.

Furthermore, heartfelt thanks go to Antonio Fincato, at STMicroelectronics, and Dr. William Whelan-Curtin, at Cork Institute of Technology, for the many useful discussions ad suggestions.

In addition, CINECA is gladly acknowledge for the granting of High Performance Computing resources under the ISCRA initiative.

In the end, I would like to thanks all my friends and colleagues, who helped me in this experience.